The Optimal Design of a Concentric Coil, Radial Magnet Moving Magnet Actuator

by

Adrian A. Adames

A thesis submitted in partial fulfillment
of the requirements for the degree of
Master of Science in Engineering
(Department of Mechanical Engineering)
in The University of Michigan
2015

Advisor:
Professor Shorya Awtar

ACKNOWLEDGEMENTS

I would like to thank my advisor, Professor Shorya Awtar, for his guidance and mentorship throughout my graduate studies. I would like to thank David Hiemstra whose work on moving magnet actuators laid the foundation for the work presented in this thesis. I would like to thank Daniel Grohnke, who, as an undergraduate, was able to handle everything we threw at him. David and Daniel deserve most of the credit for the detailed hardware design of the MMA design presented in this thesis, and for that, I thank you both. Finally, I would like to thank my colleagues at the Precision Systems Design Laboratory for all the help and support they have provided me over the years.

TABLE OF CONTENTS

LIST OF FIGURES

LIST OF TABLES

ABSTRACT

A moving magnet actuator (MMA) is a direct-drive, single-phase, linear electromagnetic actuator that operates via the Lorentz force phenomenon, utilizing the interaction between a current-carrying stator coil and a permanent magnet mover assembly to generate force and subsequent displacement. MMAs come in a variety of different architectures, different topological arrangements between the current-carrying coil, the permanent magnet mover assembly, and a low reluctance housing structure (e.g. a soft iron housing structure) which serves to facilitate a desired magnetic flux flow profile throughout the architecture. MMAs have been identified in prior work as one of the few types of actuators that are capable of satisfying the stringent actuator level design specifications required of actuators used in high performance motion systems which are defined in this thesis as motion systems capable of simultaneously achieving large range (~10mm), high speed (>1m/s), and high (<10nm) motion quality (accuracy, precision, resolution) in a desktop-size form factor. The research presented in this thesis was motivated by the desire to overcome the performance limitations of commercially available MMAs that in turn limit the maximum achievable performance of single-axis, MMA-driven, flexure-based motion systems. This goal was realized via the detailed evaluation, optimization, design, development and construction of a recently proposed concentric coil, radial magnet MMA[*†]. This prior work highlighted the potential of this design but did not present formal analysis and/or optimization to demonstrate this potential via simulation or experiments.

This research introduces an actuator level figure of merit, referred to as the *performance metric* throughout this thesis, that quantifies the degree to which an MMA enables the simultaneous achievement of large range, high speed, and high motion quality in single-axis, MMA-driven, flexure-based motion system. Comprising the product of the previously reported actuator level figure of merit known as the dynamic actuator constant and a newly introduced quantity referred to as the dynamic mass quantity, the performance metric builds on prior work that claimed that an MMA's dynamic actuator constant should be maximized in order to maximize the performance of the motion system. This thesis shows, via analysis of the dynamics of a general single-axis, MMA-driven, flexure-based motion system in the context of control system design for high performance motion systems, that solely maximizing an actuator's dynamic actuator constant is not the best strategy for maximizing overall motion system performance. Instead, the analysis shows that, while the dynamic actuator constant is still a valuable figure of merit with which to compare the relative performance merit of different MMA designs, the appropriate strategy for maximizing overall motion system performance is to maximize the product of an MMA's dynamic actuator constant and dynamic mass quantity, i.e., the performance metric. Overall, the analysis of the dynamics and control of a general single-axis, MMA-driven, flexure-based motion system indicated that that there are four critical actuator level design specifications that an MMA must satisfy to maximize the performance of the motion system: one, a large motion range; two, a highly uniform force-stroke profile; three, reasonably small off-axis attraction forces between the MMA's permanent magnet and back iron; and four, a large magnitude of the product of the actuator's dynamic actuator constant and dynamic mass quantity.

Throughout this thesis, the dynamic actuator constant is utilized as a figure of merit with which to compare the relative performance merit of different MMA designs. In prior work it was suggested that the dynamic actuator constant of the traditional, commercially-available MMA with a motion range of around 10 [mm] was limited to a maximum of ≈20 [$\sqrt{Hz}$]; a maximum which could not be readily overcome by changing the values or relative proportions of the different geometric parameters that define the design of the traditional MMA. The potential performance of the concentric coil, radial magnet MMA architecture was bolstered by analysis of an idealized model representative of the force producing physics of an MMA; analysis that revealed the existence of a fundamental upper limit to the maximum achievable dynamic actuator constant of a Lorentz force actuator. Assuming the use of the best available permanent magnet (N52-grade neodymium) and coil winding (copper) material, the upper limit to the dynamic actuator constant was calculated to be 62.8 [$\sqrt{Hz}$]. Certain similarities between the topologies of the concentric coil, radial magnet MMA architecture and the ideal MMA model give the concentric coil, radial magnet MMA architecture distinct performance advantages over the commercially available traditional MMA architecture.

With the above-mentioned actuator level design specifications kept in mind, a systematic process was carried out to evaluate the potential performance of several variations of the concentric coil, radial magnet MMA. After selecting the particular variation of the concentric coil, radial magnet MMA architecture with the highest

[*] D. B. Hiemstra, "The design of moving magnet actuators for large-range flexure-based nanopositioning," M. S. thesis, Dept. of Mech. Eng., Univ. of Michigan, Ann Arbor, MI, 2014.

[†] D. Hiemstra, G. Parmar, C. Welch, and S. Awtar, "Electromagnetic actuators and component designs thereof," *US Pat. Application* USA 2014/0235644.

potential performance, a brute-force search optimization process was carried out to optimize the design of the concentric coil, radial magnet MMA. The brute-force search optimization process utilizes a closed form approximation of the concentric coil, radial magnet MMA's performance metric to identify an approximate optimal actuator design, followed by FEA simulations to hone in on the optimal actuator design. According to the FEA simulations, the dynamic actuator constant and performance metric values of the optimal concentric coil, radial magnet MMA design were predicted to be 36.8 [$\sqrt{Hz}$] and 22.2 [$\sqrt{Hz} \cdot \frac{1}{\sqrt{kg}}$], respectively. An MMA with optimized dimensions corresponding to these performance values was constructed and tested. Experimental characterization of this constructed MMA, however, yielded an MMA with dynamic actuator constant and performance metric values of 25.5 [$\sqrt{Hz}$] and 15.4 [$\sqrt{Hz} \cdot \frac{1}{\sqrt{kg}}$], respectively. Nevertheless, the measured dynamic actuator constant of 25.5 [$\sqrt{Hz}$] is 27.5% larger than the largest dynamic actuator constant value of ≈20 [$\sqrt{Hz}$] that was reported in the survey of traditional MMA architectures conducted in prior work[*‡] and 82.1% larger than the dynamic actuator constant value of 14 [$\sqrt{Hz}$] that was reported for the traditional MMA that was designed and constructed in the prior work[‡].

[‡] D. B. Hiemstra, G. Parmar, and S. Awtar, "Performance tradeoffs posed by moving magnet actuators in flexure-based nanopositioning," *IEEE/ASME Transactions on Mechatronics*, vol. 19, no. 1, pp. 201-212, Feb. 2014

CHAPTER 1

1 Introduction and Motivation

A moving magnet actuator (MMA) is a direct-drive, single-phase, linear electromagnetic actuator [1]. MMAs operate via the Lorentz force phenomenon, utilizing the interaction between a current-carrying coil – the stator – and a permanent magnet mover to generate force and subsequent displacement. Their unique physical construction enables non-contact, frictionless, and cog-free actuation over several millimeters range of motion, making them useful in applications such as precision motion systems [2], disk drives [3], and automotive valves [4].

MMAs come in a variety of different architectures or topological arrangements. Key components common to most MMAs include a static current-carrying coil, a permanent magnet mover, and a low reluctance material that facilitates a desired magnetic flux flow profile throughout the architecture. The traditional MMA architecture, shown in Figure 1, is the one of the most commonly used MMA architectures [5]. It employs an axially magnetized (i.e. magnetized in the direction of the motion axis) permanent magnet cylinder sandwiched between two pole pieces as the mover. The mover travels between two sets of oppositely wound coil windings fixed to a steel housing, which acts as the stator. The two windings are fixed at two different axial locations on the steel housing. The pole pieces of the mover and the steel housing of the stator guide the magnetic flux from the permanent magnet through the coil windings, producing a Lorentz force linearly proportional to the current through the windings. Not shown in the figure are the bearings that support actuator motion. The type of bearing used to guide mover motion is application-specific.

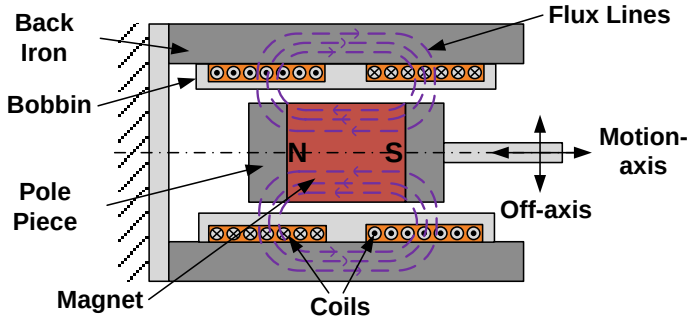

Figure 1: A cross section of the traditional MMA architecture taken along the motion axis of the MMA.

The relatively uncommon concentric coil radial magnet MMA architecture, shown in Figure 2, is the focus of this thesis. It employs as the mover two ring-shaped, radially magnetized permanent magnets of opposite polarity. The mover travels between two oppositely wound sets of concentric coil windings fixed to a steel housing. A three dimensional solid model of the concentric coil radial magnet MMA can be seen in Figure 3.

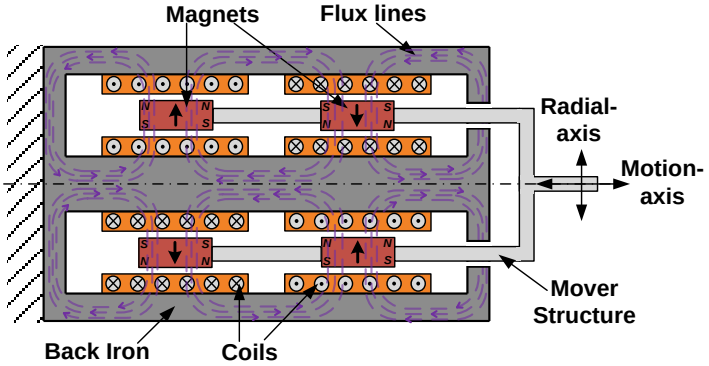

Figure 2: A cross section of the concentric coil, radial magnet MMA architecture taken along the motion axis of the MMA.

MMAs are commonly used in mechatronic motion systems; systems which, in general, comprise an actuator and bearing along with a sensor, driver, and control logic and hardware to produce controlled motion. The specific kind of MMA-driven motion system discussed in this thesis comprises a concentric coil, radial magnet MMA, a diaphragm flexure bearing, a current driver, an optical encoder, and a feedback control system. Figure 3 shows how the various components work together to make up a motion system, highlighting the interdependent nature of the system via a flow diagram.

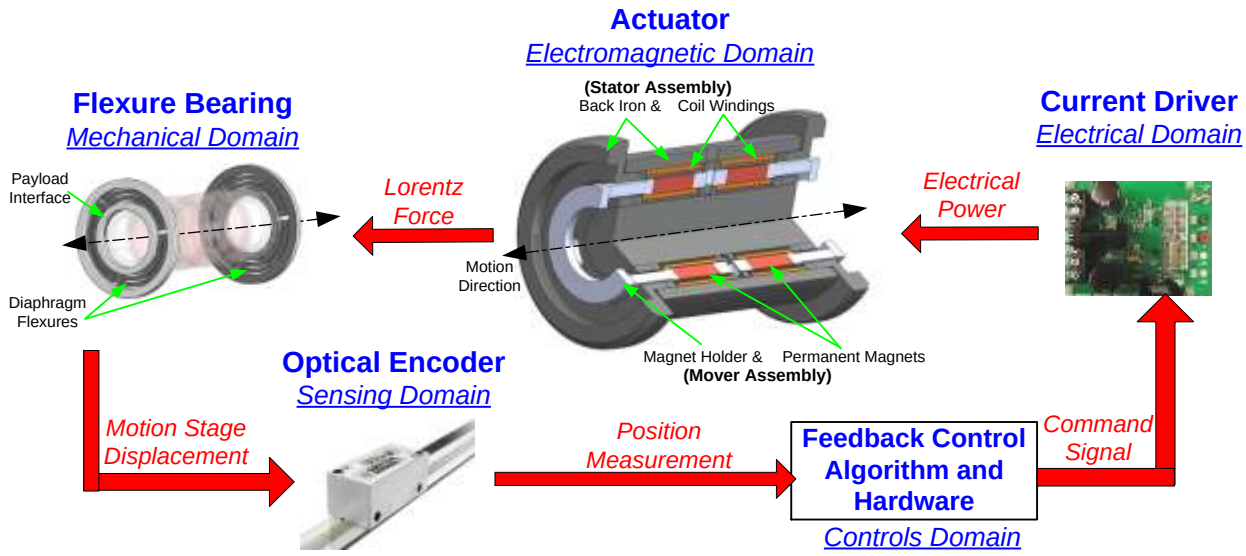

Figure 3: The basic components of a mechatronic motion system.

In general, MMAs can have multiple phases for the windings; the focus of this thesis, however, is on MMAs with a single-phase winding. The unique physical construction of MMAs with a single-phase winding enables them to provide non-contact, frictionless, and ripple-free actuation over several millimeters range of motion, making them useful in applications such as precision motion systems [2], disk drives [3], automotive valves [4], compressors and fuel pumps [3][4][6][7], and vibration isolators [3][4][6][7][8]. Here we would like to distinguish between the terms "ripple-free" and "cog-free". A ripple refers to a periodic variation in the actuator's force output over its stroke as the current is kept constant. In an MMA, the permanent magnet experiences a reluctance force, the magnitude of which depends on the construction of the MMA. This results in a variation in the actuator's output force over its stroke for a constant current; however, this variation is not periodic and therefore not a ripple. Instead, this force variation may be referred to as "cogging", and in that sense, MMAs are not cog-free actuators.

MMAs are one of the few classes of actuators capable of satisfying the stringent requirements required of actuators used in nanopositioning systems, mechatronic motion systems capable of producing motion with nanometric (<10nm) *motion quality* (accuracy, precision, resolution) [9]. Because of this high motion quality, nanopositioning systems are employed in various sensitive applications to provide relative scanning as well as point-to-point motion. These applications include scanning probe microscopy [10][11], scanning probe lithography [12], nanometrology [12], and hard-drive and semiconductor inspection [13]. Nanopositioning systems are one of the primary motivations for this thesis. The concentric coil, radial magnet MMA design discussed in this thesis shows promise for overcoming the actuation technology limitations of the state of the art in actuation technology for desktop size, high performance nanopositioning applications.

Due, in large part, to limitations in actuation technology, a long standing challenge in the performance of nanopositioning systems has been the simultaneous achievement of large range (~10mm), high speed (>1m/s), and high motion quality (<10nm) in a nanopositioning system with desktop size form factor [14]. Desktop size nanopositioning systems capable of producing high speed, nanometric quality motion are commercially available and have been reported in the literature, but they are restricted to a relatively small motion range of a few hundred microns per axis [15][16]. Increasing this range to several millimeters will significantly increase the "area-coverage" in scanning nanometrology and direct-write nanomanufacturing, potentially leading to large-scale industrial applications of these techniques.

This thesis aims to methodically assess an MMA's ability to achieve the actuator level performance that can enable motion system performance in terms of simultaneous large range, high speed, high motion quality, and desktop size. Prior work has identified an actuator level figure of merit referred to as β, the dynamic actuator constant, as an important MMA design metric that captures the relationship between the actuator level performance specifications of force output, power consumption, and mover mass and the system level performance specifications of motion range, speed, and motion quality [5]. It has been claimed that the maximum achievable dynamic actuator constant of an MMA places on upper bound on overall system level performance, requiring that the designer of a high performance motion system make tradeoffs between the system level performance specifications of motion range, speed, and motion quality.

The contributions of this thesis are as follows:

1. It is shown that there exists an upper limit to the maximum achievable dynamic actuator constant that is inherent not only to MMAs but to all Lorentz force actuators.

2. It is shown that the dynamic actuator constant is not solely responsible for placing an upper bound on the overall motion system performance; the masses of the actuator and payload also play an important role. This is reflected in a new performance metric that captures an MMA design's suitability as the actuator of a high performance motion system more accurately. Deemed the *performance metric* (*PM)*, it comprises the product of the dynamic actuator constant and a quantity referred to as the dynamic mass quantity (defined in Section 2.2.1).

3. A methodical evaluation process to weigh the strengths and weaknesses of several variations of the concentric coil, radial magnet MMA architecture arrangement is presented.

4. A systematic optimization design process for designing a concentric coil, radial magnet MMA architecture that maximizes the performance of the motion system is presented.

Although the MMA presented in this thesis is intended to be integrated in a single-axis, flexure-based motion system, the MMA design insights generated in this research are applicable to any motion system application that simultaneously requires high speeds, large range, and high motion quality.

The structure of this thesis is as follows. In Chapter 2, the system level dynamics and control of a general single-axis, MMA-driven, flexure-based motion system are analyzed to derive an analytical expression that quantitatively captures the relationship between actuator level design specifications and the motion system performance specifications of interest. Analysis of this analytical expression sheds light on the actuator level design specifications required to achieve the system level performance requirements of large range, high speed, desktop size nanopositioning systems. In Chapter 3, a review of the current state-of-the-art in MMA technology is presented. Different MMA architectures are evaluated based on their ability to satisfy the actuator level design specifications required for actuators used in high performance motion systems. The limitations of the current state-of-the-art MMAs motivate the design and development of the recently reported concentric coil, radial magnet MMA architecture [5][17]. Chapter 4 begins with the analysis of an ideal model representative of the force-producing physics of an MMA, revealing the existence of a fundamental upper limit to the dynamic actuator constant. This upper limit to the dynamic actuator constant is a useful metric, providing insight on the extent to which practical factors (e.g. flux fringing, magnetic saturation, finite assembly tolerances, material properties, etc.) limit optimal performance. This upper limit also provides insight into the relative performance of two MMA architectures, i.e., the difference between the dynamic actuator constants of 15 [$\sqrt{Hz}$] and 30 [$\sqrt{Hz}$] is more significant if the upper bound to the dynamic actuator constant is 60 [$\sqrt{Hz}$] versus if the upper bound to the dynamic actuator constant is 600 [$\sqrt{Hz}$]. In Chapter 5, many variations of the concentric coil, radial magnet MMA architecture are evaluated for high performance. The variation of the concentric coil, radial magnet MMA architecture that is shown in Figure 2 is methodically selected, using the dynamic actuator constant and other considerations, as having the best performance when compared to other variations of this architecture. Chapter 6 covers the modeling (closed-form as well as finite element analysis) and dimensional optimization of the selected MMA architecture for use in a single-axis, diaphragm flexure-based motion system. Chapter 7 presents the experimental setup used to characterize the fabricated MMA and the associated measurement results. The results will show that the concentric coil, radial magnet MMA architecture does indeed provide a larger dynamic actuator constant than previous designs, clearing the way for improved levels of performance for large range, high speed, high quality motion, desktop size motion systems. Finally, Chapter 8 summarizes the contributions of this thesis, open questions, and future work.

CHAPTER 2

2 Background: Deriving actuator level design specifications from system level performance specifications

Achieving the system level performance specifications of large range, high speed, and high motion quality in an MMA-driven motion system imposes several requirements on the design specifications of the components that make up the motion system. These component level design specifications can be identified by developing a quantitative understanding of the relationship between the set of all the component level design specifications and the set of all the desired system level performance specifications. As discussed in [14], each of the components that make up a motion system has its own set of performance limitations that contribute to limiting the maximum achievable performance of the motion system. The focus of this thesis is on the actuator component. The overarching purpose of this chapter is to derive a quantitative understanding of the relationship between the actuator level design specifications and the system level performance specifications. By establishing this relationship, a set of system level performance specifications can then be used to derive the associated actuator level design specifications required to achieve said system level performance.

Detailed in full below, analysis of the motion system's dynamics in the context of control system design for high performance indicates that there are four critical actuator level design specifications that an actuator must satisfy to maximize the performance of the motion system: one, a large motion range; two, a highly uniform force-stroke profile; three, reasonably small off-axis attraction forces between the permanent magnet and the back iron (explained further in Section 2.2.1); and four, a large magnitude of the product of the actuator's dynamic actuator constant and a quantity referred to as the dynamic mass quantity (defined later in Section 2.2.1).

The following discussion on control system design considerations for high performance motion systems establishes the context under which the dynamics of an MMA-driven motion system is analyzed. It serves as the basis from which the system level performance tradeoffs arising from the dynamics of the motion system and the performance limitations of its components are characterized.

2.1 Control system design considerations

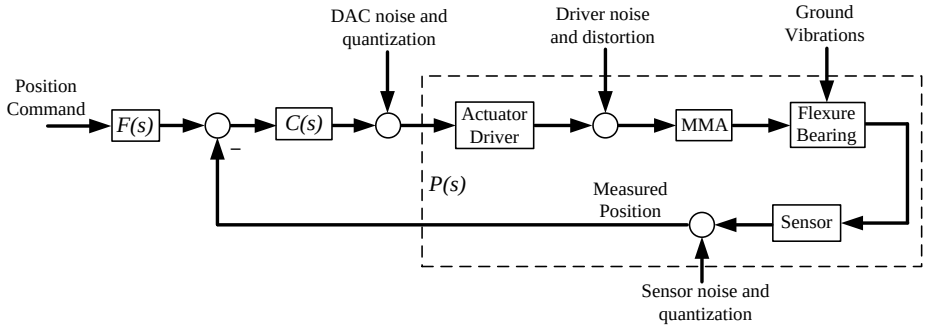

Figure 4: Feedback architecture of a closed-loop, MMA-driven motion system [21].

The dynamic performance of a high performance, closed-loop, MMA-driven motion system (as shown in Figure 4) is described by the five qualities below:

1. *Good tracking performance*. This implies that the tracking error is small, which, in turn, implies that the magnitude of the closed-loop transfer function is close to unity for the motion system's range of operating frequencies.
2. *Good disturbance rejection*. This is important to minimize the motion degrading effects of ground vibrations (output disturbance), driver noise (input disturbance), or any other disturbance from the environment.
3. *Low sensitivity to modeling errors.* This is important to minimize the motion degrading effects of the actuator force-stroke non-uniformity, the nonlinearities of the driver component (signal distortion in the current output of the driver), and the nonlinearities of the real-time control hardware component (e.g. quantization)
4. *Good stability margin.* This is important to ensure stability robustness in the presence of modeling uncertainty and system parameter variation at high frequencies.
5. *Low sensitivity to sensor noise.* This is not as high a priority as the other requirements because of the relatively low noise of the sensor and associated electronics.

The dynamic performance of a linear feedback control-based motion system such as the MMA-driven motion system discussed in this thesis is largely limited by the open-loop bandwidth of the system. When compared to a motion system with a low open-loop bandwidth, a motion system with a high open-loop bandwidth is not only capable of operating at higher speeds, but is also associated with a more favorable tradeoff between low tracking error, low sensitivity to moderate modeling errors, and good disturbance rejection on the one hand and good noise rejection and stability robustness on the other hand [18]. This tradeoff between low tracking error, low sensitivity to moderate modeling errors, and good disturbance rejection on the one hand and good noise rejection and stability robustness against high-frequency uncertainty on the other hand is a direct consequence of the Bode waterbed effect phenomena that follows from Bode's integral theorem [18]. The Bode waterbed effect precludes one from reducing the sensitivity transfer function of a real life physical system over the low frequency range without increasing the sensitivity transfer function over the intermediate frequency range. The same holds true for the complementary sensitivity transfer function. A small sensitivity function is associated with low tracking error, low sensitivity to moderate modeling errors, and good disturbance rejection, while a small complementary sensitivity function is associated with good noise rejection and stability robustness. Furthermore, the inherent structure of the feedback loop precludes one from simultaneously achieving a small sensitivity function gain and a small complementary sensitivity function gain at the same frequency [18].

To improve the tracking performance, disturbance rejection, and sensitivity to moderate modeling errors of a motion system, the gain of the sensitivity function has to be reduced in the low frequency range (motion systems operate in the low frequency range). Decreasing the sensitivity function in the low frequency range, however, requires an increase of the lower bound of the peak of the sensitivity function in the intermediate frequency range, which decreases the stability robustness of the system. Hence, when compared to a motion system with a low open-loop bandwidth, a motion system with a high open-loop bandwidth is capable of achieving a smaller gain of the sensitivity transfer function over the low frequency range with the same level of noise rejection and stability robustness as the motion system with a low open-loop bandwidth.

For a high performance MMA-driven, flexure-based motion system such as the one presented in this thesis, a large open-loop bandwidth is highly desirable to suppress many of the deleterious, motion degrading effects of several of the nonlinearities that exist in the system. The nonlinearities that have the greatest adverse effect on the dynamic performance of the motion system are the nonlinearities associated with the actuator itself and the nonlinearities associated with the actuator driver. Although an MMA-driven, flexure-based motion system is free of friction and backlash, the actuator can have a non-uniform force-stroke profile, i.e., for a fixed current input, the force output of the MMA is not constant along its stroke; it is dependent on the position of the mover [19]. This non-uniformity leads to higher order harmonics in open-loop and closed-loop operation [20][21]. While the motion degrading effect of this nonlinearity can be mitigated by designing the system to have a large open-loop bandwidth and therefore lower sensitivity to moderate modeling errors, the motion degrading effect can be further mitigated by choosing or designing an MMA with a highly uniform force-stroke profile. The actuator level design specification of a highly uniform force-stroke profile is a direct consequence of this.

The nonlinearities associated with the electrical driver are a result of the limitations of the physical components that make up the driver [20]. As shown in Figure 4, these nonlinearities manifest themselves in the loop as harmonic distortion. While the motion degrading effects of these nonlinearities can be mitigated by designing the system to have a large open-loop bandwidth and therefore better closed-loop disturbance rejection, the motion degrading effects can be further mitigated by reducing the power input to the MMA, as the magnitude of the noise and harmonic distortion from the driver tends to increase with power [21].

At this point the rationale behind two of the four critical actuator level design specifications required of high performance MMAs has been presented. The actuator level design specification of a highly uniform force-stroke profile was justified, and the actuator level design specification of a large motion range is self-evident. To deduce the two remaining actuator level design specifications, the dynamics of the motion system is analyzed in the context of the control system design considerations discussed above. From this analysis it will be shown that the product of the actuator level design specifications of the dynamic actuator constant and the dynamic mass quantity place an upper bound on the degree to which the motion system can simultaneously achieve large range, high speed, and high open-loop bandwidth.

2.2 Constraints imposed by Newton's second law

In general, a single-axis, MMA-driven, flexure-based motion system can be modeled as a simple mass-spring system actuated by an MMA as shown in Figure 5, where m_m, the permanent magnet mass, is the mass of the permanent magnet, m_p, the payload mass, is the sum of all the moving masses except for that of the permanent magnet, K_x is the stiffness of the flexure bearing, and x is the position of the motion stage. Applying Newton's second law of motion to the model of the MMA-driven, flexure-based motion system in Figure 5, it is apparent that the equation of motion governing the dynamics of the motion stage is,

$$F_a(t) = \left(m_m + m_p\right)\left(\ddot{x}(t) + \omega_n^{\,2} x(t)\right), \tag{1}$$

where ω_n, the natural frequency of the motion system, is defined as follows,

$$\omega_n^{\,2} \triangleq \frac{K_x}{\left(m_m + m_p\right)}. \tag{2}$$

The open-loop bandwidth of a second-order motion system is approximately equal to its natural frequency [22]. Hence, from here on out, the natural frequency of an MMA-driven, flexure-based motion system is used interchangeably with the open-loop bandwidth of the system. It then follows from section 2.1 that the larger the natural frequency (i.e. open-loop bandwidth) of an MMA-driven motion system, the higher the motion quality of the system.

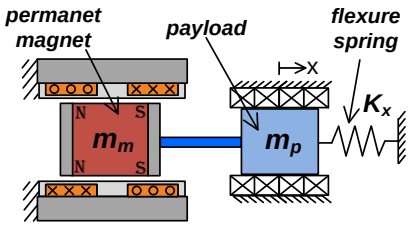

Figure 5: A single-axis, MMA-driven, flexure-based motion system modeled as a simple mass-spring system actuated by an MMA.

As will be shown below, an expression for the maximum actuator force output required for the motion system to sustain a given motion profile command can be derived from Equation (1). This expression for the maximum actuator force output, expressed in terms of the permanent magnet mass, m_m, the payload mass, m_p, the spring constant of the spring, K_x, and the variables that define the motion profile command, corresponds to the point in the motion profile associated with the largest actuator forces.

The nature of the application in which the motion system is employed determines the motion profile command the motion system is expected to carry out. Motion systems are employed to execute a variety of application-specific motion profiles. While large range, high speed, and high motion quality are generally representative of the system level performance specifications required of high performance motion systems, the actual specifications used to quantify range, speed, and motion quality depend on the nature of the application-specific motion profile the motion system is expected to execute. As will be shown below, analysis of Equation (1) in the context of two different application-specific motion profiles will show that, while the different motion profiles can impose different application-specific system level design tradeoffs between range, speed, and motion quality, maximizing the product of the actuator level design specifications of the dynamic actuator constant and the dynamic mass quantity make those tradeoffs more favorable regardless of the motion profile.

In general, motion profiles can be grouped into one of two categories, periodic motion profiles and aperiodic motion profiles. To deduce the two remaining actuator level design specifications required of high performance MMAs, Equation (1) is analyzed in the context of two commonly used motion profiles: a periodic sinusoidal raster scanning motion profile and an aperiodic constant velocity point-to-point positioning motion profile. This analysis is presented below in Sections 2.2.1 and 2.2.2. In each section, an expression for the maximum actuator force output required for the motion system to sustain the motion profile is derived. By incorporating the dynamic actuator constant into these expressions, it will be shown that the magnitude of the product of the dynamic

actuator constant and the dynamic mass quantity places an upper bound on the degree to which the motion system can simultaneously achieve large range, high speed, and high open-loop bandwidth.

2.2.1 Analysis of the motion system's equation of motion for a raster scanning motion profile

Raster scanning motion profiles are typically employed in scanning based imaging applications such as atomic force microscopy, scanning probe microscopy, scanning tunneling microscopy, etc., in which it is desired to measure the variation of a material property across the surface area of a sample. This variation is measured by using a two axis motion system to produce a relative scanning motion between the x-y plane of the sample's surface area and the common z-axis that the sample shares with a probing material property measurement system. As the motion stage provides the relative scanning motion, the material property measurement system probes the sample's surface area, thereby mapping material property measurements taken along the z-axis to different locations across the x-y plane of the sample's surface area. Figure 6 illustrates one example of the x-y motion profile that motion systems are expected to carry out in raster scanning applications. Referred to as the sinusoidal raster scanning motion profile, it is the motion profile of interest in this section of the thesis. Figure 6(a) illustrates the general movement pattern, with the "long motion" of the movement profile carried out along the x-axis and the "small motion" of the movement profile carried out simultaneously along the y-axis. Figure 6(b) and Figure 6(c) illustrate the "long" and "small" motions of the movement profile, respectively, as a function of time. The following analysis of the maximum actuator output force required to sustain this sinusoidal raster scanning motion is based on the "long" sinusoidal motion profile in Figure 6(b).

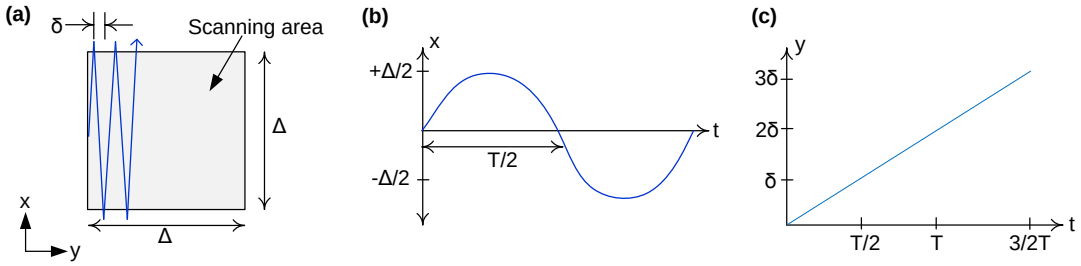

Figure 6: A sinusoidal raster scanning motion profile.

The following sinusoidal expressions in Equation (3) are used as the mathematical representations of the position, velocity, and acceleration motion profiles expected of an MMA-driven motion system performing the raster scanning function,

$$\begin{aligned} x(t) &= \frac{\Delta}{2}\sin(\omega t) \\ \dot{x}(t) &= \frac{\Delta}{2}(\omega)\cos(\omega t) \\ \ddot{x}(t) &= -\frac{\Delta}{2}(\omega)^2\sin(\omega t) \end{aligned} \quad , \tag{3}$$

where $x(t)$ is position, Δ is the peak-to-peak amplitude of the sinusoid, ω is the scanning frequency, t is time, $\dot{x}(t)$ is velocity, and $\ddot{x}(t)$ is acceleration.

It follows from Equation (1) and Equation (3) that the actuator must output the following sinusoidal force waveform to sustain the raster scanning motion profile,

$$F_r(t) = F_{r0}\sin(\omega t)\,, \tag{4}$$

where F_{r0}, the amplitude of the force waveform, is,

$$F_{r0} = \frac{\Delta}{2}\left(m_m + m_p\right)\left(\omega_n{}^2 - \omega^2\right). \tag{5}$$

The magnitude of the amplitude of the force waveform, $|F_{r0}|$, is,

$$\left|F_{r0}\right| = \frac{\Delta}{2}\left(m_m + m_p\right)\left|\omega_n{}^2 - \omega^2\right|, \tag{6}$$

which implies that, for an actuator to sustain the raster scanning motion profile, its maximum force output, $F_{a,max}$, has to be greater than or equal to the magnitude of the amplitude of the force waveform, i.e.,

$$F_{a,\max} \geq \left|F_{r0}\right| = \frac{\Delta}{2}\left(m_m + m_p\right)\left|\omega_n{}^2 - \omega^2\right| \tag{7}$$

.

Dividing both sides of Equation (6) by the amplitude of the position waveform, $\frac{\Delta}{2}$, and the sum of the magnet and payload masses,(m_m+m_p), shows that,

$$\frac{\left|F_{r0}\right|}{\left(m_m + m_p\right)\cdot\frac{\Delta}{2}} = \left|\omega_n{}^2 - \omega^2\right|. \tag{8}$$

The right hand side of Equation (8) is plotted as a function of scanning speed for several values of system natural frequencies in Figure 7. These plots correspond to the necessary combination of payload mass, m_p, motion range, Δ, force waveform amplitude magnitude, $|F_{r0}|$, and permanent magnet mass, m_m, required to operate at scanning speed ω for a motion system that has a natural frequency of ω_n. Given a fixed payload mass, m_{p0}, motion range, Δ_0, and permanent magnet mass, m_{m0}, these plots can be said to be representative of the actuator effort required to operate a motion system with natural frequency ω_n at scanning speed ω.

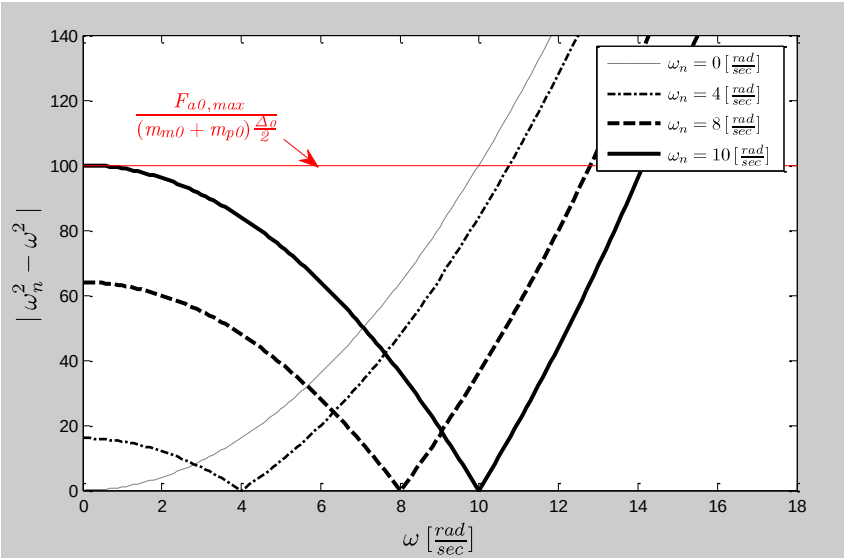

Figure 7: Actuation effort versus scanning speed for motion systems with different natural frequencies.

The plots in Figure 7 show that, given a motion system with natural frequency, $\omega_n > 0$, payload mass, m_{p0}, motion range Δ_0, and permanent magnet mass m_{m0}, operating in the scanning speed range, $0 < \omega < \omega_n$, the greatest actuation forces occur at $\omega = 0+$, the scanning speed just past zero. For the same motion system operating in the scanning speed range, $\omega > \omega_n$, the greatest actuation forces occur at the maximum scanning speed the system is

intended to be operated, ω_{max}. Letting $|F_{r0}|_{max}$ be the magnitude of the maximum actuator force output required to sustain the raster scanning motion profile across each of these two different scanning speed regions,

$$\left|F_{r0}\right|_{\max} = \begin{cases} \dfrac{\Delta_0}{2}\left(m_{m0}+m_{p0}\right)\omega_n^{\,2} & \text{for region } 0<\omega<\omega_n \\ 0 & \text{for region } \omega=\omega_n \\ \dfrac{\Delta_0}{2}\left(m_{m0}+m_{p0}\right)\left(\omega_{\max}^{\,2}-\omega_n^{\,2}\right) & \text{for region } \omega_{\max}>\omega_n . \end{cases} \tag{9}$$

The plot of the horizontal red line in Figure 7 corresponds to the most demanding combination of system natural frequency and scanning speed that the motion system is capable of achieving given an actuator with a maximum force output of $F_{a0,max}$. The intersections between the red and black lines show that, given an actuator with a maximum force output of $F_{a0,max}$, the larger the natural frequency of the system, the larger the maximum achievable scanning speed of the motion system. Hence, to maximize the scanning speed of a single-axis, MMA-driven, flexure-based motion system for a given payload mass, m_{p0}, motion range, Δ_0, and permanent magnet mass, m_{m0}, one should design the motion system to have as large a natural frequency as the actuator and its maximum force output can support. Equation (9) implies that the maximum natural frequency that the actuator can sustain is,

$$\omega_{n,\max} = \sqrt{\frac{F_{a0,\max}}{\left(m_{m0}+m_{p0}\right)\cdot\dfrac{\Delta_0}{2}}}\,, \tag{10}$$

and that the maximum achievable scanning speed of the motion system is,

$$\omega_{\max} = \sqrt{2}\,\omega_{n,\max}\,. \tag{11}$$

Rearranging Equation (10),

$$\frac{F_{a0,\max}}{\left(m_{m0}+m_{p0}\right)} = \frac{\Delta_0}{2}\cdot\omega_{n,\max}^{\,2}\,. \tag{12}$$

Equation (12) shows how the quotient of the maximum force output of the actuator and the sum of the actuator and payload masses places an upper bound on the degree to which the motion system can simultaneously achieve a large motion range (as captured by Δ_0), high speed (shown to be captured by ω_n in Equation (11)), and high open-loop bandwidth (as captured by ω_n). This quotient, however, is lacking when considered as a figure of merit with which to evaluate and design actuators for high performance motion systems [5]. A better figure of merit would solely be a function of actuator properties. It would be representative of the inherent performance of the actuator regardless of payload mass. In addition, the quotient does not offer an obvious way to incorporate any potential power constraints imposed by either the maximum heat removal capability of the motion system's thermal management system, the maximum power input of the driver, or the maximum power input that the driver can deliver without introducing unacceptably high levels of electrical noise and signal distortion. To address these shortcomings, a figure of merit known as the dynamic actuator constant has been introduced in the past [1].

The dynamic actuator constant is defined as follows,

$$\beta = \frac{K_t}{\sqrt{R}\sqrt{m_m}} = \frac{F_a(t)}{\sqrt{P(t)}\sqrt{m_m}}\,, \tag{13}$$

where K_t is the actuator force constant, and R is the coil winding resistance. Although the dynamic actuator constant is an actuator constant in that it is a function of actual physical parameters such as size, construction, materials, and geometry, it can also be stated in terms of the dynamic variables indicated above. As stated in [1], "[The dynamic actuator constant] reveals an inherent trade-off associated with the force, moving mass, and the power consumption

of an MMA, which cannot be overcome by varying the actuator size. It should be noted, however, that β varies somewhat when the relative proportions between the actuator's dimensions are changed." As is shown below, the effect of the dynamic actuator constant on motion system performance is evident when it is incorporated into Equation (12).

The maximum force output of the actuator, $F_{a0,max}$, coincides with the maximum power output of the actuator, $P_{a0,max}$, implying that the dynamic actuator constant for a given actuator can be expressed as follows,

$$\beta_0 = \frac{F_{a0,\max}}{\sqrt{P_{a0,\max}}\sqrt{m_{m0}}}, \tag{14}$$

which, in turn, implies that,

$$F_{a0,\max} = \beta_0 \sqrt{P_{a0,\max}}\sqrt{m_{m0}}. \tag{15}$$

Note here that $F_{a0,max}$ represents the maximum or peak actuator force which is also the amplitude of force and that $P_{a0,max}$ refers to the peak power and not the amplitude of power or average power. The force and power terms in the dynamic actuator constant equation refer to the instantaneous values of the two respective terms. In Appendix A, for both the raster scanning and point-to-point positioning motion profiles analyzed in Sections 2.2.1 and 2.2.2, it is shown that the ratio of the instantaneous actuator force output and the square root of the instantaneous power consumption is a constant. In addition, it is shown that the time at which the motion profiles demand the maximum actuator force output coincides with the time of maximum power consumption, implying that the dynamic actuator constant for a given actuator can be expressed as in Equation (14).

Substituting Equation (15) into Equation (12) shows that,

$$\frac{\beta_0 \sqrt{P_{a0,\max}}\sqrt{m_{m0}}}{\left(m_{m0}+m_{p0}\right)} = \frac{\Delta_0}{2} \cdot \omega_{n,\max}{}^2. \tag{16}$$

Collecting the amplitude of the sinusoidal raster scanning position waveform, the open-loop bandwidth, and the power consumption terms on one side of the equation and the mass terms and dynamic actuator constant term on the other side of the equation shows that,

$$\beta_0 \cdot \frac{\sqrt{m_{m0}}}{\left(m_{m0}+m_{p0}\right)} = \frac{\Delta_0}{2} \cdot \omega_{n,\max}{}^2 \cdot \frac{1}{\sqrt{P_{a0,\max}}}. \tag{17}$$

The quantity that includes the mass terms is deemed as the dynamic mass quantity, $M_{dynamic}$, where,

$$M_{dynamic} \triangleq \frac{\sqrt{m_m}}{m_m + m_p}. \tag{18}$$

Equation (17) can then be expressed as,

$$\beta_0 \cdot M_{dynamic0} = \frac{\Delta_0}{2} \cdot \omega_{n,\max}{}^2 \cdot \frac{1}{\sqrt{P_{a0,\max}}}. \tag{19}$$

Equation (19) quantitatively captures the system level performance limitations associated with the actuator component of the system, showing how the product of the actuator's dynamic actuator constant and dynamic mass quantity places an upper bound on the performance of the system, imposing system level performance tradeoffs between the motion range, open-loop bandwidth and scanning frequency, and power consumption of the system. Analysis of Equation (19) in the context of a power constraint, $P_{a0,max}$, shows that the level to which one can simultaneously achieve large range, high scanning speed, and high open-loop bandwidth is limited by the product of

the actuator's dynamic actuator constant and the dynamic mass quantity. Hence, when designing a high performance MMA, one should aim to maximize the product of its dynamic actuator constant and dynamic mass quantity. One can conduct a similar analysis for a simple mass, no spring, single-axis, MMA-driven motion system and arrive at similar conclusions.

Although the product of the actuator's dynamic actuator constant and the dynamic mass quantity is referred to as an actuator level specification, the dynamic mass quantity is also, in part, a system level specification, as it is a function of the system level specification of the payload mass in addition to being a function of the actuator's permanent magnet mass. The implications of the dynamic mass quantity on system performance and actuator design are presented in Section 2.3. In a theoretical scenario, one would design an MMA architecture by first maximizing its dynamic actuator constant and then scaling its size so that its permanent magnet mass matches the payload mass in the system level specifications, and that would be an optimal solution. This is due to the fact that the dynamic actuator constant has been shown to be independent of geometric scaling and the fact that the maximum of the dynamic mass quantity corresponds to the point when the permanent magnet mass is equal to the payload mass. This is evident when the derivative of the dynamic mass quantity with respect to the magnet mass is set equal to zero,

$$\frac{d}{dm_m} M_{dynamic} = \frac{m_{p0} - m_m}{2\sqrt{m_m}\left(m_m + m_{p0}\right)^2} = 0 \quad , \tag{20}$$

showing that the maximum of the dynamic mass quantity occurs when the magnet mass is equal to the payload mass. Real world considerations introduce many other factors that invalidate this simplistic approach towards optimization, making the optimization of an MMA design a more complicated, multi-iterative procedure, and that is the focus of this thesis.

The last actuator level design specification of reasonably small-off axis attraction forces between the permanent magnet of the MMA's mover assembly and the MMA back iron can be derived from Equation (16). Isolating the square of the maximum naturally frequency of the system on one side of the equation, Equation (16) becomes,

$$\frac{\beta_0 \sqrt{P_{a0,\max}} \sqrt{m_{m0}}}{\left(m_{m0} + m_{p0}\right)} \frac{2}{\Delta_0} = {\omega_{n,\max}}^2 , \tag{21}$$

which can be restated as follows,

$$\beta_0 \cdot M_{dynamic0} \cdot \sqrt{P_{a0,\max}} \cdot \frac{2}{\Delta_0} = \left| \left(\frac{K_x}{\left(m_m + m_p\right)} \right)_{\max} \right| . \tag{22}$$

It is desired to maximize the left hand side of the equation in order to maximize the natural frequency of the system. Recall from section 2.1 that maximizing the natural frequency of the system helps to maximize the motion quality of the system. In addition, recall that, per Equation (11), maximizing the natural frequency of the system maximizes the maximum operating speed of the motion system. It is therefore desired to maximize the left hand side of Equation (22). Assuming that the motion range and maximum power consumption of a motion system has been specified and that the product of the dynamic actuator constant and dynamic mass quantity has been maximized, the next course of action is to get the magnitude of the right hand side of the equation (i.e. the square of the natural frequency of the system) to match the magnitude of the left hand side of the equation. In maximizing the product of the dynamic actuator constant and dynamic mass quantity, the magnet mass and payload mass are specified, leaving those parameters as fixed constraints on the expression on the right hand side of the equation. Therefore, to get the right hand side of the equation to match the maximized left hand of the equation, the motion system's flexure bearing should be designed or selected so that the ratio of the flexure bearing's axial stiffness and the sum of the moving masses equals the left hand side of Equation (22). For the motion system to be realizable, however, the flexure bearing with the desired axial stiffness must have a corresponding off-axis stiffness that is large enough to resist the off-axis attraction forces between the permanent magnets in the mover assembly and the MMA's back iron. Therein lies the actuator level design specification of reasonably small off-axis attraction forces between the permanent

magnet in the MMA mover assembly and the back iron of the MMA. The off-axis attraction forces must be small enough to be resisted by the off-axis stiffness of a flexure bearing with axial stiffness K_x.

In the design of the single-axis, MMA-driven, flexure-based motion system that was constructed as a part of this thesis, diaphragm-type flexures were used, in part, because of the wide range of desirable axial and radial stiffness values that this flexure can be designed to provide. Hence, the actuator level design specification of reasonably small off-axis attraction forces between the permanent magnet in the MMA mover assembly and the back iron of the MMA could also be framed as a specification on the flexure design, in that flexure bearing must have the desired axial stiffness, as well as a minimum off-axis stiffness that is large enough to resist the off-axis attraction forces between the permanent magnet in the MMA mover assembly and the back iron of the MMA. When designing an MMA-driven, flexure-based motion system from scratch, the axial and radial stiffness constraints of the spring and the off-axis stiffness of a particular MMA design should be considered in tandem to ensure that the MMA and the spring bearing are compatible with one another. This is typically not a problem in the design of high performance motion systems with large natural frequencies because such systems require that the bearing have a large axial stiffness which, in flexure bearings, tends to correspond with a large radial stiffness [23].

2.2.2 Analysis of the motion system's equation of motion for a point-to-point positioning motion profile

Point-to-point positioning motion profiles are employed in applications in which it is desired to move the motion system's motion stage from one location to another location (e.g. hole operations such as drilling, boring, and reaming) in a typically aperiodic manner. The nature of a specific point-to-point positioning motion profile depends on the application. Presented below is a quantitative analysis of a single-axis, MMA-driven, flexure-based motion system carrying out the commonly used point-to-point positioning, *triangular velocity motion profile* shown in Figure 8.

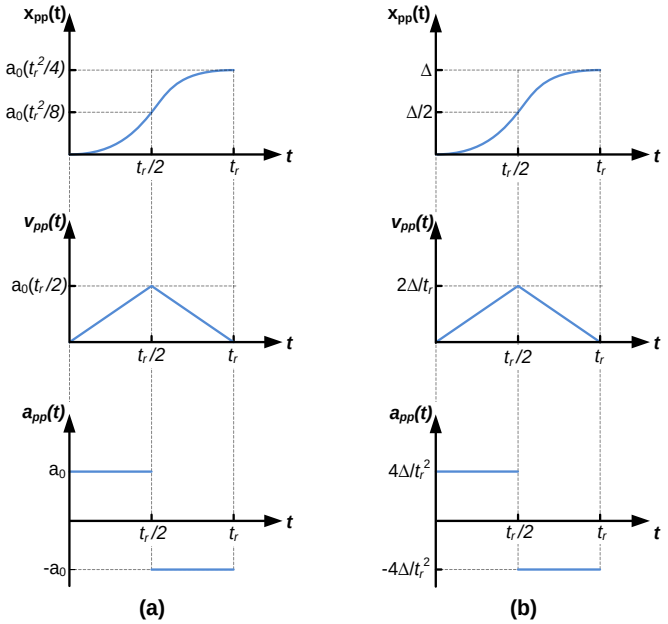

Figure 8: The position ($x_{pp}(t)$), velocity ($v_{pp}(t)$), and acceleration ($a_{pp}(t)$) profiles of the point-to-point positioning, triangular velocity motion profile. Figure 8(a) shows the expressions for the acceleration, velocity, and displacement values at times, $t = \frac{t_r}{2}$ and $t = t_r$, as a function of a_0, the magnitude of the acceleration, and t_r, the total traverse time. Figure 8(b) shows the expressions for the acceleration, velocity, and displacement values at times, $t = \frac{t_r}{2}$ and $t = t_r$, as a function of Δ, the total distance traversed during the move, and t_r, the total traverse time.

The triangular velocity motion profile in Figure 8 is characterized by a velocity motion profile of constant positive acceleration throughout the first half of the total distance traveled by the motion stage, followed by a velocity motion profile of constant negative acceleration throughout the second half of the total distance traveled by the motion stage distance. The accelerations in each half of the triangular velocity motion profile are of opposite

sign but equal in magnitude. The acceleration, velocity, and displacement motion profiles characteristic of the triangular velocity motion profile can be expressed as follows,

$$a_{pp}(t) \begin{cases} = a_0 & \text{for } \left(0 \le t \le \frac{t_r}{2}\right) \\ = -a_0 & \text{for } \left(\frac{t_r}{2} < t \le t_r\right), \end{cases} \tag{23}$$

$$v_{pp}(t) \begin{cases} = a_0 t & \text{for } \left(0 \le t \le \frac{t_r}{2}\right) \\ = a_0\left(t_r - t\right) & \text{for } \left(\frac{t_r}{2} < t \le t_r\right), \end{cases} \tag{24}$$

$$x_{pp}(t) \begin{cases} = \frac{1}{2} a_0 t^2 & \text{for } \left(0 \le t \le \frac{t_r}{2}\right) \\ = a_0\left(t t_r - \frac{1}{2}t^2 - \frac{1}{4}{t_r}^2\right) & \text{for } \left(\frac{t_r}{2} < t \le t_r\right), \end{cases} \tag{25}$$

where a_0 is the magnitude of the acceleration and t_r is the time it takes to travel from the origin of the travel path to the end of the travel path. Letting Δ be the distance covered during the move profile,

$$\Delta = x_{pp}(t_r) = \frac{1}{4} a_0 {t_r}^2. \tag{26}$$

The magnitude of the acceleration, a_0, can then be expressed in terms of Δ,

$$a_0 = \frac{4\Delta}{{t_r}^2}. \tag{27}$$

Substituting this expression of a_0 into Equations (23)-(25), the displacement, velocity, and acceleration motion profiles associated with the triangular velocity motion profile can be expressed as follows,

$$a_{pp}(t) \begin{cases} = \frac{4\Delta}{{t_r}^2} & \text{for } \left(0 \le t \le \frac{t_r}{2}\right) \\ = -\frac{4\Delta}{{t_r}^2} & \text{for } \left(\frac{t_r}{2} < t \le t_r\right), \end{cases} \tag{28}$$

$$v_{pp}(t) \begin{cases} = \frac{4\Delta}{{t_r}^2} t & \text{for } \left(0 \le t \le \frac{t_r}{2}\right) \\ = \frac{4\Delta}{{t_r}^2}\left(t_r - t\right) & \text{for } \left(\frac{t_r}{2} < t \le t_r\right), \end{cases} \tag{29}$$

$$x_{pp}(t) \begin{cases} = 2\Delta\left(\dfrac{t}{t_r}\right)^2 & \text{for } \left(0 \le t \le \dfrac{t_r}{2}\right) \\ = \Delta\left(-2\left(\dfrac{t}{t_r}\right)^2 + 4\left(\dfrac{t}{t_r}\right) - 1\right) & \text{for } \left(\dfrac{t_r}{2} < t \le t_r\right). \end{cases} \tag{30}$$

It follows from Equation (1) and Equations (28)-(30) that the actuator must output the following force waveforms to sustain the point-to-point positioning, triangular velocity motion profile,

$$F_{pp}(t) \begin{cases} = \left(m_m + m_p\right)\Delta\omega_n^{\,2}\left(2\left(\dfrac{t}{t_r}\right)^2 + \dfrac{4}{\left(\omega_n t_r\right)^2}\right) & \text{for } \left(0 \le t \le \dfrac{t_r}{2}\right) \\ = \left(m_m + m_p\right)\Delta\omega_n^{\,2}\left(-2\left(\dfrac{t}{t_r}\right)^2 + 4\left(\dfrac{t}{t_r}\right) - 1 - \dfrac{4}{\left(\omega_n t_r\right)^2}\right) & \text{for } \left(\dfrac{t_r}{2} < t \le t_r\right). \end{cases} \tag{31}$$

Equation (31) implies that for an actuator to sustain the triangular velocity motion profile, its maximum force output, $F_{a,max}$, has to be greater than or equal to the maximum magnitude of force associated with the force waveforms in Equation (31).

$$F_{a,\max} \ge \left|F_{pp}\right|_{\max}. \tag{32}$$

In what follows below, it will be shown that, out of the two force waveforms in Equation (31), the one that is associated with the maximum magnitude of force varies depending on the product of the travel time of the move, t_r, and the natural frequency of the system, ω_n. To facilitate the discussion, the two force profiles in Equation (31) are renamed as follows,

$$F_{pp1}(t) = \left(m_m + m_p\right)\Delta\omega_n^{\,2}\left(2\left(\frac{t}{t_r}\right)^2 + \frac{4}{\left(\omega_n t_r\right)^2}\right) \quad \text{for } \left(0 \le t \le \frac{t_r}{2}\right), \tag{33}$$

$$F_{pp2}(t) = \left(m_m + m_p\right)\Delta\omega_n^{\,2}\left(-2\left(\frac{t}{t_r}\right)^2 + 4\frac{t}{t_r} - 1 - \frac{4}{\left(\omega_n t_r\right)^2}\right) \quad \text{for } \left(\frac{t_r}{2} < t \le t_r\right), \tag{34}$$

where $F_{pp1}(t)$ is the actuator force profile required to carry out the first leg of the triangular velocity motion profile, and $F_{pp2}(t)$ is the actuator force profile required to carry out the second leg of the triangular velocity motion profile. By the end of the discussion, it will be shown that the maximum magnitude of force the actuator is required to output to sustain the triangular velocity motion profile is,

$$\left|F_{pp}\right|_{\max} \begin{cases} = F_{pp1}\left(\dfrac{t_r}{2}\right) = \Delta\left(m_m + m_p\right)\left(\dfrac{1}{2}\omega_n^{\,2} + \dfrac{4}{t_r^{\,2}}\right) & \text{for } \left(0 < (\omega_n t_r) \le 4\right), \\ = F_{pp2}\left(t_r\right) = \Delta\left(m_m + m_p\right)\left(\omega_n^{\,2} - \dfrac{4}{t_r^{\,2}}\right) & \text{for } \left((\omega_n t_r) \ge 4\right). \end{cases} \tag{35}$$

The maximum magnitude of force associated with $F_{pp1}(t)$ can be identified by inspection. The magnitude of the function increases as a function of time regardless of the magnitude of the other parameters that $F_{pp1}(t)$ is a function of, implying that its maximum occurs at time, $t = \frac{t_r}{2}$,

$$\left|F_{pp1}\right|_{\max} = F_{pp1}\left(\frac{t_r}{2}\right) = \Delta\left(m_m + m_p\right)\omega_n{}^2\left(\frac{4}{\left(\omega_n t_r\right)^2} + \frac{1}{2}\right). \tag{36}$$

To identify the maximum magnitude of force associated with $F_{pp2}(t)$, it is first established that the maximum magnitude of $F_{pp2}(t)$ occurs at either $t = \frac{t_r}{2}$ or $t = t_r$, regardless of the magnitude of the other parameters that $F_{pp2}(t)$ is a function of. The expression for the magnitude of $F_{pp2}(t)$ is as follows,

$$\left|F_{pp2}(t)\right| = \Delta\left(m_m + m_p\right)\omega_n{}^2\sqrt{\left(-2\left(\frac{t}{t_r}\right)^2 + 4\frac{t}{t_r} - 1 - \frac{4}{\left(\omega_n t_r\right)^2}\right)^2} \quad \text{for } \left(\frac{t_r}{2} < t \le t_r\right). \tag{37}$$

Dividing both sides of Equation (37) by the sum of the moving masses, (m_m+m_p), the travel distance, Δ, and the square of the natural frequency, $\omega_n{}^2$, and dividing the time bound inequality for which the equation applies by t_r,

$$\frac{\left|F_{pp2}(t)\right|}{\Delta\left(m_m + m_p\right)\omega_n{}^2} = \sqrt{\left(-2\left(\frac{t}{t_r}\right)^2 + 4\frac{t}{t_r} - 1 - \frac{4}{\left(\omega_n t_r\right)^2}\right)^2} \quad \text{for } \left(\frac{1}{2} \le \left(\frac{t}{t_r}\right) < 1\right). \tag{38}$$

Although the sum of the moving masses, the travel distance, and the square of the natural frequency should stay on the right hand side of the equation in determining the maximum magnitude of force associated with $F_{pp2}(t)$, the purpose of manipulating Equation (37) into Equation (38) is to establish the fact that the maximum magnitude of $F_{pp2}(t)$ occurs at either $t = \frac{t_r}{2}$ or $t = t_r$. This is shown in Figure 9 with plots of the right hand side of Equation (38) as a function of $\frac{t}{t_r}$ for several values of the product $(\omega_n t_r)$.

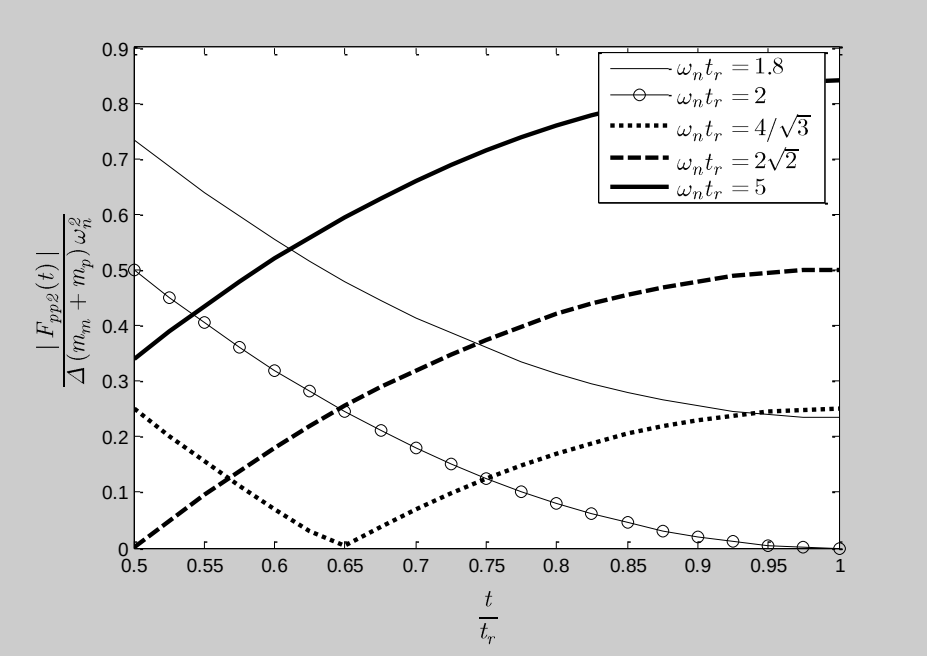

Figure 9: Plots of the right hand side of Equation (38) as a function of $\frac{t}{t_r}$ for several values of the product $(\omega_n t_r)$. The values of $(\omega_n t_r)$ for which the right hand side of Equation (38) is plotted serve to highlight the three distinct trends that the magnitude of $F_{pp2}(t)$ can display as function of $\frac{t}{t_r}$ depending on the value of $(\omega_n t_r)$.

The plots in Figure 9 are representative of the three distinct trends the magnitude of $F_{pp2}(t)$ can take on depending on the magnitude of $(\omega_n t_r)$. For $0 < (\omega_n t_r) \leq 2$, the magnitude of $F_{pp2}(t)$ has a negative slope throughout the entire motion profile, beginning at its maximum at $t = \frac{t_r}{2}$ and decreasing to its minimum at $t = t_r$. For $2 < (\omega_n t_r) < 2\sqrt{2}$, the magnitude of $F_{pp2}(t)$ begins with a negative slope and decreases to zero over some time, $t < t_r$, and then increases in magnitude for the rest of the time, showing that the maximum of the function occurs at either $t = \frac{t_r}{2}$ or $t = t_r$. For $(\omega_n t_r) \geq 2\sqrt{2}$, the magnitude of $F_{pp2}(t)$ has a positive slope throughout the entire motion profile, beginning at its minimum at $t = \frac{t_r}{2}$ and increasing to its maximum at $t = t_r$. The only factor that determines the trend of the magnitude of $F_{pp2}(t)$ as described above is the magnitude of $(\omega_n t_r)$. Variations to the mass of the permanent magnet, the mass of the payload, the travel distance, the travel time, and the natural frequency of the system can have a large impact on the magnitude of $F_{pp2}(t)$, but as long as the magnitude of $(\omega_n t_r)$ stays within the same bound of $(\omega_n t_r)$ as before the variations, the trend of $F_{pp2}(t)$ will remain unchanged.

Having established that the maximum magnitude of $F_{pp1}(t)$ occurs at $t = \frac{t_r}{2}$ and that the maximum magnitude of $F_{pp2}(t)$ occurs at either $t = \frac{t_r}{2}$ or $t = t_r$, the only magnitudes of force to consider when identifying the maximum magnitude of $F_{pp}(t)$ are the magnitudes at those times. The expressions for the magnitude of force at those respective times are as follows,

$$\left| F_{pp1}\left(\frac{t_r}{2}\right)\right| = \Delta\left(m_m + m_p\right)\omega_n^{\,2}\left(\frac{1}{2} + \frac{4}{\left(\omega_n t_r\right)^2}\right), \tag{39}$$

$$\left| F_{pp2}\left(\frac{t_r}{2}\right)\right| = \Delta\left(m_m + m_p\right)\omega_n^{\,2}\sqrt{\left(\frac{1}{2} - \frac{4}{\left(\omega_n t_r\right)^2}\right)^2}, \tag{40}$$

$$\left|F_{pp2}\left(t_r\right)\right| = \Delta\left(m_m + m_p\right)\omega_n^{\,2}\sqrt{\left(1 - \frac{4}{\left(\omega_n t_r\right)^2}\right)^2}. \tag{41}$$

Equations (39)-(41) share as common factors the sum of the moving masses, the distance traveled, and the square of the first natural frequency. Dividing Equations (39)-(41) by their common factors gives,

$$\frac{\left| F_{pp1}\left(\frac{t_r}{2}\right)\right|}{\Delta\left(m_m + m_p\right)\omega_n^{\,2}} = \left(\frac{1}{2} + \frac{4}{\left(\omega_n t_r\right)^2}\right), \tag{42}$$

$$\frac{\left| F_{pp2}\left(\frac{t_r}{2}\right)\right|}{\Delta\left(m_m + m_p\right)\omega_n^{\,2}} = \sqrt{\left(\frac{1}{2} - \frac{4}{\left(\omega_n t_r\right)^2}\right)^2}, \tag{43}$$

$$\frac{\left|F_{pp2}\left(t_r\right)\right|}{\Delta\left(m_m + m_p\right)\omega_n^{\,2}} = \sqrt{\left(1 - \frac{4}{\left(\omega_n t_r\right)^2}\right)^2}. \tag{44}$$

implying that the force profile associated with the largest magnitude of force is the one that is associated with the largest magnitude of the right hand side of Equations (42)-(44). The right hand sides of Equations (42)-(44) are plotted as a function of $(\omega_n t_r)$ in Figure 10. The plots show that the maximum magnitude of force required to sustain the triangular force profile is $|F_{pp1}(t_r/2)|$ for $(\omega_n t_r) < 4$ and $|F_{pp2}(t_r)|$ for $(\omega_n t_r) > 4$.

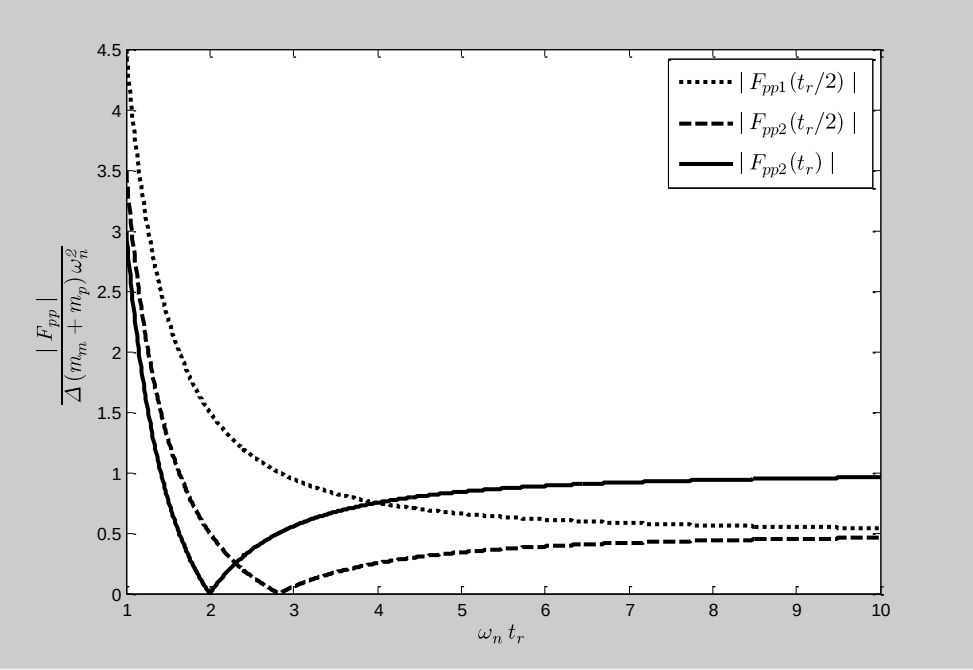

Figure 10: The right hand sides of Equations (42)-(44) plotted as a function of $(\omega_n t_r)$ show how the relative magnitudes of $F_{pp1}\left(\frac{t_r}{2}\right)$, $F_{pp2}\left(\frac{t_r}{2}\right)$, and $F_{pp2}(t_r)$ compare as a function of $(\omega_n t_r)$.

$$\left|F_{pp}\right|_{\max} \begin{cases} = F_{pp1}\left(\frac{t_r}{2}\right) = \Delta\left(m_m + m_p\right)\left(\frac{1}{2}\omega_n{}^2 + \frac{4}{t_r{}^2}\right) & \text{for } \left(0 < \left(\omega_n t_r\right) \le 4\right), \\ = F_{pp2}\left(t_r\right) = \Delta\left(m_m + m_p\right)\left(\omega_n{}^2 - \frac{4}{t_r{}^2}\right) & \text{for } \left(\left(\omega_n t_r\right) \ge 4\right). \end{cases} \tag{45}$$

A physical interpretation of the expressions for $F_{pp1}\left(\frac{t_r}{2}\right)$ and $F_{pp2}(t_r)$ provides insight as to why the magnitude of $(\omega_n t_r)$ determines which of the triangular velocity force profiles is associated with the maximum magnitude of force.

$$F_{pp1}\left(\frac{t_r}{2}\right) = \Delta\left(m_m + m_p\right)\left(\frac{1}{2}\omega_n{}^2 + \frac{4}{t_r{}^2}\right), \tag{46}$$

$$F_{pp2}\left(t_r\right) = \Delta\left(m_m + m_p\right)\left(\omega_n{}^2 - \frac{4}{t_r{}^2}\right). \tag{47}$$

The magnitude of the coefficients of $\omega_n{}^2$ imply that the actuator force output required to overcome the spring forces at $t = \frac{t_r}{2}$ is just half of what is required to overcome the spring forces at $t = t_r$. This makes physical sense as the motion stage is at the halfway point of the the total travel distance at time, $t = \frac{t_r}{2}$. Further comparison of $F_{pp1}\left(\frac{t_r}{2}\right)$ and $F_{pp2}(t_r)$, however, shows that there is an additional positive force output that the actuator must provide at $t = \frac{t_r}{2}$ to support the positive acceleration of the motion stage, while at $t = t_r$, there is an additional negative force output that the actuator must provide at $t = t_r$ to support the negative acceleration of the motion stage. The magnitude of the forces required to support the positive and negative acceleration depends on the inverse square of t_r, while the magnitude of forces required to overcome the spring force depends on the square of ω_n. Hence, holding ω_n constant and making t_r smaller causes the magnitude of $F_{pp1}\left(\frac{t_r}{2}\right)$ to become greater than the magnitude of $F_{pp2}(t_r)$, while

holding t_r constant and making ω_n larger causes the magnitude of $F_{pp2}(t_r)$ to become greater than the magnitude of $F_{pp1}\left(\frac{t_r}{2}\right)$. This behavior is reflected in the plots in Figure 10.

The plots in Figure 10 show that, for $(\omega_n t_r) < 4$, the magnitude of the sum of the positive force required to overcome the spring forces at $t = \frac{t_r}{2}$ and the positive force required to support the positive acceleration of the motion stage, i.e., $|F_{pp1}\left(\frac{t_r}{2}\right)|$, is greater than the magnitude of the sum of the positive force required to overcome the spring forces at $t = t_r$ and the negative force required to support the negative acceleration of the motion stage, i.e., $|F_{pp2}(t_r)|$, and vice versa for $(\omega_n t_r) > 4$. The trends imply that, for $(\omega_n t_r) > 4$, the maximum magnitude of the triangular velocity force profiles is predominantly due to having to overcome the spring forces, while for $(\omega_n t_r) < 4$, the maximum magnitude of the triangular velocity force profiles is predominantly due to having to move the moving masses at the desired positive acceleration.

The above mentioned behavior is also highlighted in Figure 11 which shows plots of the right hand side of Equation (48) as a function of time for a given travel time of $t_r = 1\ [s]$ and several values of ω_n.

$$\frac{F_{pp}(t)}{\left(m_m + m_p\right)\Delta} = \begin{cases} \omega_n^2\left(2\left(\dfrac{t}{t_r}\right)^2 + \dfrac{4}{\left(\omega_n t_r\right)^2}\right) & \text{for } \left(0 \le t \le \dfrac{t_r}{2}\right) \\ \omega_n^2\left(-2\left(\dfrac{t}{t_r}\right)^2 + 4\left(\dfrac{t}{t_r}\right) - 1 - \dfrac{4}{\left(\omega_n t_r\right)^2}\right) & \text{for } \left(\dfrac{t_r}{2} < t \le t_r\right). \end{cases} \tag{48}$$

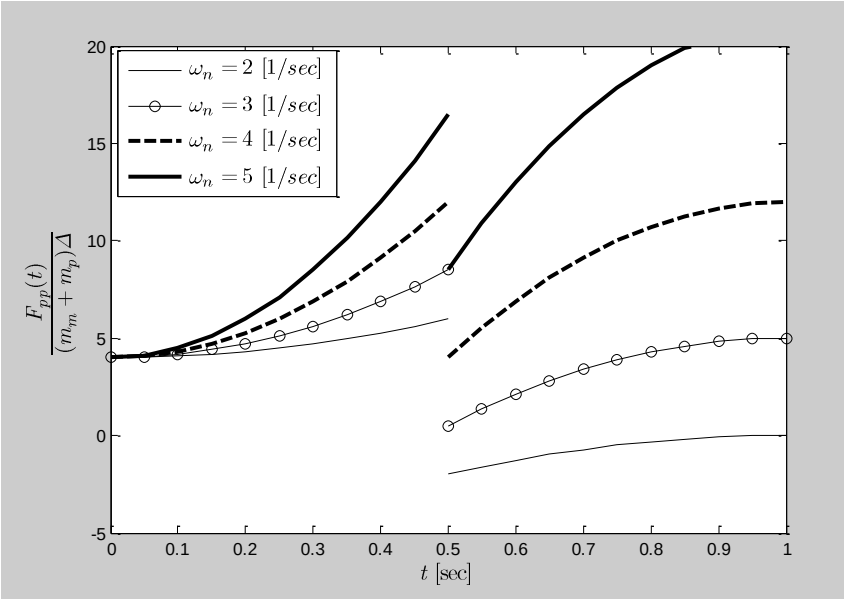

Figure 11: Plots of the right hand side of Equation (48) as a function of time for a given travel time of $t_r = 1\ [s]$ and several values of ω_n.

The plots illustrate the effect that the desired negative acceleration of the second half of the motion profile has on the corresponding force output required to support the negative acceleration. Recall that the negative term in the expression for $F_{pp2}(t_r)$ in Equation (47) supports the desired negative acceleration of the second half of the motion profile. The addition of this negative term means that the actuator does not have to output a force equal to or greater than the positive force required to overcome the spring forces at any given time. Instead, the actuator has to provide a force with the sign and magnitude such that the sum of the actuator force output and spring force results in the moving masses moving with the desired negative acceleration associated with the second half of the triangular velocity motion profile. This can be seen more clearly by rearranging Equation (47) and expressing it as follows,

$$F_{pp2}(t_r) - \omega_n{}^2 \Delta\left(m_m + m_p\right) = -\frac{4}{t_r{}^2}\Delta\left(m_m + m_p\right). \tag{49}$$

The plots in Figure 11 illustrate the effect of increasing the natural frequency of the system while the travel time is kept constant. As the natural frequency increases, the positive force output required to resist the spring's restoring force grows larger. Even though the actuator output force is less than the positive force required to achieve equilibrium with the spring, the force is still positive and greater than the force in the first half of the movement because without that force, the restoring force of the spring would cause the motion stage to return to the origin at too large of a negative acceleration.

With respect to performance, both of the possible expressions for $|F_{pp}|_{max}$, restated below in Equation (50) for convenience,

$$\frac{\left|F_{pp}\right|_{\max}}{\left(m_m + m_p\right)} \begin{array}{ll} = \dfrac{F_{pp1}\left(\dfrac{t_r}{2}\right)}{\left(m_m + m_p\right)} = \Delta\left(\dfrac{1}{2}\omega_n{}^2 + \dfrac{4}{t_r{}^2}\right) & \text{for } \left(0 < \left(\omega_n t_r\right) \le 4\right), \\ = \dfrac{F_{pp2}(t_r)}{\left(m_m + m_p\right)} = \Delta\left(\omega_n{}^2 - \dfrac{4}{t_r{}^2}\right) & \text{for } \left(\left(\omega_n t_r\right) \ge 4\right), \end{array} \tag{50}$$

show how the quotient of the maximum force output of the actuator and the sum of the actuator and payload masses places an upper bound on the degree to which the motion can simultaneously achieve a large motion range (as captured by Δ), high speed (i.e. small t_r), and high open-loop bandwidth (as captured by ω_n) in an MMA-driven, flexure-based motion system. This quotient, however, is lacking when considered as a figure of merit with which to evaluate and design actuators for high performance motion systems [5]. A better figure of merit would solely be a function of actuator properties. It would be representative of the inherent performance of the actuator regardless of payload mass. In addition, the quotient does not offer an obvious way to incorporate any potential power constraints imposed by either the maximum heat removal capability of the motion system's thermal management system, the maximum power input of the driver, or the maximum power input that the driver can deliver without introducing unacceptably high levels of electrical noise and signal distortion. To address these shortcomings, the dynamic actuator constant is incorporated into Equation (50), leading to conclusions similar to the conclusions that were arrived at during the analysis of the equation of motion for the raster scanning motion profile.

It is shown in Appendix A that the time at which the point-to-point positioning motion profile demands the maximum force output of the actuator, $F_{a0,max}$, coincides with the time at which the actuator's power consumption of is at a maximum, $P_{a0,max}$, implying that the dynamic actuator constant for a given actuator can be expressed as follows,

$$\beta_0 = \frac{F_{a0,\max}}{\sqrt{P_{a0,\max}}\sqrt{m_{m0}}}, \tag{51}$$

which, in turn, implies that,

$$F_{a0,\max} = \beta_0 \sqrt{P_{a0,\max}}\sqrt{m_{m0}}\ . \tag{52}$$

Substituting Equation (54) into Equation (50) shows that,

$$\frac{\beta_0\sqrt{P_{a0,\max}}\sqrt{m_{m0}}}{\left(m_{m0}+m_{p0}\right)} \quad \begin{array}{ll} = \dfrac{F_{pp1}\left(\dfrac{t_r}{2}\right)}{\left(m_m+m_p\right)} = \Delta\left(\dfrac{1}{2}{\omega_n}^2+\dfrac{4}{{t_r}^2}\right) & \text{for } \left(0<\left(\omega_n t_r\right)\le 4\right), \\ = \dfrac{F_{pp2}\left(t_r\right)}{\left(m_m+m_p\right)} = \Delta\left({\omega_n}^2-\dfrac{4}{{t_r}^2}\right) & \text{for } \left(\left(\omega_n t_r\right)\ge 4\right). \end{array} \tag{53}$$

Collecting the range, open-loop bandwidth, travel time, and power consumption terms on one side of the equation and the mass terms and dynamic actuator constant term on the other side of the equation shows that,

$$\beta_0 \cdot \frac{\sqrt{m_{m0}}}{\left(m_{m0}+m_{p0}\right)} \quad \begin{array}{ll} = \Delta \cdot \left(\dfrac{1}{2}{\omega_n}^2+\dfrac{4}{{t_r}^2}\right)\cdot \dfrac{1}{\sqrt{P_{a0,\max}}} & \text{for } \left(0<\left(\omega_n t_r\right)\le 4\right), \\ = \Delta \cdot \left({\omega_n}^2-\dfrac{4}{{t_r}^2}\right)\cdot \dfrac{1}{\sqrt{P_{a0,\max}}} & \text{for } \left(\left(\omega_n t_r\right)\ge 4\right). \end{array} \tag{54}$$

which implies that,

$$\beta_0 \cdot M_{dynamic0} \quad \begin{array}{ll} = \Delta \cdot \left(\dfrac{1}{2}{\omega_n}^2+\dfrac{4}{{t_r}^2}\right)\cdot \dfrac{1}{\sqrt{P_{a0,\max}}} & \text{for } \left(0<\left(\omega_n t_r\right)\le 4\right), \\ = \Delta \cdot \left({\omega_n}^2-\dfrac{4}{{t_r}^2}\right)\cdot \dfrac{1}{\sqrt{P_{a0,\max}}} & \text{for } \left(\left(\omega_n t_r\right)\ge 4\right). \end{array} \tag{55}$$

Equation (55) quantitatively captures the system level performance limitations associated with the actuator component of the system, showing how the product of the actuator's dynamic actuator constant and dynamic mass quantity places an upper bound on the maximum performance of the system, thus imposing system level performance tradeoffs between the motion range (as captured by Δ), open-loop bandwidth (as captured by ω_n), traverse time (as captured by t_r), and power consumption (as captured by P) of the system. Analysis of Equation (55) in the context of a power constraint, $P_{a0,max}$, shows that the level to which one can simultaneously achieve large range, small traverse time, and high open-loop bandwidth is limited by the product of the actuator's dynamic actuator constant and the dynamic mass quantity. Hence, when designing a high performance MMA, one should aim to maximize the product of its dynamic actuator constant and dynamic mass quantity. One can conduct a similar analysis for a simple mass, no spring, single-axis, MMA-driven motion system and arrive at similar conclusions.

2.3 Performance implications of the dynamic mass quantity

Analysis of the single-axis, MMA-driven, flexure-based motion system's equation of motion for a point-to-point positioning motion profile and a raster scanning motion profile showed that the magnitude of an MMA's dynamic actuator constant alone does not place an upper bound on the performance of the motion system. Instead, the product of the actuator's dynamic actuator constant and the dynamic mass quantity, deemed the *performance metric* (*PM*), where,

$$PM \triangleq \beta \cdot M_{dynamic} = \frac{K_t}{\sqrt{R}} \cdot \frac{1}{m_m+m_p} \cdot \tag{56}$$

The performance metric places an upper bound on the performance the motion system is capable of. Prior work has recognized the significance of the dynamic actuator constant but not the dynamic mass quantity [1]. Analysis of the dynamic mass quantity, presented below, reveals the implications of the dynamic mass quantity on system performance and actuator design.

The dynamic mass quantity is defined in Equation (18) and is stated again in Equation (57) for convenience.

$$M_{dynamic} \triangleq \frac{\sqrt{m_m}}{m_m + m_p} \quad . \tag{57}$$

After some algebraic manipulation, the dynamic mass quantity can be further expressed as follows in Equation (58) and Equation (59).

$$M_{dynamic} = \frac{1}{\sqrt{m_m}} \frac{1}{\left(\frac{m_p}{m_m}\right)+1} \quad . \tag{58}$$

$$M_{dynamic} = \frac{1}{\sqrt{m_p}} \frac{\sqrt{\left(\frac{m_m}{m_p}\right)}}{\left(\frac{m_m}{m_p}\right)+1} \quad . \tag{59}$$

Examination of Equation (57) and Equation (58) is useful for understanding the behavior of $M_{dynamic}$ for a fixed magnet mass, m_m, and varying payload mass, m_p. From Equation (57) it is evident that, given a magnet mass, m_{m0}, the maximum of $M_{dynamic}$ is $\frac{1}{\sqrt{m_{m0}}}$, occurring when m_p equals zero. An m_p value larger than zero will increase the magnitude of the denominator while leaving the numerator unaffected. This is also evident when examining Equation (58). In Equation (58), a given magnet mass, m_{m0}, fixes the first term in the equation; the second term in the equation varies with m_p and is at a maximum when m_p equals zero. As m_p increases from a starting value of zero, the second term in Equation (58) decreases from its starting maximum value, resulting in a decreasing $M_{dynamic}$. It can then be concluded that, regardless of the value of a fixed m_m, the magnitude of $M_{dynamic}$ increases as m_p decreases.

The trends described above can be seen in Figure 12 in a plot of $M_{dynamic}$ as a function of m_m for several values of m_p. It can also be concluded from Figure 12 as well as Equation (58) that if m_p is unknown, one cannot be certain as to what magnitude of m_m will maximize $M_{dynamic}$. While a magnet mass, m_m=0.1[kg] will maximize $M_{dynamic}$ for a payload mass, m_p=0.1[kg], a magnet mass, m_m=0.1[kg] would not maximize $M_{dynamic}$ for a payload mass, m_p=0.5[kg]. The plot also shows that, for any given fixed m_m, $M_{dynamic}$ increases as m_p decreases.
Equation (58) also shows that, for $m_m >> m_{p0}$,

$$M_{dynamic} \approx \frac{1}{\sqrt{m_m}} \quad , \tag{60}$$

which implies that, for $m_m >> m_{p0}$, $M_{dynamic}$ increases as m_m decreases.

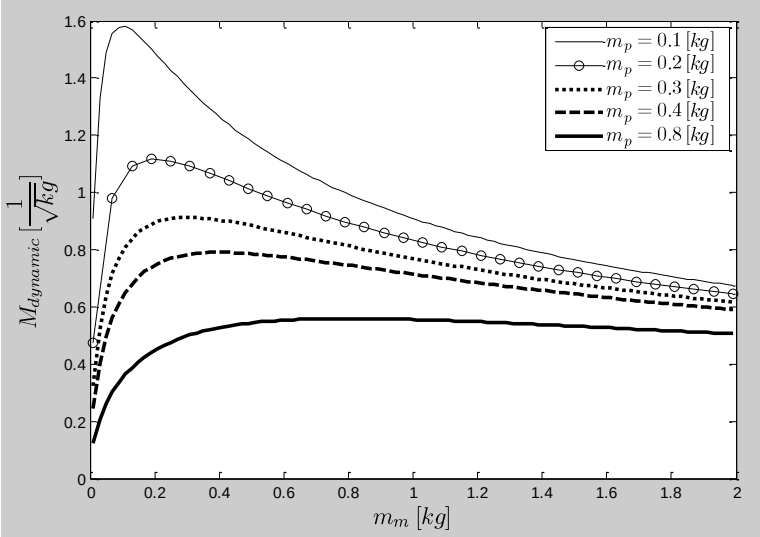

Figure 12: The dynamic mass quantity, $M_{dynamic}$, as a function of magnet mass, m_m, for various payload mass values, m_p.

The maximum of $M_{dynamic}$ (for a fixed payload mass, m_{p0}) can be obtained by taking the derivative of $M_{dynamic}$ with respect to m_m, solving for the m_m that makes the derivative equal to zero, and substituting this m_m back into the original expression of $M_{dynamic}$. As was stated at the end of Section 2.2.1 (Equation (55)), the derivative of $M_{dynamic}$ with respect to m_m is,

$$\frac{d}{dm_m} M_{dynamic} = \frac{m_{p0} - m_m}{2\sqrt{m_m}\left(m_m + m_{p0}\right)^2}, \tag{61}$$

Equation (61) shows that the derivative of $M_{dynamic}$ with respect to m_m is zero when m_m is equal to m_{p0}, implying that the maximum of $M_{dynamic}$ (for a fixed, non-zero m_{p0}) is,

$$M_{dynamic,\max} = \frac{\sqrt{m_{p0}}}{m_{p0} + m_{p0}} = \frac{1}{2\sqrt{m_{p0}}}, \tag{62}$$

Equation (62) implies that the upper bound of the maximum achievable $M_{dynamic}$ is dictated by the magnitude of m_{p0}.

Figure 13 shows a plot of $M_{dynamic}$ as a function of the ratio $\frac{m_m}{m_p}$ (the right hand side of Equation (59)) for several values of m_p. Each $M_{dynamic}$ curve corresponds to a different m_p value.

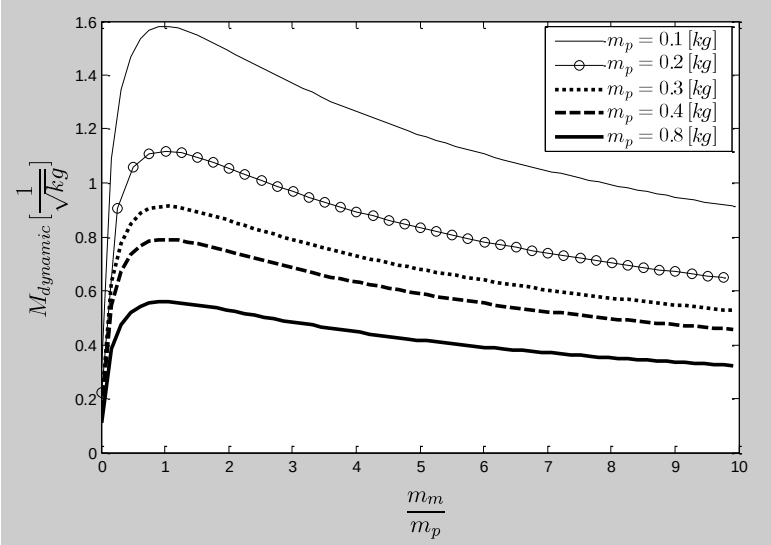

Figure 13: $M_{dynamic}$ as a function of the ratio, $\frac{m_m}{m_p}$, for various m_p values.

As expected, it shows that, given a non-zero m_{p0}, the maximum value of $M_{dynamic}$ occurs when the ratio, $\frac{m_m}{m_p}$, is equal to one (i.e. when m_m is equal to m_{p0}). For any given fixed ratio, $\frac{m_m}{m_p}$, $M_{dynamic}$ increases as m_p decreases. Figure 13 also shows that, given an m_{p0}, the magnitude of $M_{dynamic}$ will begin to decrease from its maximum value as the magnitude of m_m begins to stray from the magnitude of m_{p0}. This can also be seen in Figure 12.

The above analysis shows that the magnitudes of the magnet and payload masses, via the dynamic mass quantity, have a significant effect on actuator and system level performance. The analysis shows that maximizing the dynamic actuator constant of an MMA alone is not the appropriate strategy for maximizing system performance. The dynamic actuator constant is still a good figure of merit, however, as it is representative of the maximum force an MMA can output for a given permanent magnet mass and power input. Maximizing the dynamic mass quantity of an MMA alone is also not an appropriate strategy for maximizing an MMA's performance. It is important, however, to have an understanding of the implications of the dynamic mass quantity on the design and performance of high performance motion systems and Lorentz force actuators. The following design insights can be derived from the analysis above:

1. Given an actuator and the task of designing a flexure-based motion system around the actuator to maximize the system's dynamic performance:
   a. The dynamic actuator constant and m_m are given and they are fixed.
   b. The peak dynamic performance of the system (captured by *PM*, the performance metric) occurs when m_p is equal to zero and decreases as m_p increases, implying that one should minimize m_p to maximize performance.

2. Given a motion system and the design of an actuator that has been optimized to maximize its dynamic actuator constant, the following should be taken into consideration to maximize the system's dynamic performance:
   a. m_p, the payload mass, is a given and is fixed.
   b. Although the magnitude of the dynamic mass quantity varies as the magnet mass varies, the dynamic actuator constant is invariant to the scaling of its geometry. This invariance to scaling, however, has limits due to real world constraints. As the actuator geometry is scaled down there comes a point where the mechanical air gap thickness of the actuator can no longer be scaled down with the rest of the geometric parameters that define the MMA's geometry. This is due to fabrication as well as assembly tolerances and constraints. This constraint causes the dynamic actuator constant of the MMA to decrease as it is scaled down past this point. Another important caveat to take note of is that, when a given actuator design is optimized for a maximum dynamic actuator constant, the optimization is done so for a specific motion range. As the actuator's geometry is scaled up or down in size, so does the geometric parameter associated with the stroke. If the scaled stroke parameter of a scaled MMA design is not close to the desired stroke of the

motion system, the above described strategy of maximizing system performance may not be applicable.

c. Assuming that the dynamic actuator constant is constant as it is scaled up or down in size, the dynamic mass quantity, and hence the performance metric, is maximum when m_m becomes equal to m_p.
d. If m_m is large due to the geometry of the actuator design, the actuator design should be scaled down in size until m_m becomes equal to m_p. If the actuator is made too small, however, the constraint of a minimum air gap thickness will cause its dynamic actuator constant to decrease. Scaling down the actuator to the point where its dynamic actuator constant begins to decrease may still be the appropriate design decision if the performance metric continues to increase due to the increasing dynamic mass quantity. Note here that it is assumed that scaled geometric parameter of stroke that corresponds to the scaled MMA geometry is close to the magnitude of the stroke that is specified by the system level performance specifications of the motion system.
e. If m_m is small, the actuator should be scaled up in size so that m_m becomes equal to m_p. This should preserve the dynamic actuator constant (remains constant with size) while increasing the dynamic mass quantity, resulting in better overall system performance. Like above, it is assumed that that scaled geometric parameter of stroke is close to the magnitude of the stroke that is specified by the system level performance specifications of the motion system. The extent to which the scaling of the stroke can negatively impact motion system performance for cases like described in this list has yet to be fully explored.
f. If m_p is unknown, one cannot be certain as to how magnitude of m_m will effect $M_{dynamic}$ and hence performance.

3. All of the above assume that the air gap thickness and stroke length of the actuator are being scaled up or down in size along with the rest of the actuator. If the stroke length is held constant at some desired value, and the air gap thickness is held at its minimum value, as the actuator is scaled up, the dynamic actuator constant would increase. At the same time, as the actuator is scaled up, the dynamic mass quantity would decrease in value. This is one of many tradeoffs to take into consideration during the design of high performance MMA-driven motion systems. It exemplifies the need for a multi-objective or iterative optimization approach for designing an MMA.

4. If allowed to start on a clean slate, i.e. design the system and the actuator simultaneously, then,

a. The above steps should be done concurrently (multi-objective or iterative optimization)
b. Independent of the actuator, m_p should be minimized

CHAPTER 3

3 A review of MMA prior art

The concentric coil, radial magnet MMA belongs to a broad class of MMAs that are distinguished by their two-terminal, non-commutated, and single-phase excitation windings; such MMAs are commonly used in direct-drive applications [23]. This chapter provides an overview of several of the unique MMA architectures associated with the MMAs that span this space. Each architecture is presented with a schematic of its cross-section, a description of its basic operating principles, and a brief discussion of the architecture's merit (advantages and disadvantages) as a high performance MMA. An exception to the brevity of discussion is made for the much better performance that has been demonstrated by the traditional MMA architecture that is commercially-available [5][17]. The challenge of exceeding the performance of the traditional MMA architecture motivated the investigation into the optimal design of the concentric coil, radial magnet MMA and is hence discussed in depth.

The chapter is organized as follows. Section 3.1 describes several of the electromagnetic phenomena that tend to hinder the performance of an MMA. The performance of the various MMA architectures reviewed in this chapter is largely dependent on the degree to which the architecture's design attenuates the adverse effects associated with these electromagnetic phenomena. Section 3.2 is devoted to the traditional MMA architecture. Section 3.3 is devoted to MMA architectures other than the traditional one. Referred to as non-traditional architectures, these architectures have been reported in the prior literature but are typically not commercially available for various reasons. It should be noted that the non-traditional concentric coil, radial magnet MMA architecture is purposely omitted from this chapter. A review of that architecture is deferred to Section 5.2, in which many variations of the concentric coil, radial magnet MMA architecture are evaluated in order to identify the one with the highest potential performance.

3.1 Common electromagnetic phenomena harmful to MMA performance

This section reviews several common electromagnetic phenomena harmful to MMA performance. A more thorough and expansive review of the electromagnetic phenomena relevant to MMA design can be found in [5].

3.1.1 Fringing flux and leakage flux

The magnetic flux associated with the magnetic flux flow profile in electromagnetic actuators tends to display the undesirable behaviors of flux fringing and flux leakage as the flux passes through regions of high reluctance. Both flux fringing and flux leakage stem from the spreading and bulging behavior that flux displays as it passes through the high reluctance regions of the actuator (discounting the high reluctance region of the magnetic field source). Flux fringing refers to the spreading and bulging behavior that flux displays as it passes through the high reluctance regions it is intended to pass through [24]. The flux is said to "fringe" in this high reluctance region. Flux leakage refers to the spreading and bulging behavior that flux displays when it does not travel through the high reluctance region it is intended to pass through [24]. The flux is said to "leak" from the intended flux flow path.

In MMAs, the high reluctance region through which flux is intended to pass through comprises the coil winding and any other high reluctance component along the flux flow path between the magnet and the coil winding such as the portions of the mechanical air gap along the same lengthwise span of the coil winding and the coil bobbin thickness that houses the coil windings. This region of high reluctance is often referred to as the magnetic air gap, named as such because the components that comprise it have a magnetic permeability that is approximately equal to that of air. In general, the larger the magnetic air gap of an MMA, the more likely the magnetic flux is to fringe or leak.

In MMAs, any flux that passes through the coil windings at an angle other than one that is perpendicular to the direction of current in the coil windings is considered to be fringing flux. Flux that does not pass through the coil windings at all is considered to be leakage flux. Both phenomena can be seen in Table 3 in Section 5.2; a table which shows the flux field images of several of the different variations of the concentric coil, radial magnet MMA architecture that were evaluated for high performance. Flux fringing and flux leakage in MMAs result in lower magnetic flux densities in the coil region of the magnetic circuit as well as cosine losses from the lack of relative perpendicularity between the flux lines and the direction of current in the coil. The Lorentz force exerted on a current carrying conductor placed in a magnetic field is proportional to the dot product between the current vector

and the field vector. This implies that the force is proportional to the cosine of the angle between these two vectors: the force is maximum when the two vectors are orthogonal and zero when they are collinear.

3.1.2 Magnetic saturation

As in most electromagnetic actuators, the back iron of an MMA is made of ferromagnetic materials that have low hysteresis, such as carbon steel. This choice helps increase the magnetic flux density (i.e. B field) in response to an externally applied magnetic field intensity (i.e. H field) because the dipoles associated with the magnetic domains in the material line up with the external field. However, once all the dipoles have become aligned with the applied external field, there is no further increase in the flux density, resulting in magnetic flux saturation [25]. This magnetic saturation limits the maximum force output from the MMA for a given geometry/construction and a given current input.

3.1.3 Reluctance forces

Reluctance forces refer to the attractive forces that a ferromagnetic material experiences when it is subjected to a magnetic field. This attractive force acts in the direction that tends to minimize the net reluctance of the system [25]. In layman terms, this is simply the attractive force between a magnetic field (that may have been generated by a permanent magnet or electromagnet or a combination thereof) and a soft iron material. Reluctance forces tend to worsen the force-stroke uniformity of the MMA.

3.1.4 Armature reaction

The armature reaction phenomenon refers to the effect that an armature's magnetic field (i.e. the magnetic field induced by the coil in an MMA) has on the field magnet's magnetic field (i.e. the magnetic field induced by the permanent magnet in an MMA). The armature's magnetic field tends to distort the field magnet's magnetic field [25]. In MMAs, the armature reaction refers to the effect that the coil winding's magnetic field has on the permanent magnet's magnetic field. The armature reaction can cause undesirable reluctance forces (mentioned above) between the mover and stator of the MMA. It can also cause saturation in the back iron. Examples of the armature reaction acting as a major contributing factor to saturation in the back iron may be seen in Section 5.2 in the FEA simulation images of the magnetic flux density fields of concentric coil, radial magnet, MMA architecture variations 1, 2, and 5 in Table 3.

3.1.5 Joule heating

Joule heating refers to the generation of heat energy that occurs when a current passes through a conductor. In MMAs, the heat generated in the coil component can compromise the motion quality of the motion system via thermal expansion of the motion system's components and/or heat damage to the motion system's components. The heat generated in the coils can also cause the permanent magnet's temperature to rise above its curie temperature, which is the temperature at which the permanent magnet will lose its magnetization [26]. The role of the thermal management component of a motion system is to reject the heat that is generated in the coils.

3.2 The traditional MMA architecture

A cross section of the traditional MMA architecture shown previously in Figure 1 is shown again in Figure 14 for convenience. This traditional architecture is the basis of most commercially available MMAs. The cross section is taken along the motion axis of the architecture (the x-axis), highlighting the relative spatial orientation between the components that make up the MMA as well as the magnetic flux flow profile induced by the permanent magnet. The coordinate axis in the schematic is located at the center stroke position of the mover's range of motion. Note that the non-ferrous coupling structure connecting the mover to the motion stage is omitted from Figure 14.

In Figure 14 as well as other subsequent figures that show a cross-sectional schematic of various MMAs in this thesis, a consistent color scheme is used throughout. The color red denotes components made of permanent magnet; the color orange denotes current-carrying conductors; the color dark gray denotes ferromagnetic material; and the color light gray denotes non-ferromagnetic material. Using this color scheme to examine Figure 14, it is evident that the end cap and coil bobbin are made of non-ferromagnetic material, while the back iron and pole pieces are made of ferromagnetic material.

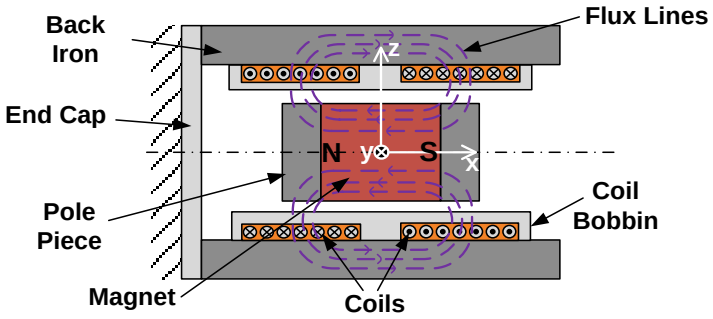

Figure 14: A cross-section of the traditional MMA architecture with the permanent magnet mover assembly at the center stroke position.

The architecture has several characteristics that contribute to its overall good performance. Firstly, it has two sets of coils wound in opposite directions. The oppositely wound coils induce magnetic flux fields of opposite direction, effectively canceling each other out. This characteristic negates the armature reaction and any of the adverse effects associated with it such as the reluctance force and saturation of the back iron. Secondly, the back iron component has a large cross sectional area through which the magnetic flux in the loop travels. This large cross-sectional surface area makes risk of saturation in the back iron small. Thirdly, the back iron of the traditional MMA architecture is simply constructed, easy to access, has a high thermal conductivity, and is in close contact with the coils, making it a good thermal interface for the thermal management system that rejects the joule heating in the coils. Risk of saturation in the pole pieces is high, but prior work has shown that the traditional MMA is capable of high performance without the use of pole pieces [1].

The traditional MMA architecture is not without disadvantages, however. The primary disadvantages are listed as follows:

1. The components of the architecture are arranged such that an axial reluctance force is induced between the permanent magnet and the back iron whenever the permanent magnet mover is at a position other than its center stroke position (indicated by the origin of the coordinate axes in Figure 14). This is because the reluctance of the magnetic circuit at the center stroke position is less than the reluctance at any other position for reasons that are explained in the next disadvantage described below. This reluctance force draws the permanent magnet towards the center stroke position, reducing the force-stroke uniformity of the actuator for a given input current. Reference [1] presents experimental data quantifying the effect of these axial reluctance forces on the force-stroke uniformity of a constructed traditional MMA [1]. The axial reluctance forces induced due to the traditional architecture's arrangement, however, are relatively small when compared to the reluctance forces induced in architectures with a significant armature reaction. Radial, off-axis reluctance forces are also present in this architecture. The magnet experiences off-axis forces towards the back iron, requiring that the components of the architecture be designed with tight mechanical tolerances that keep the components of the system as concentric as possible. Off-axis forces are inevitable, however; like with all MMAs, the permanent magnet mover is in an inherently unstable state, requiring that the actuator's bearings be designed to withstand the off-axis forces.
2. Another disadvantage of the traditional MMA architecture can be attributed to the relative spatial orientation between the permanent magnet's magnetization direction and the direction of current in the coil. The permanent magnet is spatially oriented such that the direction of flux flow emanating from and returning to its north and south poles, respectively, is parallel to the direction of current in the conductor, making for a relatively large magnetic air gap between the poles of the magnet and the low reluctance back iron. The arrangement results in flux fringing and leakage, as is apparent in the flux field images of the traditional MMA architecture shown in Figure 6.1 in David Hiemstra's M.S. thesis [5]. This leads to a non-trivial reduction in the actuator performance. The flux fringing and leakage are a result of the topology and the large magnetic air gap associated with it. The large air gap and the associated flux fringing and flux leakage reduce the force output of the actuator. The flux fringing and leakage phenomena also reduce the force-stroke uniformity of the actuator. This is due to the varying magnetic flux flow profile the coils are exposed to as the mover traverses along its range of motion. The coils are exposed to a more favorable magnetic flux flow profile at the center stroke position than at any other position in that, for a given input current, the actuator generates more force at the center stroke position than at any other position. The consequences of flux fringing and flux leakage become more pronounced the more off-

center the actuator is located from its zero-stroke position along its motion axis. Given a fixed current input, the actuator force output begins to decrease as soon as the mover moves away from its zero-stroke position, with the actuator experiencing the greatest decrease in force at the ends of the stroke. This force-stroke non-uniformity can be alleviated by adding more coil overhang to the ends of the coils. With additional coil overhang, some of the magnetic flux that was once considered to be leakage flux when the mover was located at the extremes of its motion range becomes fringing flux. Increasing the coil overhang, however, increases the power consumption of the actuator, which, in turn, reduces the MMA's dynamic actuator constant. A balance needs to be struck between the addition of coil overhang to increase force-stroke uniformity and the reduction of coil overhang to increase the dynamic actuator constant of the actuator.

3. Although steel pole pieces can be attached/fastened to the poles of the permanent magnet to help direct flux flow in the desired direction, the pole pieces provide only incremental improvement in terms of reducing the effect of the flux fringing and flux leakage consequences associated with the traditional MMA architecture, not to mention the undesirable additional mass the pole pieces add to the mover [1].

Compared to the other architectures that span the space of direct drive, single phase MMAs, the advantages associated with the traditional MMA architecture generally outweigh its disadvantages. This is reflected in their widespread commercial availability. Section 3.3 of this thesis provides an overview of various non-traditional MMA architectures and their relative advantages and disadvantages when compared to the traditional MMA architecture. The better performance of the traditional MMA architecture is apparent not only via a qualitative analysis of the advantages and disadvantages associated with several non-traditional MMA architectures but also via the performance that has been demonstrated with the traditional MMA architecture in prior work [1][5]. This prior work reports that a traditional MMA architecture with a motion range of around 10 [mm] is capable of having a dynamic actuator constant as large as 20 [$\sqrt{Hz}$]. This finding was based off a survey of commercially available off-the-shelf MMAs of the traditional type with a motion range of around 10 [mm]. The dynamic actuator constants associated with the commercially available off-the-shelf traditional MMAs that were included in the survey are presented in Figure 5.3 in David Hiemstra's MS thesis [5]. Almost of all of the traditional MMAs in the survey had a dynamic actuator constant close to or less than ≈15 [$\sqrt{Hz}$]. Two of the traditional MMAs in the survey had a dynamic actuator constant close to ≈20 [$\sqrt{Hz}$]. The design of an MMA of the traditional type was also presented in [1][5]. The MMA was designed in a systematic matter to maximize its dynamic actuator constant, and a dynamic actuator constant of 14 [$\sqrt{Hz}$] was achieved [1][5]. The apparent upper bound of ≈20 [$\sqrt{Hz}$] on the maximum achievable dynamic actuator constant of the traditional MMA architecture motivated an investigation in this thesis on the maximum achievable dynamic actuator constant of the uncommonly used concentric coil, radial magnet MMA architecture.

3.3 Non-traditional MMA architectures

Section 3.3 of this thesis provides an overview of various non-traditional MMA architectures and their relative advantages and disadvantages when compared to the traditional MMA architecture. For a more detailed treatment of the qualitative discussion of the pros and cons of various non-traditional MMA architectures presented here, please refer to David Hiemstra's MS Thesis [5]. It is noted here that the coil bobbin structure that houses the coil windings is omitted from the schematics of the non-traditional MMA architectures below.

3.3.1 Non-traditional MMA architecture #1

The non-traditional MMA architecture shown in Figure 15 is referred to as non-traditional MMA architecture #1. It features two radially magnetized permanent magnets fixed to a steel core as the mover and a stator that is identical to that of the traditional MMA architecture. The permanent magnets in this architecture induce a magnetic flux loop similar to that of the traditional MMA architecture.

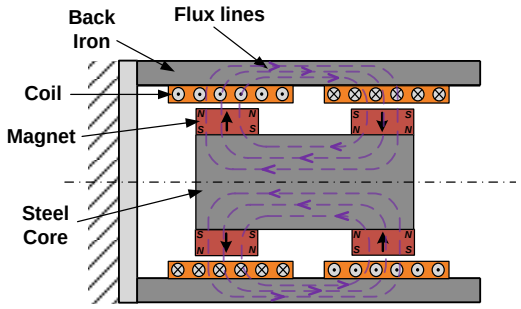

Figure 15: Non-traditional MMA architecture #1 is a radial magnet MMA featuring two radially magnetized permanent magnets of opposite polarity fixed to a steel core. The steel core simultaneously acts as the mover structure and a low reluctance flux path.

Similar to the traditional MMA architecture, the oppositely wound coils negate any adverse effects associated with the armature reaction, the large cross-sectional area of the back iron makes the risk of saturation in the back iron small, and the construction and properties of the back iron make it a good thermal interface for the motion system's thermal management system. One considerable advantage this architecture has over the traditional MMA architecture is the relative spatial orientation between the permanent magnet's direction of magnetization and the direction of current in the coil. The flux from the permanent magnet does not need to make the sharp ninety degree turn associated with the magnetic air gap of the traditional MMA architecture. This characteristic reduces the air gap reluctance of the architecture's magnetic circuit, reducing the flux fringing and flux leakage associated with the larger air gap of the traditional MMA architecture. This characteristic, in turn, suggests a greater actuator force output for a given current input and permanent magnet mass, i.e., a greater dynamic actuator constant than that of the traditional MMA architecture. Another advantage associated with the smaller air gap and lack of flux fringing and flux leakage is that the coils are exposed to a more uniform magnetic flux field as the mover traverses through its range of motion, resulting in a more uniform force-stroke profile than the force-stroke profile of the traditional MMA architecture. Whereas the spatial orientation of the traditional MMA architecture's components result in magnetic flux flow profiles that are increasingly unfavorable as the mover approaches either extreme in its stroke, this architecture's orientation has a magnetic flux flow profile that is relatively constant at every position along the stroke, implying that the magnetic flux flow profile at the extremes of its stroke is nearly as favorable as the magnetic flux flow profile at the center stroke position. This then implies that the actuator does not need much coil overhang to compensate for the small difference in the magnetic flux flow profile at the center stroke position of the MMA and the magnetic flux flow profile at the extremes of the stroke, which, in turn, implies that the actuator has a greater dynamic actuator constant as the mover traverses along its stroke when compared to the traditional MMA architecture. This uniform magnetic flux flow profile characteristic also implies smaller axial reluctance forces between the mover and the back iron than with the traditional MMA architecture. This is implied by the fact that the reluctance of the magnetic circuit of the actuator at the center stroke position is comparable to the reluctance of the magnetic circuit of the actuator at the extremes of the stroke.

The main disadvantage of this architecture is the relatively large mass of the mover. The mass of the steel core component contributes to the mass of the payload, which, as reviewed in Section 2.2.1, severely limits the possibility of a large dynamic mass quantity. The small cross-sectional area of the steel core presents another disadvantage. Risk of saturation in the steel core is moderately high due to the relatively small cross-sectional surface area through which the flux in the steel core travels. Lastly, because the flux density in the air-gap is larger in this architecture, the off-axis forces associated with this architecture would likely be larger than the off-axis forces associated with the traditional MMA architecture.

3.3.2 Non-traditional MMA architecture #2

The non-traditional MMA architecture shown in Figure 16 is referred to as non-traditional MMA architecture #2. It features two radially magnetized permanent magnets coupled by a non-ferrous structure as the mover. The stator is the same as that of the traditional MMA architecture, with the exception of the additional inner back iron component in the center of the architecture. This architecture is similar to the MMA architecture reviewed above except that this architecture's inner back iron structure is part of the stator assembly.

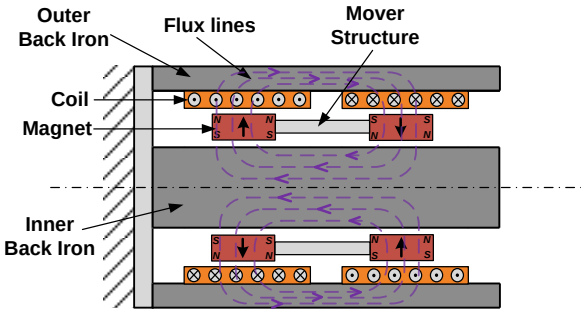

Figure 16: Non-traditional MMA architecture #2 is a radial magnet MMA with two radially magnetized permanent magnets coupled by a non-ferrous mover structure and outer and inner back iron structures that form part of the stator.

This architecture has the same armature reaction, heat transfer, and flux fringing and leakage advantages associated with non-traditional MMA architecture #1. The main advantage of this architecture is the relatively small mass of the mover structure. Unlike the previous architecture, it does not have a steel core that simultaneously serves as the mover structure and the inner back iron. This reduction in the payload mass of the MMA implies that the magnitude of this architecture's dynamic mass quantity has a much higher ceiling.

The main disadvantage of this architecture is the large reluctance force that attracts the permanent magnet mover in the radial direction towards the inner back iron. The small air gap between the permanent magnet and inner back iron causes the magnet to experience relatively large off-axis reluctance forces towards the inner back iron, imposing greater demands on the off-axis stiffness of the actuator bearing. Risk of saturation of the inner back iron is comparable or slightly less than the risk of saturation in the previous architecture. The separation of the inner back iron from the mover implies that the inner back iron has a smaller cross sectional area than the steel core in the previous architecture. Separating the mover from the steel core, however, introduces an air gap between the magnet and the back iron, reducing the magnetic flux density in the circuit which implies a smaller magnetic flux density in the inner back iron of this architecture than the magnetic flux density in the steel core of the previous architecture (non-traditional MMA architecture #1).

3.3.3 Non-traditional MMA architecture #3

The non-traditional MMA architecture shown in Figure 17 is referred to as non-traditional MMA architecture #3. It can be described as an inversed configuration of the traditional MMA architecture [5][28]. Similar to the traditional MMA architecture, it features an axially magnetized permanent magnet as the mover and two sets of oppositely wound coils fixed to the back iron as the stator, but unlike the traditional architecture, the permanent magnet mover is on the outside of the architecture while the stator is on the inside of the architecture.

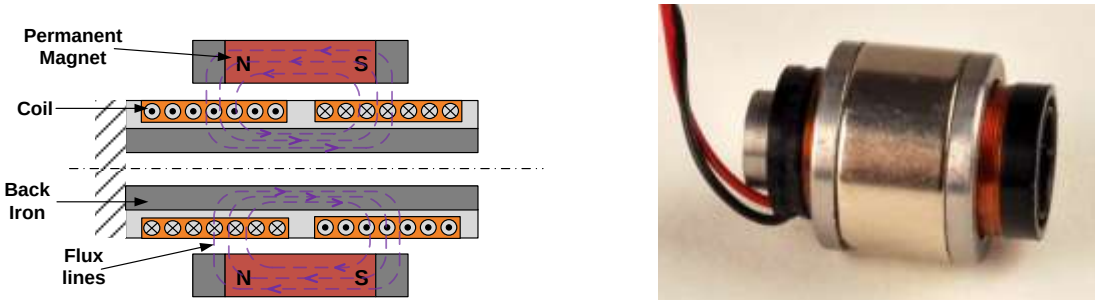

Figure 17: (a) A cross-section of non-traditional MMA architecture #3. It is also described as an inversed configuration of the traditional MMA architecture [5][28]. (b) An off-the-shelf inverted MMA architecture made by H2W technologies [28].

The inverted MMA architecture has the same armature reaction advantage of the traditional MMA architecture. Its coils are wound in opposite directions causing their magnetic flux fields to cancel each other out. The inverted MMA architecture offers the greatest ease of access to the mover when compared to the other non-

traditional MMA architectures discussed in this chapter. Additionally, the open exposure of the coils results in a higher rate of convective heat transfer to the surrounding air than can be obtained with the traditional MMA architecture.

The main disadvantage of this architecture is the small cross-sectional area of the back iron. It makes the back iron prone to saturation. It also restricts the space with which the thermal management system can interface with the actuator. Additionally, the architecture shares the same flux fringing and flux leakage disadvantages associated with the traditional MMA architecture.

3.3.4 Non-traditional MMA architecture #4

The non-traditional MMA architecture shown in Figure 18 is referred to as non-traditional MMA architecture #4. It's often referred to as a "stacked" variation of the traditional MMA architecture [5][29]. The stator comprises three sets of alternately wound coils fixed to the back iron. The mover comprises two axially magnetized permanent magnets joined by a common pole piece. The permanent magnets are magnetized in opposite directions, resulting in a large magnetic flux field density (0.6–0.8 times the magnet material's remanent magnetization value [30]) in the common pole piece region between the two permanent magnets, which in turn implies a relatively large magnetic flux density in the middle coil region.

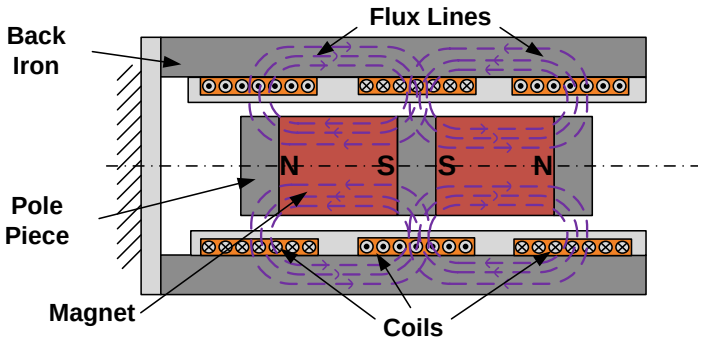

Figure 18: Non-traditional MMA architecture #4. Referred to as the "stacked" variation of the traditional MMA architecture, this architecture is arranged such that the two axially magnetized permanent magnets induce a large magnetic flux density in the middle coil region.

The main advantage of the "stacked" variation of the traditional MMA architecture is the relatively large magnetic flux density that can be achieved in the middle coil region. A higher magnetic flux density in the middle coil region implies that, as long as the back iron does not saturate, the "stacked" variation of the traditional MMA architecture has a larger force output per current input than the traditional MMA architecture. The spatial orientation of the permanent magnets also reduces the degree to which flux fringes in the middle coil region, implying a more uniform force-stroke profile input than the traditional MMA architecture.

The main disadvantages of the "stacked" variation of the traditional MMA architecture are the additional mass of the second permanent magnet and the high risk of saturation in the middle pole piece and middle back iron region. Taken together, these two characteristics tend to reduce the dynamic actuator constant of the MMA, negating the advantage of the large magnetic flux density in the middle region of the MMA. When compared to the traditional MMA architecture, the additional mass of the second permanent magnet also reduces the upper bound of the MMA's maximum dynamic mass quantity (see Section 2.3). The "stacked" variation also suffers from flux fringing and flux leakage at the two ends of the MMA. Lastly, the architecture can have greater off-axis reluctance forces than the traditional MMA architecture due the addition of the second magnet, imposing greater demands on the bearing. If the bearing used only supports the mover at one end, the longer axial length of the mover, together with the greater off-axis loads, requires that the bearing withstand a larger cantilever moment than the cantilever moment required to support the mover of the traditional MMA architecture. If the off-axis cantilever moment is too great for a bearing that only supports the mover at one end, a different bearing design that supports the mover at both ends might be necessary.

3.3.5 Non-traditional MMA architecture #5

The non-traditional MMA architecture shown in Figure 19 is referred to as non-traditional MMA architecture #5 in this thesis. It is commonly referred to as the slotted coil MMA architecture due to the slots in the back iron in which the coils are located. This non-traditional architecture differs from the other architectures presented in this chapter in that the coils that are slotted in the back iron do not directly interact with the permanent magnet's flux field to produce force via the Lorentz force. It instead works like a solenoid; a coil induced magnetic flux loop forms in the iron slot around the recessed coil, causing the radially magnetized permanent magnet to experience an axial reluctance force that aligns itself with the magnetic flux loop [5]. The slotting of the coils in the back iron decreases the net reluctance of the magnetic circuit, which, in turn, increases the magnetic flux in the circuit.

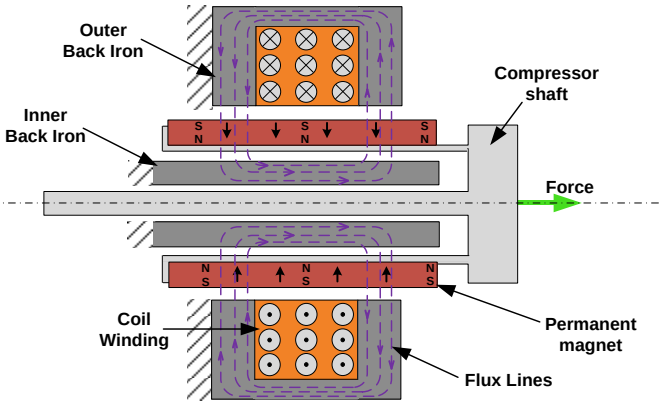

Figure 19: Non-traditional MMA architecture #4. The "slotted coil" MMA architecture.

The slotted MMA architecture is commonly used in compressor type applications [31][32]. Compressor type applications typically demand that the actuator carry out a reciprocating motion at a fixed frequency. In these reciprocal applications, the architecture is sized so that the resonant frequency of the motion system matches the desired operating frequency of the application [5][33]. The slotted MMA architecture draws most of its advantages from its relatively large volumetric force output [5][34]. It enables the slotted coil MMA to operate at higher accelerations, speeds, and bearing load capacities than non-slotted MMA architectures [5]. Despite these advantages, the slotted MMA architecture is not suitable for fine motion control due to its highly non-uniform force-stroke profile; a characteristic typical of linear actuators that operate via the reluctance force [5][35]. There are additional limitations of this architecture design that pertain to higher inductance, magnetic hysteresis, and eddy current losses as described in [5].

CHAPTER 4

4 An upper limit to the dynamic actuator constant

In seeking to design an MMA with as large a dynamic actuator constant as possible, an investigation was undertaken to find out if the maximum achievable dynamic actuator constant of an MMA has some inherent upper bound that cannot be overcome regardless of an MMA's architecture or geometry; an upper bound that stems from the fundamental physical phenomena that governs the generation of force in all MMAs. A better understanding of the physical phenomena that limit the maximum achievable dynamic actuator constant of an MMA can provide insight as to how and to what extent different design decisions affect the magnitude of the dynamic actuator constant. More specifically, it could provide insight on the extent to which the limitations to the maximum attainable dynamic actuator constant are due to the physical architecture of the MMA, the physical phenomena (and physical properties) inherent to the operation of MMAs in general (non-ideal materials, reluctance forces, armature reaction, inductance, etc.), and the mechanical design constraints imposed by existing manufacturing and fabrication methods. As detailed below, analysis of an idealized model representative of the force producing physics of an MMA, i.e., an idealized model of the force producing interaction between a permanent magnet element and a current carrying conductor element, shows that there is indeed an upper bound to the maximum achievable dynamic actuator constant of an MMA, inherent to all MMAs regardless of architecture.

Figure 20 shows a schematic of the idealized model representative of the force producing physics of an MMA, including a permanent magnet element and a current carrying conductor element, each with identically infinitesimally small length and width dimensions, *dl* and *dw*, respectively, and finite thickness dimensions t_m and t_c, where t_m is the thickness of the permanent magnet element, and t_c is the thickness of the current carrying conductor element. Flux travels out from the north pole of the permanent magnet element in a direction perpendicular to the direction of current (shown to be into the page) in the current carrying conductor element and then travels back around to the south pole of the permanent magnet element along an ideal, zero-reluctance flux return path. Superimposed on the schematic in the color green is the representative magnetic circuit of the idealized model.

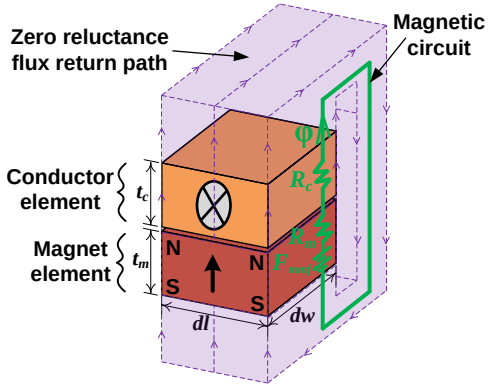

Figure 20: An idealized model of the force producing physics of an MMA. Its associated magnetic circuit representation, shown in the color green, is superimposed on the idealized model. The arrows on the dotted purple lines indicate the direction of flux flow. Any flux flow path outside of the one shown in the magnetic circuit is modeled as having an infinite reluctance, ensuring zero flux fringing and zero flux leakage.

The following assumptions are made in the analysis of the ideal MMA physics model:

1. No flux fringing (i.e. everything outside of the magnetic circuit acts as a perfect magnetic flux insulator). This assumption ensures that all the flux from the permanent magnet element goes through the current carrying conductor element in a direction perpendicular to the current direction.
2. A zero reluctance flux return path (i.e. perfect magnetic flux conductor). This assumption removes the possibility of the flux return path material reducing the flux through the magnetic circuit.
3. The permeability of the permanent magnet and conductor elements is approximately equal to the permeability of a vacuum. The assumption is valid because the permeability of the most common permanent magnet and conductor materials is very close to that of vacuum.

4. The air gap between the permanent magnet and conductor elements is infinitesimally small. This ensures that the only reluctances that affect system dynamics are that of the permanent magnet and current carrying conductor elements.
5. The entire region occupied by the current carrying conductor is filled with current carrying conductor. It is absent of the small gaps of air that are unavoidably introduced when a coil is packed into a volume of space.

Based on standard lumped parameter magnetostatic analysis [36], the magnetomotive force (F_{mmf}) and the lumped reluctances of the permanent magnet element (R_m) and the current carrying conductor element (R_c) can be expressed as,

$$F_{mmf} = \frac{B_r t_m}{\mu_m} \; ; \quad R_m = \frac{t_m}{\mu_m \, dw \, dl} \; ; \quad R_c = \frac{t_c}{\mu_c \, dw \, dl} \, , \tag{63}$$

where B_r is the remanent flux density of the permanent magnet, and μ_m and μ_c are the permeabilities of the permanent magnet and the coil, respectively. Equation (63) implies that the resultant flux (φ) and the average magnetic flux density in the conductor element (B_c) can be expressed as,

$$\phi = \frac{F_{mmf}}{R_m + 2R_g} \; ; \quad B_c = \frac{\phi}{dw \, dl} \, . \tag{64}$$

Given the above, the force output (F), power consumed, i.e., power dissipated as heat (P), and the mass of the permanent magnet (m_m) can be determined to be

$$\begin{aligned} F &= B_c \, i \, dl = \frac{\phi}{dw} i \\ P &= i^2 R = i^2 \rho_c \frac{dw}{t_c \, dl} \\ m_m &= \rho_m V_m = \rho_m \, t_m \, dw \, dl \end{aligned} \quad , \tag{65}$$

where i is the coil current, R is the coil wire resistance, ρ_c is the coil wire resistivity, ρ_m is the permanent magnet mass density, and V_m is the volume of the permanent magnet element. The closed form expression of the dynamic actuator constant for the idealized MMA physics model can then be expressed as,

$$\beta_{idealized} = \frac{F}{\sqrt{P}\sqrt{m_m}} = \frac{B_r}{\sqrt{\rho_c \rho_m}} \frac{\sqrt{t_c t_m}}{\left(t_c + t_m\right)} \, . \tag{66}$$

Taking the derivative of Equation (66) with respect to either t_c or t_m and setting the derivative equal to zero,

$$\begin{aligned} \frac{d}{dt_c} \beta_{ideal} &= \frac{B_r}{2\sqrt{\rho_c \rho_m}} \sqrt{\frac{t_m}{t_c}} \frac{\left(t_m - t_c\right)}{\left(t_c + t_m\right)^2} = 0 \\ \frac{d}{dt_m} \beta_{ideal} &= \frac{B_r}{2\sqrt{\rho_c \rho_m}} \sqrt{\frac{t_c}{t_m}} \frac{\left(t_c - t_m\right)}{\left(t_c + t_m\right)^2} = 0 \end{aligned} \quad , \tag{67}$$

it is evident that the maximum of Equation (66) occurs when the thickness of the conductor element, t_c, equals the thickness of the permanent magnet element, t_m. Substituting t_c with t_m (or vice-versa) in Equation (66), the maximum achievable dynamic actuator constant for the idealized MMA physics model was found to be,

$$\beta_{\text{idealized,max}} = \frac{B_r}{2\sqrt{\rho_c \rho_m}} \, , \tag{68}$$

showing that there is indeed an inherent upper bound to the maximum achievable dynamic actuator constant of an MMA (and all electromagnetic Lorentz force actuators in general).

The result implies the following:

1. There is indeed a maximum achievable dynamic actuator constant that is inherent to all MMAs, regardless of the architecture. For an ideal MMA interaction between a permanent magnet element of N52-grade neodymium ($B_r \approx 1.42$ [T], $\rho_m = 7600$ $\left[\frac{kg}{m^3}\right]$) and a conductor element of copper ($\rho_c = 1.68 \cdot 10^{(-8)}$ [Ω-m]), the magnitude of the maximum achievable dynamic actuator constant 62.8 [$\sqrt{Hz}$].
2. The limiting factors that impose an upper bound on the maximum achievable dynamic actuator constant are the material properties of the actuator components (i.e., not the geometry of the actuator components). The maximum achievable dynamic actuator constant (Equation (72)) is solely a function of the remanent flux density of the permanent magnet, B_r, the mass density of the permanent magnet, ρ_m, and the resistivity of the conductor, ρ_c. Deviations from the geometry of the idealized model are to be expected in a practically realizable MMA geometry, implying that the dynamic actuator constant of a practically realizable MMA geometry will always be less than the maximum dynamic actuator constant of the idealized MMA design.
3. To maximize the dynamic actuator constant of an MMA, one should choose a permanent magnet with a large remanent magnetization, B_r, and low mass density, ρ_m, such as N52-grade neodymium permanent magnets, and a current carrying conductor with a low resistivity, ρ_c, such as copper.
4. In an ideal model of the force producing interaction between a permanent magnet element and a current carrying conductor element, the maximum achievable dynamic actuator constant occurs when the thickness of the conductor, t_c, equals the thickness of the magnet, t_m. This may have some physical significance but is not obvious at this point.
5. For a given ideal MMA interaction between a permanent magnet element and current carrying conductor element, the dynamic actuator constant is independent of the infinitesimally small length and width dimensions of the elements. Analysis of an idealized MMA interaction between permanent magnet and current carrying conductor elements that have finite lengths and widths shows that the dynamic actuator constant is independent of the finite length and width dimensions as long as the lengths and widths of the two elements are equal. This makes intuitive sense as having one element be longer or wider than the other implies that some portion of one of the elements is not being used to generate force. When the elements have equal length and width dimensions, the entirety of each element is used to generate force.
6. The result provides insight into the extent to which the upper bound to the maximum dynamic actuator constant of the traditional MMA architecture is due to performance limitations inherent to all MMAs versus performance limitations specific to the traditional MMA architecture. Given that N52-grade neodymium permanent magnets and copper coils were selected as materials for the traditional MMA architecture designed to maximize its dynamic actuator constant in journal paper [1] and that the maximum dynamic actuator constant that was able to be achieved was 14 [$\sqrt{Hz}$], the gap between the maximum dynamic actuator constants of the idealized MMA and the traditional architecture must be attributed to other factors besides the inherent performance limitations common to all MMAs. These factors include the traditional MMA architecture's non-zero stroke, non-zero mechanical air gap, flux fringing and flux leakage, axial reluctance force attraction to the center stroke position, as well as any other factors that have yet to be identified.
7. The MMA architectures whose physics most closely resembles that of the ideal MMA are the MMA architectures most likely to have a large dynamic actuator constant. This implies that high performance MMA architectures are likely to have the magnetic flux from the permanent magnet travel in a direction perfectly perpendicular to the coil current direction (minimizing flux fringing/leakage). It also implies that high performance MMA architectures are likely to have small mechanical air gaps and low reluctance back iron components that do not saturate (minimizing the reluctance of the flux return path).
8. The upper bound to the maximum achievable dynamic actuator constant of an MMA is a useful reference metric as it can provide context when gauging the relative significance of advances in MMA performance, e.g., an increase in the dynamic actuator constant of an MMA from 15 [$\sqrt{Hz}$] to 30 [$\sqrt{Hz}$] is more significant if the upper bound to the maximum achievable dynamic actuator constant is 60 [$\sqrt{Hz}$] than if the upper bound to the maximum achievable dynamic actuator constant is 600 [$\sqrt{Hz}$].

CHAPTER 5

5 Identifying the variation of the concentric coil, radial magnet MMA architecture that is most likely to yield high performance

The concentric coil, radial magnet MMA architecture shown in Figure 2 is shown again in Figure 21 for convenience. The architecture is one of the many variations of the concentric coil, radial magnet MMA architecture that was initially reported in patent [17] and master's thesis [5]. All variations of the concentric coil, radial magnet MMA comprise at least one ring-shaped, radially magnetized permanent magnet, a corresponding set of concentric coils in between which the permanent magnet travels, and a back iron structure that directs flux flow. A systematic evaluation of several variations of the architecture led to the conclusion that the concentric coil, radial magnet MMA architecture shown in Figure 21 had the greatest potential for high performance. This chapter presents the evaluation process that led to this conclusion. It is organized as follows. Section 5.1 presents the set of MMA design considerations that inform the evaluation criteria used to compare different variations of the concentric coil, radial magnet MMA architecture. Section 5.2 presents the evaluation process used to identify the particular variation of the concentric coil, radial magnet MMA architecture shown in Figure 21 as the architecture with the highest potential performance.

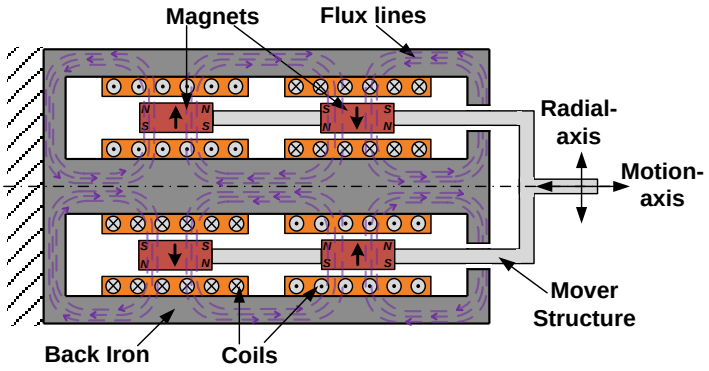

Figure 21: A cross-section of the concentric coil, radial magnet MMA architecture.

5.1 Design considerations for high performance MMAs

In MMA design, magnetic circuit analysis is often employed to model the physics and predict the performance of a given MMA architecture. The results that follow from magnetic circuit analysis, however, are not always valid. This is because the standard assumptions taken during magnetic circuit analysis do not always hold. The MMA designer must carefully examine said architecture to identify the conditions under which the magnetic circuit analysis results hold. The electromagnetic phenomena listed in Section 3.1 are often the culprits that invalidate the magnetic circuit analysis assumptions. Even when the magnetic circuit analysis assumptions hold, however, the results that follow from magnetic circuit analysis are not always the best predictor of actuator performance. Other design issues need to be taken into consideration in order to form a good judgement of an MMA architecture's merit as a high performance actuator.

Listed below are several important MMA design considerations to keep in mind while seeking to maximize the performance of an MMA architecture. Derived from an understanding of MMA-driven motion system dynamics and electromechanical design, these design considerations serve as a framework of knowledge and guiding design principles that can be used throughout the entire MMA design process, from the initial assessment stage used to screen MMA architectures for certain characteristics or a level of potential performance, all the way through the detailed mechanical design stage of the design process. Many of the design considerations listed below are informed by the electromagnetic phenomena presented in Section 3.1, and while there is some overlap with the content presented in that section, the design considerations listed below place a greater emphasis on the design implications of said electromagnetic phenomena when aiming to design an MMA for high performance. It is noted here that a more thorough and expansive review of these design considerations can be found in David Hiemstra's master's thesis [5].

1. The magnetic flux path reluctances of an MMA architecture should be minimized, implying that magnetic air gap lengths be minimized and that saturation of the back iron be avoided. Minimizing the magnetic air gap lengths and avoiding saturation of the back iron maximizes the magnetic flux densities in the magnetic air gaps where the coil windings are located which in turn maximizes the output force that an MMA architecture is capable of.
2. Minimizing the air gap and maximizing the gap flux densities, however, leads to increased off-axis, attractive reluctance forces between the permanent magnet and the back iron, requiring that the motion bearing's off-axis stiffness be sufficient to withstand these off-axis forces.
3. The armature reaction (i.e. the influence of the coil flux on the flux flow profile the permanent magnet would induce in the absence of the coil) of an MMA can induce a reluctance force that causes the actuator force output to vary with position for a given input current. The armature reaction can also cause saturation of the back iron, resulting in a non-linear force-current relationship between the force output and current input. Therefore, the armature reaction of an MMA design should be minimized.
4. The MMA architecture should minimize heat generation and storage, and facilitate expedient heat removal from the coil windings, away from the stage and sensors. System temperature should remain stable during operation.
5. The MMA architecture should allow for practically feasible construction and assembly, including reasonable tolerances, reasonably accessible materials, and mounting locations that ease assembly. High volume manufacturing constraints should also be considered.
6. The sum of the MMA architecture's permanent magnet mass and payload mass should be small in order to make the MMA's dynamic mass quantity large.

5.2 Identifying the best variation of the concentric coil, radial magnet MMA architecture

In investigating the space of single-axis, single-phase MMA architectures, it stands to reason that the MMA architectures with the highest potential for a large dynamic actuator constant are those whose topology most closely resembles that of the ideal MMA physics model shown in Figure 20 in Chapter 4. One such group of architectures is the set of the concentric coil, radial magnet MMA architecture variations reported in patent [17] and master's thesis [5]. As mentioned before, all of the concentric coil, radial magnet MMA architecture variations reported in patent [17] and master's thesis [5] share a similar arrangement of the coil winding, permanent magnet, and back iron components that make up an MMA. This arrangement, shown in Figure 22, is referred to as the concentric coil, radial magnet MMA "building block". It consists of a cylindrical, radially magnetized ring magnet sandwiched between a set of concentric coil windings, along with an inner and outer back iron to facilitate a desired flux flow profile. Similar to the idealized MMA physics model, the direction of the permanent magnet's magnetization is such that the direction of flux flow emanating from and returning to the permanent magnet's north and south poles, respectively, is perpendicular to the direction of current in the coil windings, alleviating the need to reduce flux fringing via the addition of a pole piece like in the traditional MMA architecture. Another similarity is the negligible reluctance of the concentric coil, radial magnet MMA building block's back iron (as long as the back iron doesn't saturate) and the zero-reluctance return path of the idealized MMA physics model. The concentric coil, radial magnet MMA building block deviates from the ideal MMA physics model in that the lengthwise span of the coil winding is larger than the lengthwise span of the permanent magnet. This characteristic is necessary for the MMA to have a non-trivial motion range. It also deviates from the ideal MMA physics model in that the building block has a non-zero mechanical air gap thickness between the coil and the permanent magnet. The smallest mechanical air gap thickness that can be achieved is dictated by the limitations of current fabrication and assembly processes. Another deviation from the ideal MMA physics model that isn't shown in Figure 22 is the presence of the coil bobbin component that houses the set of coil windings. The coil bobbin's radial thickness increases the overall magnetic air gap thickness of the building block. Lastly, the MMA building block's coil windings are not wound with 100% efficiency in the volume of space they occupy – a small fraction of the space is taken up by air and wire coating. This inefficiency as well as the other deviations from the idealized model noted above need to be accounted for when designing an MMA.

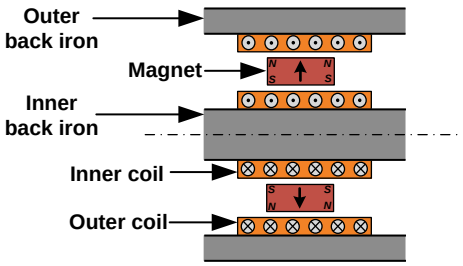

Figure 22: A cross section of a concentric coil, radial magnet MMA building block. The building block comprises a cylindrical, radially magnetized permanent ring magnet sandwiched between a set of concentric coil windings, along with an inner and outer back iron to direct flux flow and minimize the reluctance of the magnetic circuit.

Before presenting several of the concentric coil, radial magnet MMA architecture variations, it is noted here that the planar analog to the concentric coil, radial magnet MMA architecture was also considered during the investigation of high performance MMA architectures but was deemed inferior to the cylindrical analog. It was posited that the cylindrical design has greater potential for a large dynamic actuator constant because, in the cylindrical design, no strand of wire in the concentric coil windings goes unexposed to the permanent magnet's flux field as the permanent magnet traverses through its full range of motion. The planar design, on the other hand, necessitates that sections of the planar coil windings go unexposed to the permanent magnet's flux field as the permanent magnet traverses through its full range of motion. This difference in design implies that that the cylindrical design is more likely to have a larger upper bound to its maximum achievable dynamic actuator constant than the planar design due to the fact that all of the concentric coil winding in the cylindrical design contributes to produce axial force as the permanent magnet traverses through its full range of motion, whereas certain sections of the planar coil winding do not contribute to produce axial force at any point along the permanent magnet's range of motion.

The concentric coil, radial magnet MMA building block can be arranged into different variations of the concentric coil, radial magnet MMA architecture via a variety of different back iron designs (i.e. low reluctance flux flow paths). By using connecting back iron additions, multiple building blocks can be joined together in parallel, in series, or in combinations thereof to produce different back iron designs that facilitate a desired axial-force-inducing flux flow profile within the MMA architecture. Table 1 shows cross-sections of the five concentric coil, radial magnet MMA architecture variations that were selected to be evaluated for their potential for high performance. Using the systematic evaluation process presented below, the architecture variation in Figure 21 (i.e. variation 4 in Table 1) was ultimately selected as the architecture variation with the greatest potential for high performance. In the interest of keeping mechanical complexity low, designs in which multiple building blocks are joined together in parallel or designs in which more than two building blocks are joined in series were omitted from the pool of MMA designs under consideration for inclusion in the evaluation process. That then left designs based on a single building block or two building blocks in series as potential options. During the initial evaluation phase of the MMAs in this space of designs, it became obvious that certain architectures had clear disadvantages that would prevent them from achieving the same level of performance as one or more of the other architectures in the space. These architectures were not included in the evaluation process. The architectures that remained after this initial screening process are the five architecture variations in Table 1.

	Variations of the concentric coil, radial magnet MMA architecture
1	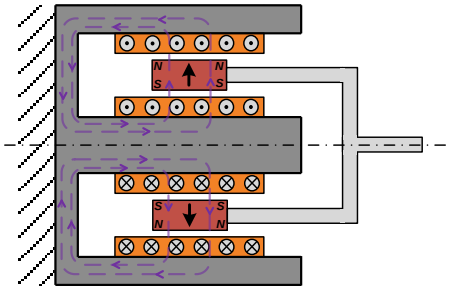
2	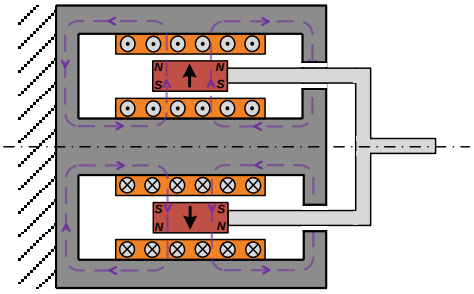
3	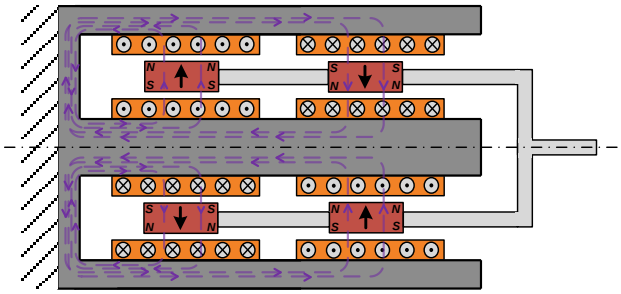
4	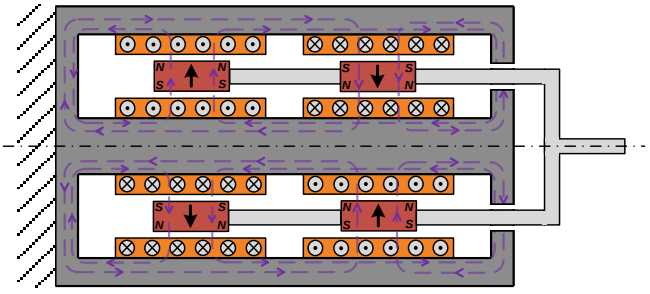
5	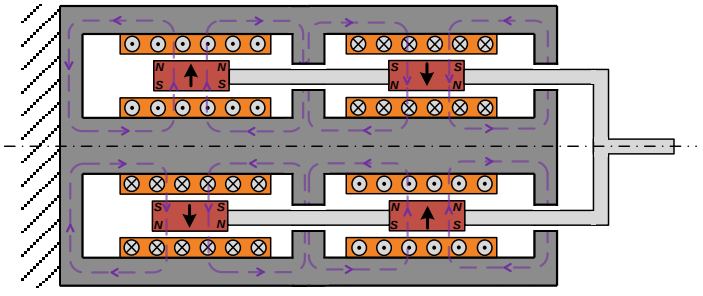

Table 1: The five concentric coil, radial magnet MMA architecture variations that were evaluated for their potential for high performance.

Following the selection of the five architectures in Table 1, a more thorough evaluation process was used to assess and compare each design's potential for high performance. The results of this more thorough evaluation process are summarized in Table 2. The evaluation process consisted of analyzing each to assess its relative strengths and weaknesses in the following four categories that were selected to serve as the evaluation criteria:

1. **Force-stroke uniformity**: Each design was classified as having low, medium, or high force-stroke uniformity. The effects of any flux fringing or flux leakage that might be present in the system were taken into consideration when assessing the force-stroke uniformity of each design. The effect of any induced reluctance forces present in the system had to be estimated when assessing the force-stroke uniformity of each design. To gain a rough estimate of any reluctance forces that might be present in the system, schematics of the expected flux flow profile in each design were developed and examined, as is illustrated in the first and second column of Table 2. Developing sufficiently accurate schematics of the flux flow profile of each design requires that one take into account the potential presence and effect of the design's armature reaction which in MMAs is equivalent to the effect that the magnetic flux induced by the coil windings has on the magnetic flux flow profile induced by the permanent magnet(s) of the system. To accomplish this, the expected magnetic flux flow induced by each source of magnetic flux in the system was superimposed onto a single schematic of the cross-section of each design, as is shown in first column of Table 2. The magnetic flux flow from each source of magnetic flux is represented as a dotted line with arrows pointing in the direction of flux flow. The thickness of the dotted line is set to represent the magnitude of the magnetic flux density of the associated flux flow. Simple vector addition or subtraction was then used to develop a schematic of the expected magnetic flux flow profile induced by the bodies in the system, as is shown in the second column of Table 2. In making these schematics, it was assumed that the magnitudes of the magnetic flux densities induced by the permanent magnet and the coil windings were of the same order of magnitude. The expected magnetic flux flow profiles shown in the second column of Table 2 were confirmed to be sufficiently accurate for the purposes of this evaluation process via the FEA simulation results shown in Table 3.
2. **Risk of saturation**: Each design was classified as having a low, medium, or high risk of saturation. The schematic of the expected flux flow profile of each design in combination with knowledge of each design's geometry was used to determine each design's risk of saturation.
3. **Mechanical complexity**: The mechanical complexity of each design was classified as low, medium, or high. Ease of fabrication and assembly were the primary factors taken under consideration when evaluating the mechanical complexity of each design.
4. **Thermal management accessibility**: Designs that provide low thermal resistance paths between the thermal management system and the coil windings and high thermal resistance paths between the actuator and the motion stage are classified as having low thermal management accessibility. Design 1 in the chart sets the bar. It is classified as having high thermal management accessibility due to the actuator having an open end on the side of the actuator that interfaces with the motion stage, as well as the ease of access to the back iron structure that supports the coil windings.

As is noted above in the descriptions of the four categories, a three tier rating system was used to rate each design in each the four categories. For each category, each design was given a positive, neutral, or negative rating. The third column of Table 2 shows the ratings the designs were given. The background color associated with each of the ratings reflects whether the rating is positive, neutral, or negative, with positive ratings having a green background, neutral ratings having an orange background, and negative ratings having a red background.

After weighing the relative strengths and weaknesses associated with each design, design 4 was selected as the design to move forward with in the design process. Despite the fact that designs 1 and 2 have a greater number of positive ratings, design 4 was determined to have the highest potential performance because the weaknesses associated with designs 1 and 2 are much more difficult to address than the weakness associated with design 4. Design 4 was rated as having a higher degree of mechanical design complexity, owing to its closed architecture. However, these practical design and fabrication challenges can be overcome, as is evident in the pictures of the constructed concentric coil, radial magnet MMA shown later in Chapter 7.

	Magnet and Coil Winding Flux Paths	Expected Flux Flow	Pros/Cons
1	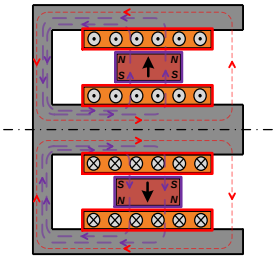	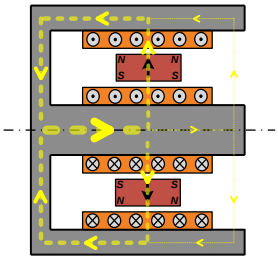	Low force-stroke uniformity High risk of saturation Low mechanical complexity High thermal mgmt accessibility
2	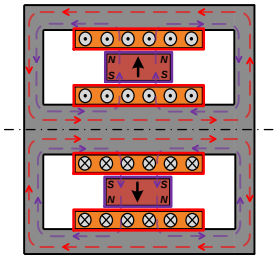	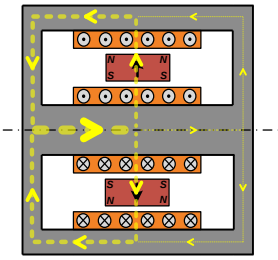	High force-stroke uniformity High risk of saturation Medium mechanical complexity High thermal mgmt accessibility
3	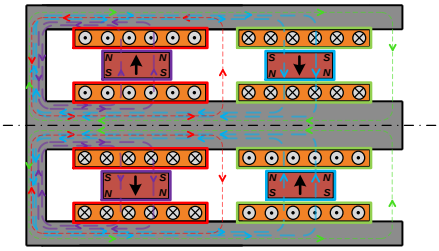	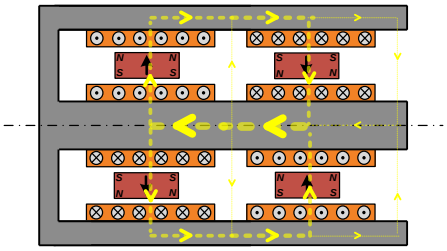	Medium force-stroke uniformity High risk of saturation Medium mechanical complexity Medium thermal mgmt accessibility
4	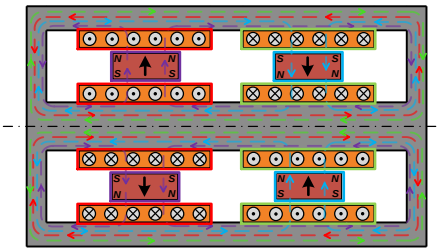	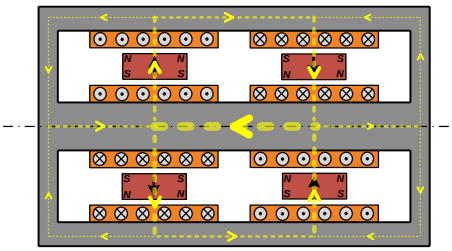	High force-stroke uniformity Medium risk of saturation High mechanical complexity Medium thermal mgmt accessibility
5	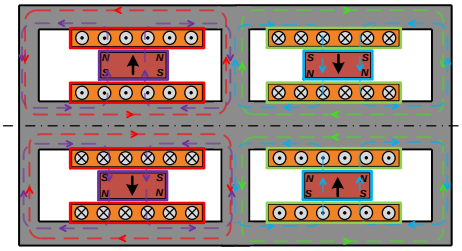	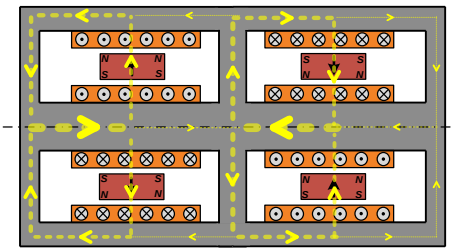	High force-stroke uniformity High risk of saturation High mechanical complexity Medium thermal mgmt accessibility

Table 2: Summary of the strengths and weaknesses associated with the different variations of the concentric coil, radial magnet MMA architecture. Characteristics that are considered strengths have a fill color of green. Characteristics that are considered weaknesses have a fill color of red. Characteristics that are considered neutral – neither a strength nor a weakness – have a fill color of orange.

(1)	Expected Flux Flow	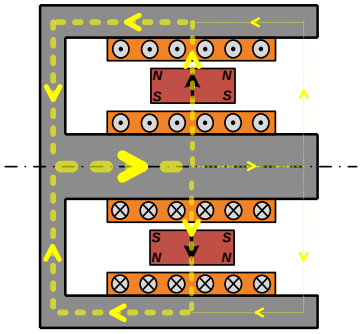
	FEA Simulation Flux Field	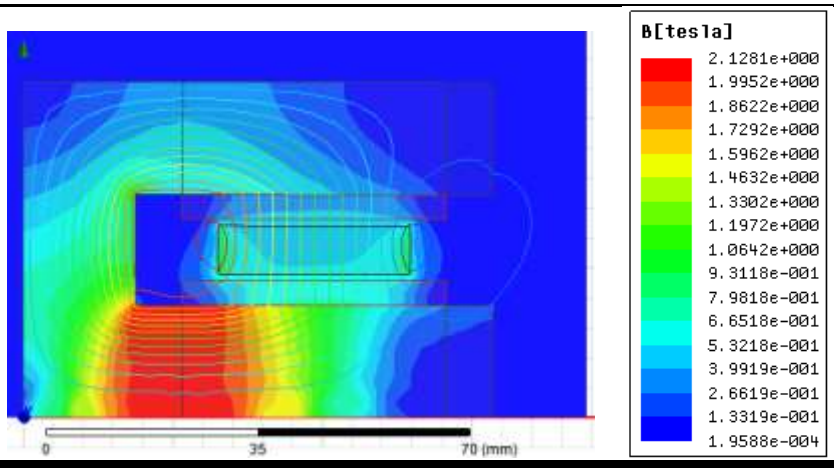
(2)	Expected Flux Flow	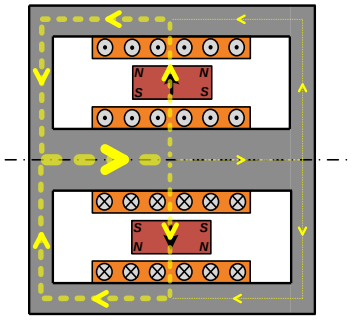
	FEA Simulation Flux Field	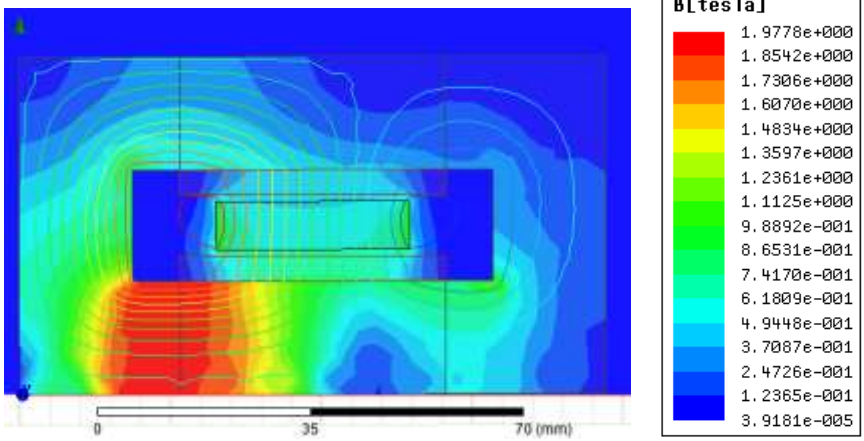

(3)	Expected Flux Flow	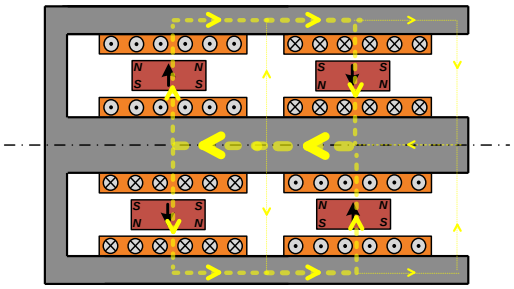
	FEA Simulation Flux Field	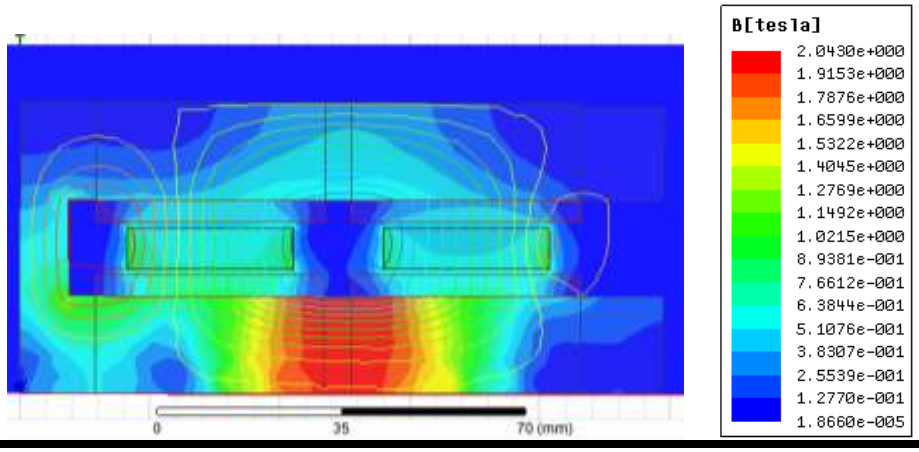
(4)	Expected Flux Flow	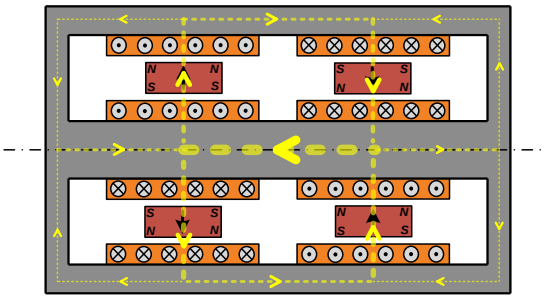
	FEA Simulation Flux Field	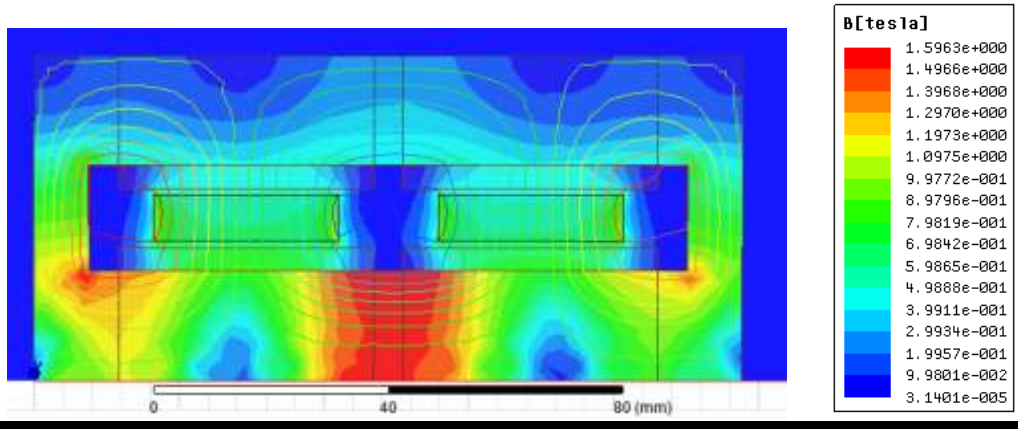

(5)	Expected Flux Flow	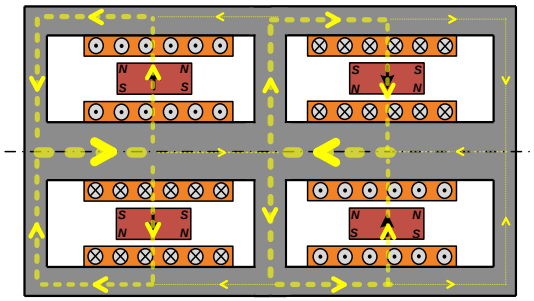
	FEA Simulation Flux Field	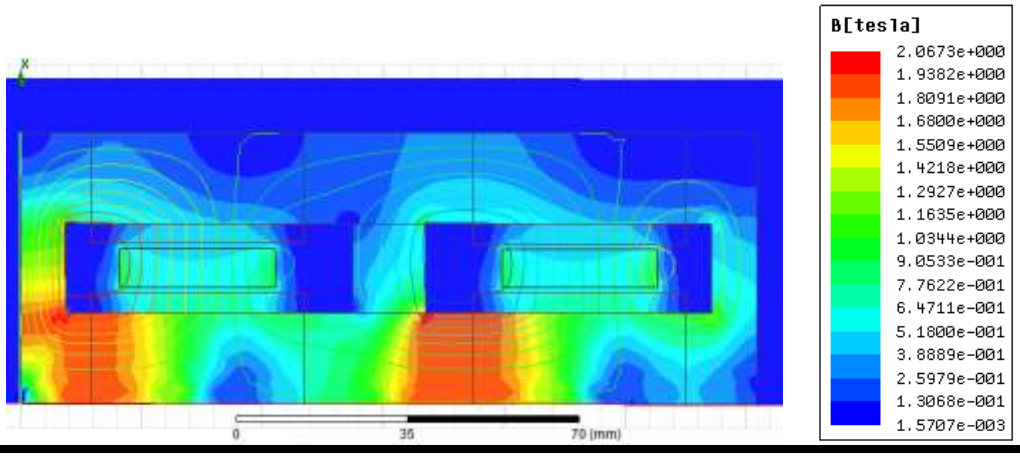

Table 3: The magnetic flux density fields of the five candidate concentric coil, radial magnet MMA architecture variations as predicted by FEA simulations, as well as the magnetic flux flow profiles of the five candidate concentric coil, radial magnet MMA architecture variations as predicted by the simple vector addition method. In generating the FEA simulation flux flow profiles for each variation of the concentric coil, radial magnet MMA, N52-grade neodymium permanent magnets and copper coils were used as the materials. In addition, all of the architecture variations shared the following concentric coil, radial magnet MMA parameter values (see Figure 23(a)) to generate the FEA simulation flux flow profiles: magnet outer radius, r_{mo}=32 [mm]; magnet length, l_m=32 [mm]; magnet thickness, t_m=8 [mm]; coil thickness, t_c=4 [mm]; mechanical air gap thickness, t_{gmech}=1.1 [mm]; stroke length, l_{stroke}=10 [mm]; $l_{overhang}$=1 [mm], current, i=0.25 [A].

CHAPTER 6

6 The optimization of the concentric coil, radial magnet MMA architecture

Having identified the concentric coil, radial magnet MMA architecture (variation 4 in Table 1) as an MMA architecture with a potentially higher performance ceiling than the architectures of the current state-of-the art in commercial MMAs, the next course of action was to design a concentric coil, radial magnet MMA that realizes this potentially higher performance. This chapter is dedicated to the optimization process that was developed and used to optimize the design of a concentric coil, radial magnet MMA that satisfies the actuator level design specifications in Table 4.

Actuator Level Design Specification	Target Value	Achieved Value
Stroke length, l_s	10 [mm]	10 [mm]
Payload mass, m_p	0.7 [kg]	0.7 [kg]
Size/Footprint	Desktop Size (< 150 [mm] x 150 [mm])	150 [mm] x 100 [mm]
Force-stroke non-uniformity	< 5%	3%
Cont. Force, F	> 40 [N]	51 [N]
Cont. Power, P	Minimize	5 [W]
Performance Metric, $PM=\beta*M_{dynamic}$	Maximize	15.4 $[\sqrt{Hz}\cdot\frac{1}{\sqrt{kg}}]$
Dynamic actuator constant, β	The value that maximizes PM	25.5 $[\sqrt{Hz}]$
Dynamic mass quantity, $M_{dynamic}$	The value that maximizes PM	0.60 $[\frac{1}{\sqrt{kg}}]$

Table 4: The actuator level design specifications that the constructed concentric coil, radial magnet MMA was designed to satisfy and the corresponding specifications that were achieved.

The design of a concentric coil, radial magnet MMA was approached as an optimization problem in which, given a design space spanned by concentric coil, radial magnet MMA designs, the design that has the highest performance is sought, with the magnitude of the product of the MMA's dynamic actuator constant and dynamic mass quantity, i.e., the performance metric, serving as the measure of performance. A systematic optimization process was developed that generates a graphical heat map representation of the MMA design space, mapping the MMA designs in the design space to the cells of a cell array, with each cell assigned a fill color representative of the associated design's performance (allowing for the optimal design to be identified via visual inspection of the heat map). Detailed in full below, the optimization process can be described as a brute-force search optimization process. It begins with the derivation of a closed form expression of the performance metric (the magnitude of the product of the MMA's dynamic actuator constant and dynamic mass quantity) as a function of the geometric and material property parameters that define a concentric coil, radial magnet MMA design. The closed form expression is then used to calculate an approximate performance metric value for every MMA design in the design space – the set of data from which the heat map representation of the design space is generated. Finally, after using the closed form approximation of the performance metric to identify the region of the design space in which the optimal MMA design is located, FEA simulations are used to hone in on the optimal design's location in the design space, the coordinates of which correspond to the set of geometric and material property parameters that define the optimal design.

6.1 Deriving a closed form approximation of the CCRM MMA's performance metric

The performance metric of the concentric coil, radial magnet MMA architecture, PM_{CCRM}, is defined as,

$$PM_{CCRM} = \beta_{CCRM} \cdot M_{dynamicCCRM} , \tag{69}$$

where β_{CCRM} and $M_{dynamicCCRM}$ are the architecture's dynamic actuator constant and dynamic mass quantity, respectively. The architecture's dynamic actuator quantity, β_{CCRM}, is defined as,

$$\beta_{CCRM} = \frac{F_{CCRM}}{\sqrt{P_{CCRM}}\sqrt{m_{mCCRM}}} \tag{70}$$

where F_{CCRM} is the actuator output force, P_{CCRM} is the actuator coil power dissipation, and m_{mCCRM} is the permanent magnet mass of the actuator. The architecture's dynamic mass quantity, $M_{dynamicCCRM}$, is defined as

$$M_{dynamicCCRM} = \frac{\sqrt{m_{mCCRM}}}{m_{mCCRM} + m_{pCCRM}}, \tag{71}$$

where m_{pCCRM} is the payload mass of the actuator. To derive a closed form expression of the performance metric in terms of the geometric parameters that define the concentric coil, radial magnet MMA geometry, the architecture was modeled as a lumped parameter system as is shown in Figure 23.

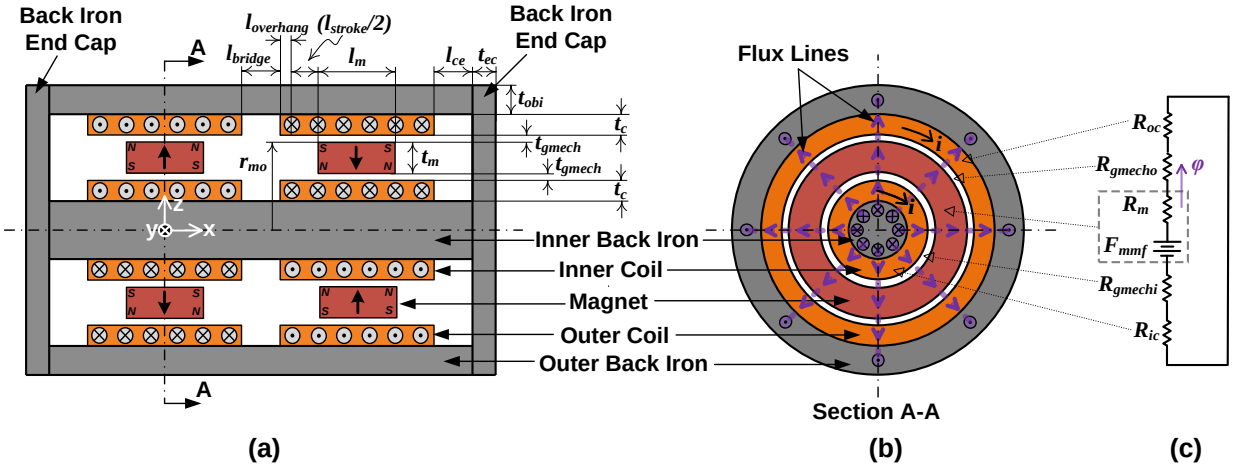

Figure 23: (a) A cross section of the MMA architecture (variation 4 in Table 1) taken along its lengthwise axis (the x-axis), labeled with the set of independent geometric parameters used to fully define and dimension the architecture geometry. (b) A cross section of one of the two concentric coil, radial magnet MMA building blocks that make up the MMA architecture, taken along the radial axis, showing the expected magnetic flux flow profile in the color purple. (c) The magnetic circuit representation of one of the concentric coil, radial magnet MMA building blocks.

Figure 23 shows two cross sections of the lumped parameter model of the concentric coil, radial magnet MMA architecture: one taken along the lengthwise axis (the x-axis) of the MMA and one taken along the radial axis of the MMA. Figure 23(a), the cross section taken along the lengthwise axis of the MMA, is labeled with the set of independent geometric parameters used to fully define and dimension the architecture geometry, and Figure 23(b), the cross section of the MMA architecture taken along the radial axis of the MMA, is overlaid with the expected magnetic flux flow profile present at that location. The dimensions l_m, t_m, and r_{mo} denote the magnet axial length, magnet radial thickness, and magnet outer radius, respectively. The dimensions t_c, l_{bridge}, and t_{gmech} denote the coil thickness, the axial distance between the two sets of concentric coil windings, and the mechanical air gap thickness between the magnet and the coil, respectively. The dimension l_{stroke} denotes the net stroke length of the actuator (i.e. the total range of motion), and the dimension $l_{overhang}$ denotes additional portions of coil winding that extend past the stroke length of the actuator for the purposes of improving force-stroke uniformity. The dimensions t_{ec} and t_{obi} denote the axial thickness of the back iron end cap and the radial thickness of the outer back iron, respectively. The dimension l_{ce} denotes the axial distance between the coil winding and the back iron end cap. It is noted here that the magnitude of $l_{overhang}$ was assumed to be small enough to have a negligible effect on the magnitude of the performance metric and was therefore omitted in the derivation of the closed form expression of the performance metric. The magnitude of $l_{overhang}$ is taken into consideration, however, during the FEA optimization step in the optimization process.

As is implied by Equations (69)-(71), deriving a closed form expression of the architecture's performance metric in terms of the geometric parameters that define it requires that one derive closed form expressions of the actuator output force, coil power dissipation, and permanent magnet mass. To simplify the process, these

expressions were first derived for one single concentric coil, radial magnet MMA building block, and then the expressions were multiplied by a factor of two to account for the other building block. To make this factor of two stand out, it is shown in curly brackets in the expressions of the actuator output force, coil power dissipation, and permanent magnet mass derived below.

Deriving closed form expressions of the actuator's coil power dissipation and permanent magnet mass is straightforward. The expressions for coil power dissipation (P_{CCRM}) and the permanent magnet mass (m_{mCCRM}) can be determined to be,

$$P_{CCRM} = \{2\} i^2 \left(R_{oc\_resis} + R_{ic\_resis} \right) = \{2\} i^2 \frac{\rho_c \left(l_{ocw} + l_{icw} \right)}{A_w} = \{2\} i^2 \rho_c \frac{8 t_c \left(2 r_{mo} - t_m \right) \left(l_m + l_s \right)}{d_w{}^4}, \tag{72}$$

and,

$$m_{mCCRM} = \{2\} \rho_m V_m = \{2\} \rho_m \pi l_m t_m \left(2 r_{mo} - t_m \right), \tag{73}$$

respectively, where R_{oc_resis} is the coil wire resistance of the outer coil, R_{ic_resis} is the coil wire resistance of the inner coil, ρ_c is the coil wire resistivity, A_w is the cross sectional area of the coil wire, d_w is the coil wire diameter, l_{ocw} is the wire length of the outer coil, l_{icw} is the wire length of the inner coil, ρ_m is the magnet mass density, and V_m is the magnet volume. Deriving a closed form expression of the actuator's output force is less straightforward. The Lorentz force law equation for the concentric coil, radial magnet MMA architecture is,

$$F_{CCRM} = \{2\} \left(B_{oc} i l_{ocw,magOL} + B_{ic} i l_{icw,magOL} \right) \tag{74}$$

where B_{ic} is the average magnetic flux density in the inner coil region, B_{oc} is the average magnetic flux density in the outer coil region, i is the coil current, $l_{ocw,magOL}$ is the length of wire in the outer coil winding through which magnet flux flows through at any given point along the MMA's range of motion, and $l_{icw,magOL}$ is the length of wire in the inner coil winding through which magnet flux flows through at any given point along the MMA's range of motion. Assuming that the wire in the coil winding is wound such that each row of wire turns is wound directly on top of the previous row of wire turns, the expressions for $l_{ocw,magOL}$ and $l_{icw,magOL}$ are,

$$\begin{aligned} l_{ocw,magOL} &= \frac{\pi l_m t_c (2 r_{mo} + 2 t_{gmech} + t_c)}{d_w{}^2}, \\ l_{icw,magOL} &= \frac{\pi l_m t_c (2 r_{mo} - 2 t_{gmech} - 2 t_m - t_c)}{d_w{}^2}. \end{aligned} \tag{75}$$

To derive closed form expressions of the magnetic flux density terms in Equation (74), the architecture is modeled and analyzed as a magnetic circuit. Figure 23(c) shows the magnetic circuit representation of one of the two MMA building blocks that make up the concentric coil, radial magnet MMA architecture. The magnetic circuit representation for the other building block is analogous to the one shown, negating the need to perform magnetic circuit analysis for two magnetic circuits. The following assumptions were made in the magnetic circuit analysis of the concentric coil, radial magnet MMA architecture:

1. The effects of flux fringing and flux leakage are negligible.
2. The permeability values of the permanent magnet, the coil winding, and the air are approximately equal to the permeability of a vacuum.
3. The permeability of the back iron is much larger than that of vacuum ($\mu_{iron} >> \mu_0$) and is constant. The reluctance of the back iron is therefore neglected.
4. The permanent magnets are uniformly magnetized in the radial direction.

Based on standard lumped parameter magnetostatic analysis [36], the magneto-motive force (F_{mmf}) and the lumped reluctances of the permanent magnet (R_m), outer coil (R_{oc}), inner coil (R_{ic}), outer mechanical air gap (R_{gmecho}), and inner mechanical air gap (R_{gmechi}) are given by,

$$F_{mmf} = \frac{B_r l_m}{\mu_m}, \qquad R_m = \frac{\ln\left(\frac{r_{mo}}{r_{mo}-t_m}\right)}{2\pi\mu_m l_m},$$
$$R_{oc} = \frac{\ln\left(\frac{r_{mo}+t_c+t_{gmech}}{r_{mo}+t_{gmech}}\right)}{2\pi\mu_c l_m}, \; R_{ic} = \frac{\ln\left(\frac{r_{mo}-t_m-t_{gmech}}{r_{mo}-t_m-t_c-t_{gmech}}\right)}{2\pi\mu_c l_m}, \tag{76}$$
$$R_{gmecho} = \frac{\ln\left(\frac{r_{mo}+t_{gmech}}{r_{mo}}\right)}{2\pi\mu_0 l_m}, \; R_{gmechi} = \frac{\ln\left(\frac{r_{mo}-t_m}{r_{mo}-t_m-t_{gmech}}\right)}{2\pi\mu_0 l_m},$$

where B_r is the remanent flux density of the permanent magnet, and μ_m, μ_c, and μ_0 are the permeabilities of the permanent magnet, coil, and vacuum, respectively.

Next, the resultant flux (ϕ) and the average magnetic flux density in the outer coil region (B_{oc}) and the inner coil region (B_{ic}) are given by,

$$\phi = \frac{F_{mmf}}{R_m + R_{oc} + R_{ic} + R_{gmecho} + R_{gmechi}},$$
$$B_{oc} = \frac{\phi}{A_{oc}} = \frac{\phi}{\pi l_m \left(t_c + 2\left(r_{mo} + t_{gmech}\right)\right)}, \tag{77}$$
$$B_{ic} = \frac{\phi}{A_{ic}} = \frac{\phi}{\pi l_m \left(t_c + 2\left(r_{mo} - t_m - t_c - t_{gmech}\right)\right)},$$

where A_{ic} is the cross-sectional area through which flux flows at the midway point along the radial thickness of the inner coil region and A_{oc} is the cross-sectional area through which flux flows at the midway point along the radial thickness of the outer coil region.

Having derived closed form expressions of the average magnetic flux densities in the outer and inner coil, a closed form expression of the actuator force output can now be obtained. Substituting the magnetic flux density expressions in Equation (77) and the coil wire length expressions in Equation (75) into the actuator force output expression in Equation (74), the actuator force output, F_{CCRM}, can be expressed as,

$$F_{CCRM} = \frac{\{2\}\frac{1}{d_w^{\,2}} 4\pi B_r i l_m t_m t_c}{\left(\ln\left(\frac{r_{mo}}{r_{mo}-t_m}\right) + \ln\left(\frac{r_{mo}+t_c+t_{gmech}}{r_{mo}+t_{gmech}}\right) + \ln\left(\frac{r_{mo}-t_m-t_{gmech}}{r_{mo}-t_m-t_c-t_{gmech}}\right) + \ln\left(\frac{r_{mo}+t_{gmech}}{r_{mo}}\right) + \ln\left(\frac{r_{mo}-t_m}{r_{mo}-t_m-t_{gmech}}\right)\right)}. \tag{78}$$

Substituting the power dissipation expression in Equation (72), the permanent magnet mass expression in Equation (73), and the actuator force output expression in Equation (78) into Equations (70) and (71), the definitions of the architecture's dynamic actuator constant and dynamic mass quantity, respectively, the dynamic actuator, β_{CCRM}, and dynamic mass quantity, $M_{dynamicCCRM}$, can be expressed as,

$$\beta_{CCRM} = \frac{\frac{B_r\sqrt{2\pi}}{\sqrt{\rho_m \rho_c}} \sqrt{\frac{1}{1+\frac{l_s}{l_m}}} \frac{\sqrt{t_m t_c}}{\left(2r_{mo}-t_m\right)}}{\left(\ln\left(\frac{r_{mo}}{r_{mo}-t_m}\right) + \ln\left(1+\frac{t_c}{r_{mo}+t_{gmech}}\right) + \ln\left(1+\frac{t_c}{r_{mo}-t_m-t_c-t_{gmech}}\right) + \ln\left(1+\frac{t_{gmech}}{r_{mo}}\right) + \ln\left(1+\frac{t_{gmech}}{r_{mo}-t_m-t_{gmech}}\right)\right)}, \tag{79}$$

and,

$$M_{dynamicCCRM} = \frac{\sqrt{\{2\}\pi\rho_m l_m t_m \left(2r_{mo} - t_m\right)}}{\{2\}\pi\rho_m l_m t_m \left(2r_{mo} - t_m\right) + m_p}, \tag{80}$$

respectively, which, in turn, implies that the architecture's performance metric, PM_{CCRM}, can be expressed as,

$$PM_{CCRM} = \frac{\dfrac{B_r\sqrt{2\pi}}{\sqrt{\rho_m\rho_c}}\sqrt{\dfrac{1}{1+\dfrac{l_s}{l_m}}}\dfrac{\sqrt{t_m t_c}}{\left(2r_{mo}-t_m\right)}\dfrac{\sqrt{\{2\}\pi\rho_m l_m t_m\left(2r_{mo}-t_m\right)}}{\{2\}\pi\rho_m l_m t_m\left(2r_{mo}-t_m\right)+m_p}}{\left(\ln\left(\dfrac{r_{mo}}{r_{mo}-t_m}\right)+\ln\left(1+\dfrac{t_c}{r_{mo}+t_{gmech}}\right)+\ln\left(1+\dfrac{t_c}{r_{mo}-t_m-t_c-t_{gmech}}\right)+\ln\left(1+\dfrac{t_{gmech}}{r_{mo}}\right)+\ln\left(1+\dfrac{t_{gmech}}{r_{mo}-t_m-t_{gmech}}\right)\right)}. \tag{81}$$

Note that the factor of two in the curly brackets that was incorporated into the closed form expressions of output force, power dissipation, and permanent magnet mass cancels out in the expression for the dynamic actuator constant but does not cancel out in the expressions for the dynamic mass quantity and the performance metric.

6.2 The inherent limitations of the closed form expression of the dynamic actuator constant: Constraints imposed by the expression's underlying assumptions

For the closed form expression of the dynamic actuator constant to yield a satisfactorily accurate approximation of the dynamic actuator constant, the assumptions taken at the beginning of the magnetic circuit analysis need to hold, necessitating the inclusion of constraints to the dynamic actuator constant expression that describe the conditions under which these assumptions hold. These constraints play an important role in two related but distinct phases of the optimization process: the phase of the optimization process in which an approximately optimal set of geometric parameters is identified via the closed form approximation of the dynamic actuator constant and the phase of the optimization process in which the overall size of the MMA is minimized. This distinction revolves around the optimization of two distinct sets of geometric parameters: the subset of geometric parameters that the closed form expression of the dynamic actuator constant is a function of and the subset of geometric parameters that the closed form expression of the dynamic actuator constant is not a function of due to the assumptions taken at the beginning of the magnetic circuit analysis. The two sets of geometric parameters are shown in the two cross sections of the concentric coil, radial magnet MMA architecture taken along its lengthwise axis in Figure 24. The cross sections are identical in every way except that the cross section in Figure 24(a) is labeled with the subset of geometric parameters that are present in the closed form expression of the dynamic actuator constant, while the cross section in Figure 24(b) is labeled with all of the geometric parameters are not present in the expression of the dynamic actuator constant. The optimization of the geometric parameters in Figure 24(a) corresponds to the phase of the optimization process in which an approximately optimal set of geometric parameters is identified via the closed form approximation of the dynamic actuator constant, while the optimization of the geometric parameters in Figure 24(b) corresponds to the phase of the optimization process in which the overall size of the MMA is minimized. In what follows below, the set of constraints imposed by the magnetic circuit analysis assumptions will be presented in the context of the two distinct optimization phases noted above.

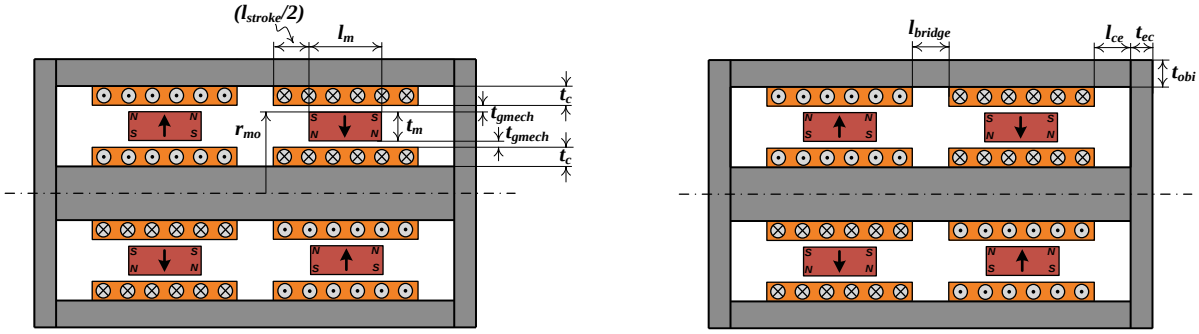

(a) **(b)**

Figure 24: (a) A cross section of the concentric coil, radial magnet MMA architecture taken along the lengthwise axis, labeled with all of the geometric parameters that the closed form expression of the dynamic actuator constant is a function of. (b) A cross section of the concentric coil, radial magnet MMA architecture taken along the lengthwise axis, labeled with all of the geometric parameters that the closed form expression of the dynamic actuator constant is *not* a function of. The magnitudes of the geometric parameters in Figure 24(b) were minimized or brought close to their minimum values to minimize the size of the MMA without affecting performance.

6.2.1 Constraints on the set of geometric parameters that the closed form expression of the dynamic actuator constant is a function of

The magnetic circuit analysis assumptions most likely to break down for a given set of the geometric parameters in Figure 24(a) and Figure 24(b) are assumption 1, the assumption that the effects of flux fringing and flux leakage are negligible, and assumption 3, the assumption that the permeability of the back iron is much larger than that of vacuum and is constant. Assumption 3 imposes the most critical constraint on the closed form expression of the dynamic actuator constant – the constraint that the inner back iron does not saturate. The inner back iron of the MMA is the section of the back iron that is most sensitive to saturation; it has the smallest cross-sectional area of all the different sections of flux-guiding iron that make up the back iron, and it has a quantity of flux passing through it that is greater than or equal to the largest amount of flux passing through any other section of the back iron. While constraints that ensure that assumptions 1 and 3 hold in regions of the MMA other than the inner back iron are also necessary for describing the conditions under which the closed form expression of the dynamic actuator is valid, these constraints, to be addressed in Section 6.2.2, can be easily satisfied for a given set of the geometric parameters in Figure 24(a). The saturation constraint on the inner back iron, on the other hand, cannot be easily satisfied for a given set of the geometric parameters in Figure 24(a) – the inner back iron will either saturate or it will not saturate. Hence, the following constraint must be attached to the closed form expression of the dynamic actuator constant for the expression to be valid,

$$B_{ibi} < B_{sat}\,, \tag{82}$$

where B_{ibi} is the magnetic flux density in the inner back iron, and B_{sat} is the magnetic flux density at which the back iron begins to saturate. The magnetic flux density in the inner back iron can be expressed as follows,

$$B_{ibi} = \frac{\phi}{2A_{ibi}}\,, \tag{83}$$

where A_{ibi} is the cross-sectional area of the inner back iron. Substituting the expression for flux in Equation (77) into Equation (83), the magnetic flux density in the inner back iron can be expressed as follows,

$$B_{ibi} = \frac{\dfrac{B_r l_m t_m}{\left(r_{mo} - t_m - t_c - t_{gmech}\right)^2}}{\left(\ln\left(\dfrac{r_{mo}}{r_{mo} - t_m}\right) + \ln\left(1 + \dfrac{t_c}{r_{mo} + t_{gmech}}\right) + \ln\left(1 + \dfrac{t_c}{r_{mo} - t_m - t_c - t_{gmech}}\right) + \ln\left(1 + \dfrac{t_{gmech}}{r_{mo}}\right) + \ln\left(1 + \dfrac{t_{gmech}}{r_{mo} - t_m - t_{gmech}}\right)\right)}\,. \tag{84}$$

Substituting Equation (84) into the constraint equation in Equation (82) implies that,

$$\frac{\dfrac{B_r l_m t_m}{\left(r_{mo} - t_m - t_c - t_{gmech}\right)^2}}{\left(\ln\left(\dfrac{r_{mo}}{r_{mo} - t_m}\right) + \ln\left(1 + \dfrac{t_c}{r_{mo} + t_{gmech}}\right) + \ln\left(1 + \dfrac{t_c}{r_{mo} - t_m - t_c - t_{gmech}}\right) + \ln\left(1 + \dfrac{t_{gmech}}{r_{mo}}\right) + \ln\left(1 + \dfrac{t_{gmech}}{r_{mo} - t_m - t_{gmech}}\right)\right)} < B_{sat}\,. \tag{85}$$

FEA simulations were used to confirm that the equations indicating saturation of the back iron are sufficiently accurate in identifying MMA geometries in which the inner iron saturates. Whenever the closed form expression of the dynamic actuator constant is used to approximate the dynamic actuator constant for a given set of geometric parameters, Equation (85) must be checked to determine whether or not the approximation is valid.

6.2.2 Constraints on the set of geometric parameters that the closed form expression of the dynamic actuator constant is not a function of

The set of constraints presented in this section are intended to be used as rules of thumb for approximating the conditions under which the geometric parameters in Figure 24(b) preserve the validity of magnetic circuit analysis assumptions underlying the closed form expression of the dynamic actuator constant. Because these constraints come in the form of restrictions on the minimum magnitudes of the geometric parameters in Figure 24(b), the constraints are useful for identifying the optimal set of the geometric parameters in Figure 24(b), where the optimal set of the geometric parameters in Figure 24(b) is defined as the set of parameters that minimize the overall size of the MMA without affecting the performance. The constraints presented can be used to develop a parametric model of the concentric coil, radial magnet MMA architecture that, given a set of the dimensions in Figure 24(a), automatically sizes the dimensions in Figure 24(b). Such a parametric model was used during many of the FEA simulations that were carried out as part of this research project. It is important to note that the set of constraints presented below are only rough approximations of the conditions under which the geometric parameters in Figure 24(b) preserve the validity of the magnetic circuit analysis assumptions. Factors of safety should be incorporated in parametric models of the concentric coil, radial magnet MMA that automatically size the dimensions in Figure 24(b) for a given a set of the dimensions in Figure 24(a). A factor of safety will be recommended for each of the constraints presented below. Ultimately, when honing in the truly optimal set of the geometric parameters in Figure 24(b), FEA simulations should be relied upon. The rules of thumb presented in this section can serve as a starting point during that process.

After the magnitudes of the geometric parameters in Figure 24(a) are selected, consideration of assumption 1, the assumption that the effects of flux fringing and flux leakage are negligible, and assumption 3, the assumption that the permeability of the back iron is much larger than that of vacuum and is constant, is necessary to minimize the size of the geometric parameters in Figure 24(b) without sacrificing performance. To adhere to the saturation constraint imposed by assumption 3, closed form expressions of the magnetic flux densities in the outer back iron and the back iron end caps can be derived to ensure that the thickness of the outer back iron, t_{obi}, and back iron end caps, t_{ec}, are large enough to prevent saturation. The saturation constraints imposed by assumption 3 can be stated as follows,

$$\begin{aligned} B_{obi} &< B_{sat}, \\ B_{ec} &< B_{sat}. \end{aligned} \tag{86}$$

where B_{obi} is the magnetic flux density in the outer back iron, and B_{ec} is the magnetic flux density in the back iron end cap. The magnetic flux densities in these sections of the back iron can be expressed as follows,

$$\begin{aligned} B_{obi} &= \frac{\phi}{2A_{obi}}, \\ B_{ec} &= \frac{\phi}{2A_{ec,\min}}, \end{aligned} \tag{87}$$

where A_{obi} is the cross-sectional area of the outer back iron, and $A_{ec,min}$ is the smallest cross-sectional area in the end cap through which flux flows through.

Substituting the expression for flux in Equation (77) into Equation (87), the magnetic flux density in the outer back iron and the end cap can be expressed as follows,

$$B_{obi} = \frac{\dfrac{B_r l_m t_m}{t_{oy}\left(2(r_{mo}+t_c+t_{gmech})+t_{oy}\right)}}{\left(\ln\left(\dfrac{r_{mo}}{r_{mo}-t_m}\right)+\ln\left(1+\dfrac{t_c}{r_{mo}+t_{gmech}}\right)+\ln\left(1+\dfrac{t_c}{r_{mo}-t_m-t_c-t_{gmech}}\right)+\ln\left(1+\dfrac{t_{gmech}}{r_{mo}}\right)+\ln\left(1+\dfrac{t_{gmech}}{r_{mo}-t_m-t_{gmech}}\right)\right)},$$

$$B_{ec} = \frac{\dfrac{B_r l_m t_m}{2t_{ec}\left(r_{mo}-t_c-t_{gmech}-t_m\right)}}{\left(\ln\left(\dfrac{r_{mo}}{r_{mo}-t_m}\right)+\ln\left(1+\dfrac{t_c}{r_{mo}+t_{gmech}}\right)+\ln\left(1+\dfrac{t_c}{r_{mo}-t_m-t_c-t_{gmech}}\right)+\ln\left(1+\dfrac{t_{gmech}}{r_{mo}}\right)+\ln\left(1+\dfrac{t_{gmech}}{r_{mo}-t_m-t_{gmech}}\right)\right)}. \quad (88)$$

Substituting the expressions of the magnetic flux densities in Equation (88) into the saturation constraints in Equation (86), the following constraints on the thickness of the outer back iron, t_{obi}, and the thickness of the back iron end caps, t_{ec}, can be derived,

$$t_{obi} > \left[\sqrt{\frac{B_r l_m t_m}{B_{sat}\psi}+(r_{mo}+t_c+t_{gmech})^2}-(r_{mo}+t_c+t_{gmech})\right] f_s,$$

$$t_{ec} > \left[\frac{B_r l_m t_m}{2B_{sat}\psi(r_{mo}-t_c-t_{gmech}-t_m)}\right] f_s, \quad (89)$$

where,

$$\psi = \left(\ln\left(\frac{r_{mo}}{r_{mo}-t_m}\right)+\ln\left(1+\frac{t_c}{r_{mo}+t_{gmech}}\right)+\ln\left(1+\frac{t_c}{r_{mo}-t_m-t_c-t_{gmech}}\right)+\ln\left(1+\frac{t_{gmech}}{r_{mo}}\right)+\ln\left(1+\frac{t_{gmech}}{r_{mo}-t_m-t_{gmech}}\right)\right), \quad (90)$$

and f_s is the factor of safety. A factor of safety of 1 for t_{obi} and 1 for t_{ec} is recommended as a first approximation of the minimum magnitude of t_{obi} and t_{ec}. For a more conservative estimation of the minimum magnitudes of t_{obi} and t_{ec}, a factor of safety of 1.5 is recommended.

To ensure that the effects of flux fringing and flux leakage can be ignored as stated in assumption 1, the dimension l_{bridge} needs to be large enough that the fringing flux from one magnet does not pass through the adjacent set of coils when the magnet is positioned at the extremes of the actuator stroke range. In addition, to avoid flux from leaking directly to the back iron end caps without passing through the coils, the axial distance between the coil winding and the back iron end cap, l_{ce}, should be large enough that the fringing flux from the magnets does not reach the end caps of the MMA when the magnet is positioned at the at the extremes of the actuator stroke range. Figure 25 illustrates how flux fringing in the concentric coil, radial magnet MMA architecture was modeled. The fringing flux at the ends of the magnet was assumed to have the shape of a circular arc with a radius equal to the thickness of the magnetic air gap, where the thickness of the magnetic air gap for the concentric coil, radial magnet MMA, t_{gmag}, is defined as,

$$t_{gmag} = t_c + t_{gmech}, \quad (91)$$

implying that the length that the magnetic field will fringe, l_{fringe}, is,

$$l_{fringe} = t_{gmag} = t_c + t_{gmech}. \quad (92)$$

Equation (92) implies that the following constraints on l_{bridge} and l_{ce} should prevent the effects of flux fringing from affecting performance,

$$l_{bridge} > l_{fringe} = \left(t_c + t_{gmech}\right) f_s ,$$
$$l_{ce} > l_{fringe} = \left(t_c + t_{gmech}\right) f_s . \quad (93)$$

A factor of safety of 1 for l_{bridge} and 1.5 for l_{ce} is recommended as a first approximation of the minimum magnitude of l_{bridge} and l_{ce}. The factor of safety of 1.5 that is recommended for a first approximation of the minimum magnitude of l_{ce} serves as more of a correction factor than a factor of safety, as several FEA simulations that were conducted with a factor of safety less than 1.5 for l_{ce} often led to small, but finite levels of undesirable axial back iron attraction between the permanent magnet closest to the back iron end cap and the back iron end cap. For a more conservative estimation of the minimum magnitudes of l_{bridge} and l_{ce}, a factor of safety of 1.5 is recommended for l_{bridge}, and a factor of safety of 2 is recommended for l_{ce}.

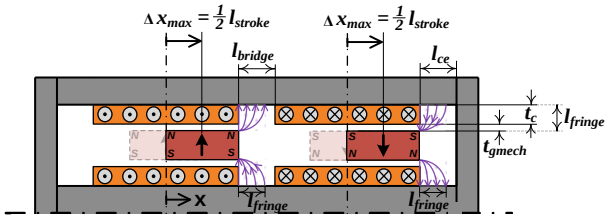

Figure 25: Flux fringing in the concentric coil, radial magnet MMA architecture.

6.3 A brute-force search approach to optimizing a concentric coil, radial magnet MMA design

The design of a concentric coil, radial magnet MMA was approached as an optimization problem in which, given a design space spanned by concentric coil, radial magnet MMA designs, the design that has the highest performance is sought. A systematic optimization process was developed and used to identify this optimal design. Referred to as the *coarse/fine brute-force search optimization process*, it comprises two separate processes that are carried out one after the other: the coarse brute-force search optimization process and the fine brute-force search optimization process. The coarse brute-force search optimization process is carried out first to identify the region of the concentric coil, radial magnet MMA design space in which the optimal design is located, and the fine brute-force search optimization process is carried out second to hone in on the optimal design's location in said region of the concentric coil, radial magnet MMA design space. This section of the thesis details the coarse/fine brute-force search optimization process in the context of the concentric coil, radial magnet MMA that was designed and constructed as a part of this research. Section 6.3.1 presents an overview of the coarse and fine brute-force search optimization processes. Section 6.3.2 details the coarse/fine brute-force search optimization process as it was applied during the design of the concentric coil, radial magnet MMA that was constructed as a part of this research. By the end of this section, it will be shown that:

1. The closed form approximation of the performance metric is sufficiently accurate over the concentric coil, radial magnet MMA design space of interest to reliably identify the region of the design space that contains the optimal design.
2. A variety of different concentric coil, radial magnet MMA geometries in a given design space can have comparably large performance metric values, giving the designer some freedom to accommodate other design considerations and priorities without compromising performance.
3. The optimal concentric coil, radial magnet MMA design that satisfies the actuator level design specifications in Table 4 corresponds to the design defined by the set of concentric coil, radial magnet MMA parameter values shown in Table 5.

The CCRM MMA parameter values identified as optimal and the final parameter values chosen during the detailed mechanical design phase of the design process				
Parameter Name	*Symbol*	*Value identified as optimal*	*Value of fabricated component*	*Units*
Stroke length[1,2]	l_{stroke}	10	10	[mm]
Payload mass[1,2]	m_p	0.7	0.7	[kg]
Magnet outer radius[2]	r_{mo}	32	32	[mm]
Magnet thickness[2]	t_m	8	8	[mm]
Magnet length[2]	l_m	32	32	[mm]
Coil thickness[2]	t_c	4	4	[mm]
Mechanical air gap thickness[2]	t_{gmech}	1.1	1.1	[mm]
Coil overhang[2]	$l_{overhang}$	2	2	[mm]
Outer back iron thickness[3]	t_{obi}	6	6.224	[mm]
Back iron end cap thickness[3]	t_{ec}	10	12.7	[mm]
Axial distance between coil windings and back iron end cap[3]	l_{ce}	8	6.35	[mm]
Axial distance between the two sets of coil windings[3]	l_{bridge}	9	12.7	[mm]
Permanent magnet mass density (assuming N52-grade Neodymium permanent magnet)[4]	ρ_m	7600	7600	[kg/m^3]
Remanent magnetization (assuming grade N52 Neodymium permanent magnet) [4]	B_r	≈1.4	≈1.4	[T]
Back iron permeability (assuming grade 1020C steel) [4]	μ_{steel}	$\mu_{steel} >> \mu_{vacuum}$	$\mu_{steel} >> \mu_{vacuum}$	
Flux density at saturation (assuming grade 1020C steel) [4]	B_{sat}	≈1.6	≈1.6	[T]
Coil wire resistivity (assuming copper) [4]	ρ_c	$1.68 \cdot 10^{(-8)}$	$1.68 \cdot 10^{(-8)}$	[Ω-m]

Table 5: The concentric coil, radial magnet MMA parameter values identified as optimal and the final parameter values of the concentric coil, radial magnet MMA that was constructed as a part of this thesis. Some of the final parameter values are not equal to their corresponding optimal parameter values due to mechanical design considerations. In the case of l_{ce}, the axial distance between coil windings and back iron end cap, the final parameter value should have been larger so that it matched the corresponding parameter value that was identified as optimal. This discrepancy was discovered after the MMA was constructed, however. The final parameter values that were selected during the detailed mechanical design phase of the design process make the constructed concentric coil, radial magnet MMA slightly larger than optimal. Of the values of the parameters that the performance metric expression is a function of, those that were identified as optimal remained unchanged during detailed mechanical design phase of the design process.

[1]Magnitude of parameter specified by the actuator level design specifications listed in Table 4.

[2]Geometric parameter that the performance metric is a function of.

[3]Geometric parameter that the performance metric is not a function of.

[4]Material property parameter

6.3.1 An overview of the coarse/fine brute-force search optimization process

The coarse brute-force search optimization process utilizes the closed form approximation of the performance metric to identify the region of the concentric coil, radial magnet MMA design space in which the optimal design is located, i.e., the neighborhood of the optimal design. The process involves using the closed form approximation of the performance metric to approximate the performance metric values of all the concentric coil, radial magnet MMA designs in the design space. The approximate performance metric values are subsequently mapped onto a "heat map" of the MMA design space – a visual representation of the design space in which the design space, the designs in the design space, and the magnitude of a parameter characteristic of each design in the design space are represented by a cell array, the cells of the cell array, and the fill color of the cells in the cell array, respectively. By choosing an appropriate color scale to represent the range of approximate performance metric values across the design space, the region of the design space that contains the optimal MMA design can be quickly

identified via visual inspection of the heat map of the approximate performance metric across the design space. After this region of the design space is identified, the fine brute-force search optimization process is carried out.

The fine brute-force search optimization process utilizes FEA simulations to identify the optimal design's exact location in the design space. The FEA simulations are used to obtain accurate force output approximations for the designs that span the region of the design space that was identified during the coarse brute-force search optimization process (i.e. the region of the design space that contains the optimal design). The accurate force output approximations are used to calculate accurate performance metric approximations for the designs that span this region of the design space. These performance metric approximations are considered to be accurate because they eliminate the primary source of error in the performance metric approximations obtained via the closed form approximations of the performance metric – the closed form approximation of the force output. Similar to the coarse brute-force search optimization process, these FEA-based performance metric approximations are presented in the form of a heat map.

6.3.2 Applying the coarse/fine brute-force search optimization strategy

This section details the coarse/fine brute-force search optimization process as it was applied during the design of a concentric coil, radial magnet MMA that satisfies the actuator level design specifications in Table 4. As the process is detailed, different factors that are important in the execution of the process will be noted, making the process more readily accessible to MMA designers in general. Emphasis is made on the development of heat map representations of the design space, as heat maps play a key role in the analysis and application of the coarse/fine brute-force search optimization process. The heat map's utility stems from the ease with which one can garner information from it; macro-level information regarding trends across the whole design space and micro-level information about individual elements in the design space. This can be seen in Figure 26 which shows the heat map of the approximate performance metric across the concentric coil, radial magnet MMA design space that was generated during the coarse brute-force search optimization process. The spectrum of colors in each color scale is such that the large and small performance metric values are represented by the bright and dark ends of the spectrum, respectively, making it easy to identify the high performance designs in each respective design space.

The heat maps in this thesis were generated in MATLAB with the function "`imagesc(C)`" which displays the data in array `C` as an image in which each element in `C` is represented by a color. The function "`colormap(map)`" was used to select the spectrum of colors in each heat map's color scale. The "`colormap`" portion of the code refers to the color scale, and the "`map`" input refers to the spectrum of colors to use in the color scale. MATLAB's built-in colormap called "`hot`" was used as the "`map`" input for all of the heat maps in this section. The function "`caxis([cmin cmax])`" was used in generating each heat map so that different sets of data that are presented in each heat map use the same color scale – a color scale that uses the brightest color in the "`hot`" colormap to represent the largest value in all of the data sets, i.e. "`cmax`", and the darkest color in the "`hot`" colormap to represent the smallest value in all of the data sets, i.e. "`cmin`". Examples of the code used to generate the heat maps are shown in Appendix B.

Before proceeding to detail the coarse/fine brute-force search optimization process and the generation of heat maps that result from the processes, it is important to note that the heat maps of the concentric coil, radial magnet MMA design space can be limited in their utility if not used appropriately. This is because the heat maps of the concentric coil, radial magnet MMA design space are a representation of a multi-dimensional design space. The design space of a concentric coil, radial magnet MMA is a multi-dimensional design space because the design of the MMA is defined by set of parameter values that define it, which implies that the design space is filled with all of the unique designs that can be realized with different combinations of different values of each parameter. Each parameter value that can be varied is an additional dimension. If the dimension of the design space is too large, the generation and interpretation of the heat maps becomes more complex. The heat maps in this section are representations of a four dimensional design space; one that only contains MMA designs that can be realized with different combinations of different values of the following four parameters: the magnet outer radius, r_{mo}, the magnet thickness, t_m, the coil thickness, t_c, and the magnet length, l_m. For all of the concentric coil, radial magnet MMA designs that are represented in these heat maps, the values associated with the rest of the parameters that define its design are held at a constant value. The extra effort that would have been necessary to make and use a design space of five or more dimensions was able to be avoided by recognizing that certain parameters should take on certain values regardless of the values that other parameters take. For example, regardless of the values of the other parameters, the value of a concentric coil, radial magnet MMA's mechanical air gap thickness, t_{gmech}, should be minimized. Therefore, in defining the design space of the concentric coil, radial magnet MMA that was constructed as a part of this research, the mechanical air gap thickness was held constant at the smallest possible value that is

practically feasible. Out of the 10 different concentric coil, radial magnet MMA parameters in the equation for the concentric coil, radial magnet MMA's performance metric, six of them were able to be identified as having a constant value that it should take on. The justification for holding these six parameters fixed at constant values is presented in the next several paragraphs.

To generate a heat map of a design space, the design space and its contents need to first be defined. In general, a design space is defined by design constraints that impose certain criteria on the elements that fill the space. In the case of a concentric coil, radial magnet MMA design space, these design constraints can be grouped into two categories: design constraints that arise from actuator level design specifications and design constraints that arise from the limitations of mechanical design. The key design constraints that arise from actuator level design specifications are constraints on the actuator's stroke length, l_s, payload mass, m_p, and footprint size (specifications on the maximum radial and/or axial dimensions of the actuator), while the key design constraints that arise from the limitations of mechanical design are constraints on the material properties of the actuator components, constraints on the magnitude of the mechanical air gap thickness, t_m, and a physical realizability constraint that ensures that the dimensions of the actuator components are compatible with one another. In defining the design space from which the MMA design described in this work was selected, the actuator level design specifications in Table 6 served as design constraints. Because the constraints that arise from the limitations of mechanical design are generally common to all concentric coil, radial magnet MMA designs, it can be said that the design space of a concentric coil, radial magnet MMA is primarily defined by the actuator level design specifications that the concentric coil, radial magnet MMA is intended to satisfy.

Design constraints from actuator level design specifications	
Stroke length, l_s	10 [mm]
Payload mass, m_p	0.7 [kg]
Maximum magnet length, $l_{m,max}$	32 [mm]
Maximum magnet outer radius, $r_{mo,max}$	32 [mm]

Table 6: Design constraints imposed by actuator level design specifications.

The material properties of the various actuator components are constrained by the available selection of materials. Prior work has shown that the permanent magnet material of N52-grade neodymium, the coil winding material of copper, and the back iron material of grade 1020C steel have favorable material properties that translate to relatively high performance [1][5]. Hence, in defining the design space from which the MMA design described in this work was selected, the material properties associated with these materials were held fixed as constants. Table 7 summarizes this constraint, listing the pertinent material property values of the materials selected for each of the major MMA components.

Material selected for each actuator component			
Actuator component	*Material Chosen*	*Pertinent material property constraint*	
Permanent magnet	Grade N52 Neodymium	Mass density, ρ_m	7600 [kg/m^3]
		Remanent magnetization, B_r	≈1.4 [T]
Back Iron	Grade 1020C Steel	Permeability, μ_{steel}	$\mu_{steel} >> \mu_{vacuum}$
		Flux density at saturation, B_{sat}	≈1.6 [T]
Coil windings	Copper	Coil wire resistivity, ρ_c	$1.68 \cdot 10^{(-8)}$ [Ω-m]

Table 7: Design constraints imposed by the material selected for each MMA component. The permeability of steel is assumed to be constant and several orders of magnitude higher than that of vacuum.

The magnitude of the mechanical air gap thickness, t_{gmech}, was selected to be as small as possible in order to minimize the mechanical air gap's contribution to the overall reluctance of the MMA's magnetic circuit. Due to the performance limitations of the fabrication processes used to fabricate the concentric coil, radial magnet MMA's components, the smallest achievable mechanical air gap thickness for the concentric coil, radial magnet MMA design in this thesis was restricted to 1.1 [mm]. In other instances and with better manufacturing capabilities, one might be able to use a smaller mechanical air gap as well. In that case, one could simply repeat the design optimization methodology that is laid out here, with a different constant value for this particular MMA design parameter. In defining the design space from which the MMA design described in this work was selected, the magnitude of the mechanical air gap thickness, t_{gmech}, was held fixed at 1.1 [mm]. Table 8 lists this constraint as well

as the last key mechanical design constraint; a physical realizability constraint that ensures that the set of magnitudes associated with the magnet outer radius, r_{mo}, magnet thickness, t_m, coil thickness, t_c, and mechanical air gap thickness, t_{gmech}, translate to an MMA that is physically realizable.

Mechanical design constraints on the design space	
Mechanical air gap thickness, t_{qmech}	1.1 [mm]
Physical realizability constraint	$r_{mo} - t_m - t_{gmech} - t_c > 0$

Table 8: Design constraints imposed by the limitations of mechanical design.

The concentric coil, radial magnet MMA design space comprises all the designs that satisfy the criteria established by the design constraints listed in Table 6, Table 7, and Table 8 above. Given these design constraints, the designs that span the concentric coil, radial magnet MMA design space are all the designs that can be realized by combinations of the "free" parameters listed in Table 9. The parameters in Table 9 are referred to as "free" parameters because they are not fixed to one constant value. They are, however, fixed to a range of values that are compatible with the set of design constraints specified in Table 6, Table 7, and Table 8.

Free geometric parameters
Magnet length, l_m
Magnet outer radius, r_{mo}
Coil thickness, t_c
Magnet thickness, t_m

Table 9: "Free" geometric parameters.

Figure 26 shows the heat map of the approximate performance metric across a select portion of the full design space. The heat map of the approximate performance metric across the design space can theoretically be designed to show the approximate performance metric value of every single design in the design space – an infinite number of approximate performance metric values for the infinite number of MMAs in the design space, all in one figure. This is not practical, however. To limit the number of designs that are represented in the heat map, an appropriate range and resolution should be selected for each free geometric parameter, where, in this context, the range of a geometric parameter is defined as the lower and upper bound of the geometric parameter values to display in the heat map, and the resolution is defined as the "distance" between neighboring geometric parameter values in the heat map. In generating the heat map in Figure 26, the range and resolution selected for each free geometric parameter are shown in Table 10. Note that the range that was selected for each geometric parameter is smaller than the largest range that is allowed by the design constraints listed in Table 6, Table 7, and Table 8; the design constraints that define the concentric coil, radial magnet MMA design space. This was done for the purposes of presentation – the smaller ranges allowed for the heat maps to be presented with a higher resolution. The regions of the design space that are left out by the smaller ranges are spanned with designs that have relatively small performance metric values and offer little academic or design insight.

Geometric parameters spanned when generating heat map		
Parameter	Range	Resolution
Magnet length, l_m	10-32 [mm]	steps of 2 [mm]
Magnet outer radius, r_{mo}	28-32 [mm]	steps of 2 [mm]
Coil thickness, t_c	2-8 [mm]	steps of 2 [mm]
Magnet thickness, t_m	2-10 [mm]	steps of 2 [mm]

Table 10: Range and resolution of the "free" geometric parameters used to generate the heat map representation of the design space in Figure 26.

For the optimal concentric coil, radial magnet MMA design to be within the bounds of the ranges of the geometric parameters listed in Table 10, the closed form approximation of the performance metric has to be sufficiently accurate within these bounds. Before continuing to detail the brute-force search optimization process and the subsequent fine brute-force search optimization process, an evaluation of the accuracy of the closed form approximation of the performance metric will be presented. It will be shown that the closed form approximation of the performance metric is sufficiently accurate over the design space defined by Table 6, Table 7, Table 8, and Table

10 for the brute-force search optimization process to reliably identify the region of the design space in which the optimal concentric coil, radial magnet MMA design is located.

The discrepancy between the closed form approximation and FEA approximation of the performance metric is wholly due to the discrepancy between the closed form approximation and FEA approximation of the dynamic actuator constant. This implies that the measure of accuracy of the closed form approximation of the dynamic actuator constant is equivalent to the measure of the accuracy of the closed form approximation of the performance metric. It was therefore decided to obtain a measure of the accuracy of the closed form approximation of the dynamic actuator constant. This was done by comparing the dynamic actuator constant values obtained via the closed form approximation of the dynamic actuator constant to the dynamic actuator constant values obtained via FEA simulations. This comparison was conducted over a design space that is larger than the design space established by the free parameters in Table 10. A larger design space was chosen for the comparison in order to gain a broader understanding of the accuracy limitations of the closed form approximation of the dynamic actuator constant and therefore, the closed form approximation of the performance metric. The range and resolution of the free geometric parameters that define this larger design space are listed in Table 11. Note that the only difference between the smaller design space defined by Table 6, Table 7, Table 8, and Table 10 and the larger design space over which this comparison takes place are the ranges of the free parameters in Table 10. This implies that the conclusions that follow from the following analysis of the accuracy of the closed form approximation of the dynamic actuator constant are, in principle, only applicable to the design space defined by Table 6, Table 7, Table 8, and Table 11; however, they may be applicable to a broader design space as well.

Dimensions spanned for FEA vs CF comparison		
Dimension	Range	Resolution
Magnet length, l_m	4-40 [mm]	steps of 4 [mm]
Magnet outer radius, r_{mo}	28-36 [mm]	steps of 4 [mm]
Coil thickness, t_c	2-14 [mm]	steps of 4 [mm]
Magnet thickness, t_m	2-14 [mm]	steps of 4 [mm]

Table 11: Range and resolution of the design space over which the accuracy of the closed form approximation of the dynamic actuator constant was measured.

The heat map of the closed form approximation of the dynamic actuator constant across this larger design space is shown in Figure 27. The heat map of the FEA-based approximations of the dynamic actuator constant across this larger design space is shown in Figure 28. When compared to the dynamic actuator constant values obtained via FEA simulations, the percent error of the closed form approximation of the dynamic actuator can be calculated by,

$$\%_{error} = \frac{\beta_{CF} - \beta_{FEA}}{\beta_{FEA}} \cdot 100 \,, \tag{94}$$

where β_{CF} is the dynamic actuator constant value obtained via the closed form approximation of the dynamic actuator constant, and β_{FEA} is the dynamic actuator constant value obtained via FEA simulations. The percent error of the closed form approximation of the dynamic actuator constant was calculated for every concentric coil, radial magnet MMA design in the larger design space defined by Table 6, Table 7, Table 8, and Table 11. The results are displayed in Figure 29 in a format similar to a heat map. Excluding designs that have a magnet length, $l_m \leq 8$ [mm], the average percent error across the design space is 10.2% with a standard deviation of 2.3%. The median percent error is 10.6%. The statistics imply that the primary cause of error of the closed form approximation of the performance metric across the majority of the design space is due to the same set of factors. A full investigation of what these factors are is beyond the scope of this thesis. The small standard deviation of the percent error implies that the closed form approximation of the dynamic actuator constant has a high level of consistency over the majority of the design space, suggesting that the trends that are captured by it are fairly accurate over the majority of the design space. This implies that it can be used to identify the optimal concentric coil, radial magnet MMA design in the design space of interest for the concentric coil, radial magnet MMA that was constructed as a part of this research. The accuracy of the closed form approximation of the performance metric implies that the actual performance metric value as predicted by FEA simulations will be ~10% less than what is predicted by the closed form approximation of the performance metric. The percent error of the closed form approximation of the dynamic actuator constant of every concentric coil, radial magnet MMA design in the larger design space defined by Table 6,

Table 7, Table 8, and Table 11 was recalculated by including a correction factor that reduces the closed form approximation of the dynamic actuator constant by 10%. The following equation was used to calculate this percent error,

$$\%_{error} = \frac{(\beta_{CF} \cdot f_c) - \beta_{FEA}}{\beta_{FEA}} \cdot 100 \,, \tag{95}$$

where f_c is the correction factor. The retabulated percent error of the closed form approximation of the dynamic actuator constant when using a correction factor, f_c=0.9, is shown in Figure 30. With the inclusions of this correction factor, all of the concentric coil, radial magnet MMA designs in the design space with a magnet length, $l_m \geq$16mm, are within +/- 4.9% of the FEA simulation approximations of the performance metric, and those designs with a magnet length, $l_m \geq$12mm, are within +/- 6.7% of the FEA simulation approximations of the dynamic actuator constant.

Figure 29 and Figure 30 show that the concentric coil, radial magnet MMA designs whose closed form approximations of the dynamic actuator constant tend to have the greatest percent errors are those designs whose parameters are such that the assumptions taken in deriving the closed form approximation of the dynamic actuator constant begin to break down. The following trends and observations were drawn from analysis of Figure 29 and Figure 30:

1. The closed form approximation of the dynamic actuator for designs that have a magnet length, l_m=4 [mm], tend to have a relatively large percent error. For a given r_{mo}, t_c, and t_m, as the magnet length increases, the percent error trends towards a constant value. This is expected because as the magnet length, l_m, increases, the fraction of flux that fringes in the magnetic circuit decreases. This assertion is supported by the fact that the larger the magnetic air gap ($t_{gmag} = t_c + t_{gmech}$) of the design, the longer the magnet length needs to be for the percent error to converge to its "equilibrium" value. This assertion is also supported by the fact that, for a given r_{mo}, t_m, and l_m, as t_c increases, percent error increases, and for smaller l_m values, the rate at which this percent error increases as t_c increases becomes even more pronounced.
2. Given an r_{mo}, a small l_m, and a t_m value, the percent error increases as t_c increases, and the rate at which percent error increases as t_c increases becomes more pronounced the larger the t_m value. Given an r_{mo}, a large l_m, and a t_m value, for $t_c \geq$6 [mm], the rate of increase in percent error as t_m increases is roughly constant as t_c increases. These observations suggest that the closed form approximation of the dynamic actuator constant of designs with a large net magnetic circuit reluctance tends to have a greater percent error than the closed form approximation of the dynamic actuator constant of designs with a smaller net magnetic circuit reluctance. A full investigation of the degree to which magnetic circuit reluctance affects the percent error of the closed form approximation of the dynamic actuator constant is beyond the scope of this thesis, as well as a full investigation of the possible reasons for this phenomenon.
3. Given an r_{mo}, a $l_m \geq$8 [mm], and a $t_c \leq$2 [mm], the percent error generally decreases as t_m increases. For some designs, the percent error begins to increase after initially decreasing as t_m increases. For designs with a larger t_c value, the percent error generally increases as t_m increases. A full investigation of the factors behind this trend is beyond the scope of this thesis.
4. Given a t_c, t_m, and l_m, the rate at which percent error increases as r_{mo} increases is very small; nearly zero. The exception to this trend is for designs that have an $l_m \leq$8 [mm], a $t_c \geq$10 [mm], and a $t_m \geq$10 [mm]. For these designs, the percent error increases as r_{mo} increases. A full investigation of the factors behind this trend is beyond the scope of this thesis.
5. With regards to the magnetic circuit reluctance contributions associated with the magnetic air gap thickness, t_{gmag}, and a given magnetic thickness, t_m, an increase in t_c results in a greater rate of increase in percent error than when t_c is constant and t_m increases. This is likely due to the fringing effects associated with the magnetic air gap. The magnetic air gap grows larger for an incremental increase in coil thickness than for an incremental increase in magnet thickness because there are two coil windings (the inner and the outer coils winding) for every magnet.

Although the closed form approximation of the performance metric tends to have a percent error of ≈10% in the design space under consideration for the concentric coil, radial magnet MMA design that was designed and constructed as a part of this research, its consistency over the design space is sufficiently high that the closed form approximation of the performance metric can be used to identify the optimal design in the design space of interest via the rough/fine brute force search optimization process. It was decided to forgo the inclusion of the correction factor in Equation (95) in the closed form approximation of the performance metric because the effects or factors

that the correction factor seemingly corrects for are not fully understood and beyond the scope of this thesis. Therefore, the heat map representation of the closed form approximation of performance metric over the design space described in Table 10 was used to identify the region of the design space that contains the optimal design. The region of the design space that was identified is shown in Figure 31 in a high resolution heat map of the closed form approximation of the performance metric across this region of the design space. A high resolution heat map of the FEA-based approximation of performance metric across this region of the design space is shown in Figure 31. Both figures are in agreement with the fact that the performance metric values of the concentric coil, radial magnet MMA designs in this region of the design space have performance metric values that are very close in magnitude. The average performance metric value for Figure 31, the heat map with the FEA-based performance metric values, is 21.5 [$\sqrt{Hz} \cdot \sqrt{\frac{1}{kg}}$] with a standard deviation of 0.4 [$\sqrt{Hz} \cdot \sqrt{\frac{1}{kg}}$]. The median performance metric value is 21.6 [$\sqrt{Hz} \cdot \sqrt{\frac{1}{kg}}$]. Both figures are also in agreement on the location of the optimal concentric coil, radial magnet MMA design in the design space, implying that the closed form approximation of the performance metric is precise enough to use in the fine brute force search optimization process instead of the FEA simulations prescribed by the fine brute force search optimization process. The location of the optimal concentric coil, radial magnet MMA design in this region of the design space corresponds to the following geometric parameter values: t_c=4 [mm], t_m=8 [mm], r_{mo}=32 [mm], and l_m=32 [mm], and the FEA-based approximation of the performance metric value of this optimal concentric coil, radial magnet MMA design is 22.2 [$\sqrt{Hz} \cdot \sqrt{\frac{1}{kg}}$].

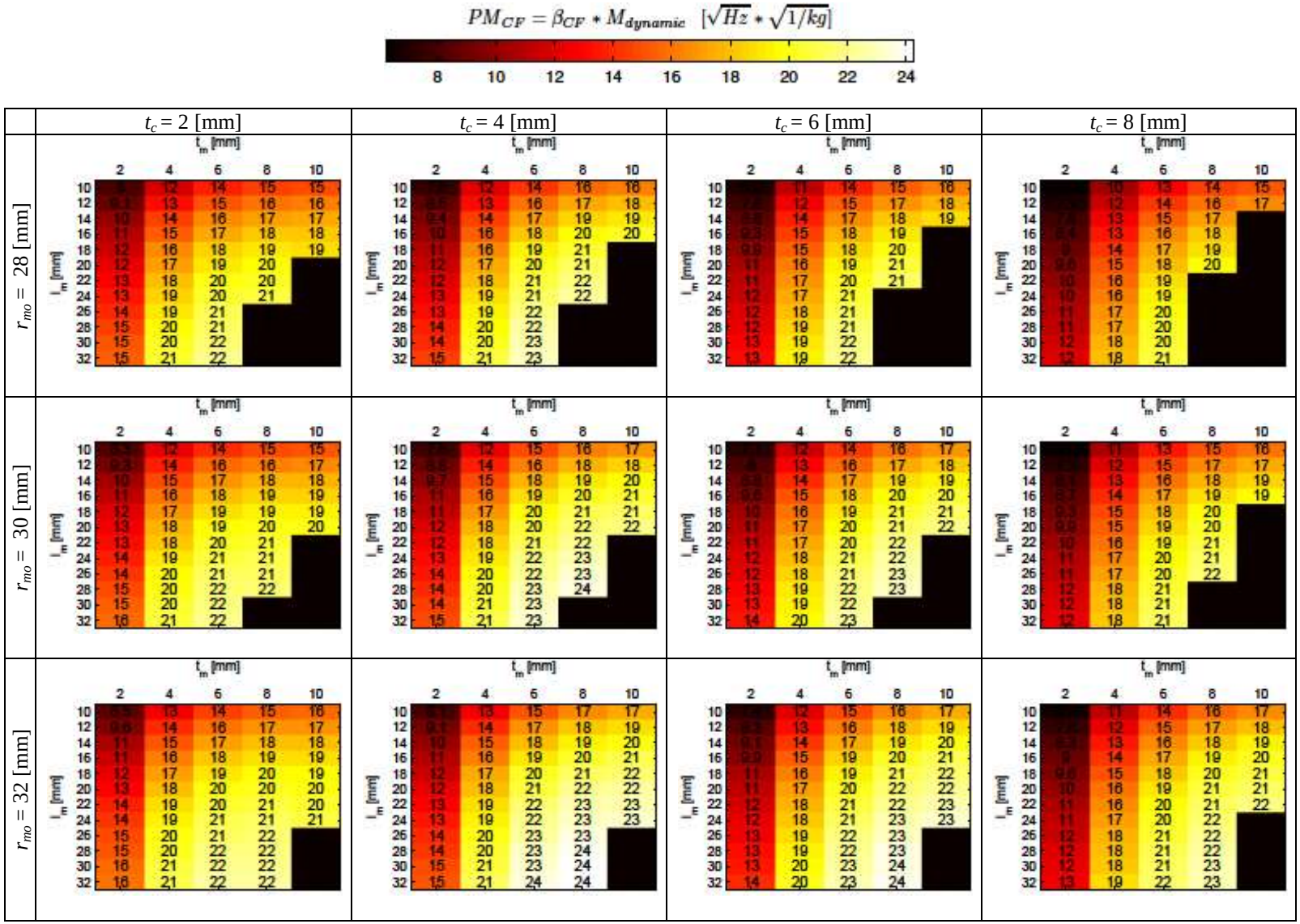

Figure 26: Heat map representation of the closed form approximation of performance metric across the design space described in Table 6, Table 7, Table 8, and Table 10. The concentric coil, radial magnet MMA designs that lead to saturation in the inner iron are blacked out. Geometries that are non-realizable due to the design constraint listed in Table 8 are also blacked out. The mass of the payload in these approximations is 0.7 [kg].

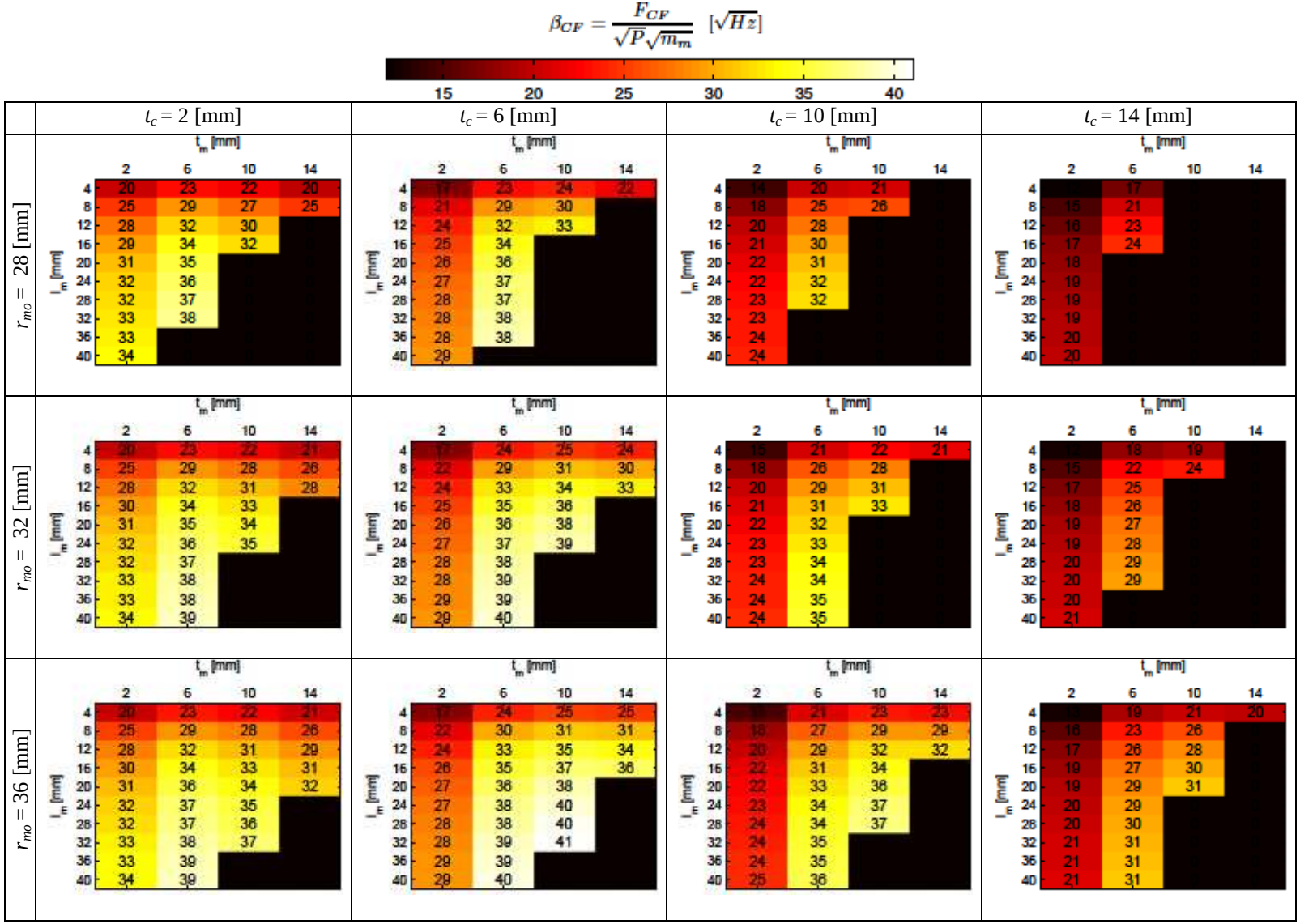

Figure 27: Heat map representation of the closed form approximation of the dynamic actuator constant across the relatively large design space defined by Table 6, Table 7, Table 8, and Table 11. The concentric coil, radial magnet MMA designs that lead to saturation in the inner iron are blacked out. Geometries that are non-realizable due to the design constraint listed in Table 8 are also blacked out. The mass of the payload in these approximations is 0.7 [kg].

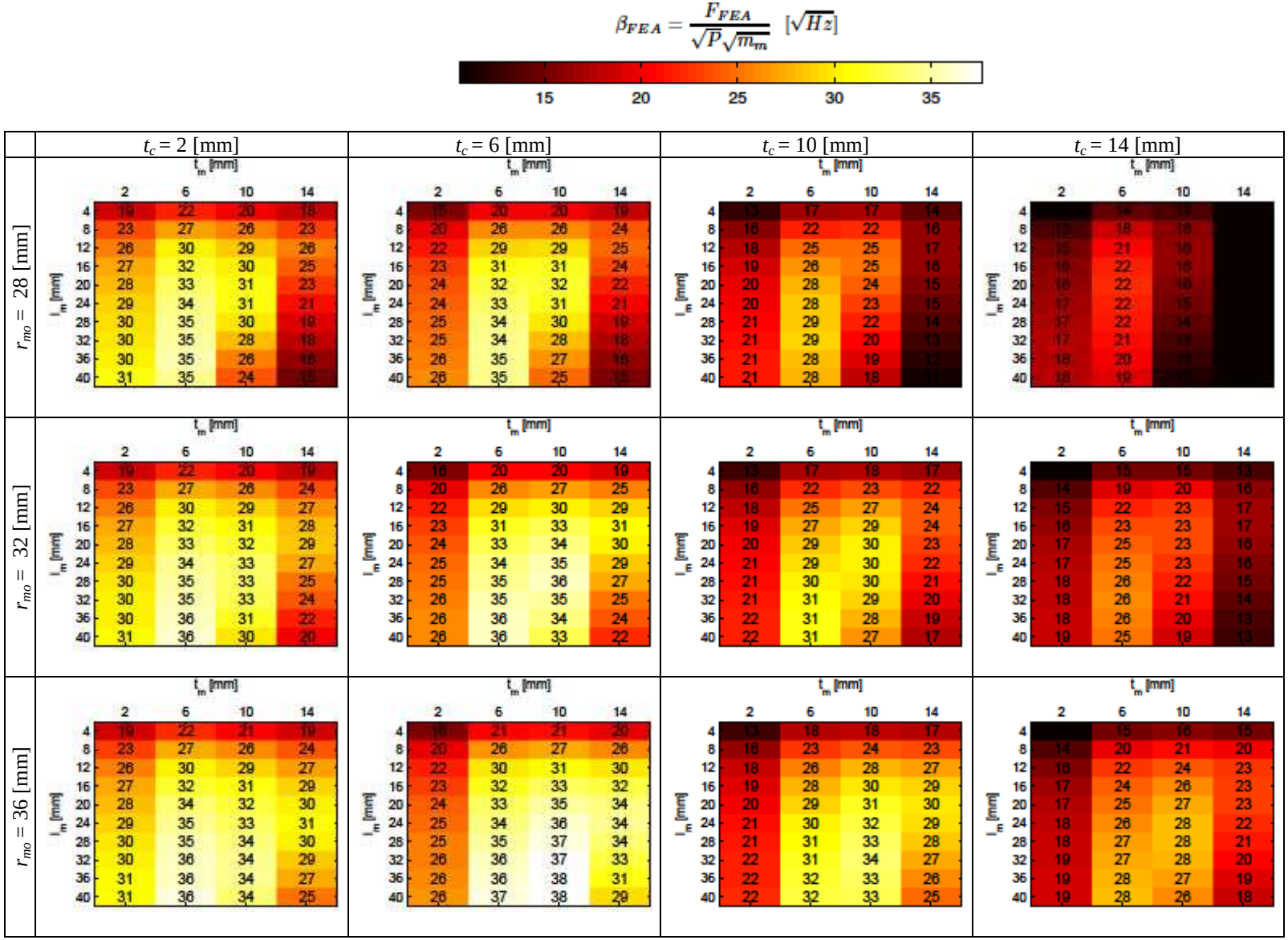

Figure 28: Heat map representation of the Maxwell FEA simulation approximation of the dynamic actuator constant over the relatively large design space described by Table 6, Table 7, Table 8, and Table 11. The concentric coil, radial magnet MMA designs that are non-realizable due to the design constraint listed in Table 8 are blacked out.

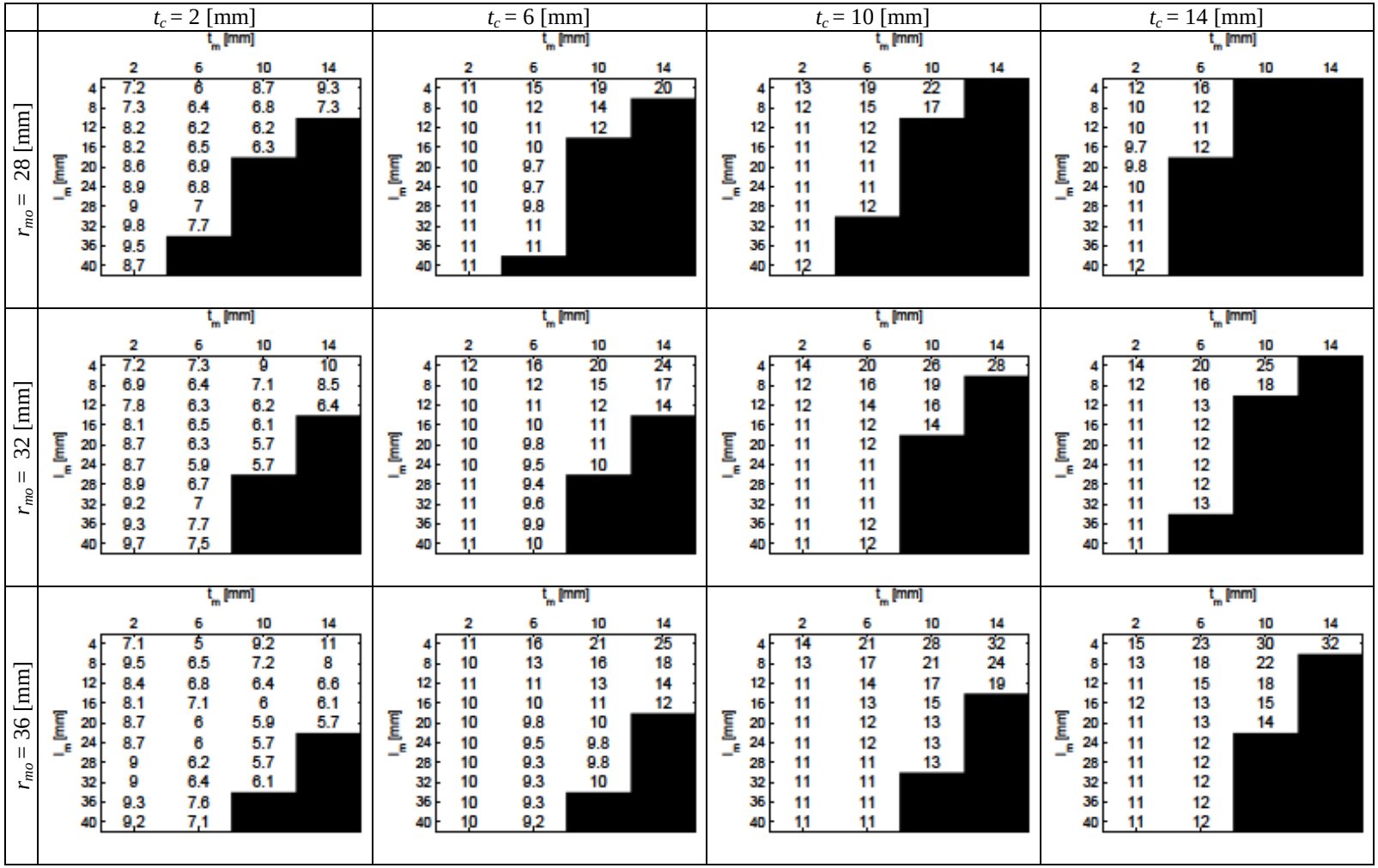

Figure 29: Percent error of the closed form approximation of the dynamic actuator constant when compared to the dynamic actuator constant approximations obtained via FEA simulations over the relatively large design space described in Table 6, Table 7, Table 8, and Table 11. The results have the concentric coil, radial magnet MMA designs that lead to saturation in the inner iron blacked out, as well as the geometries that are non-realizable due to the design constraint listed in Table 8.

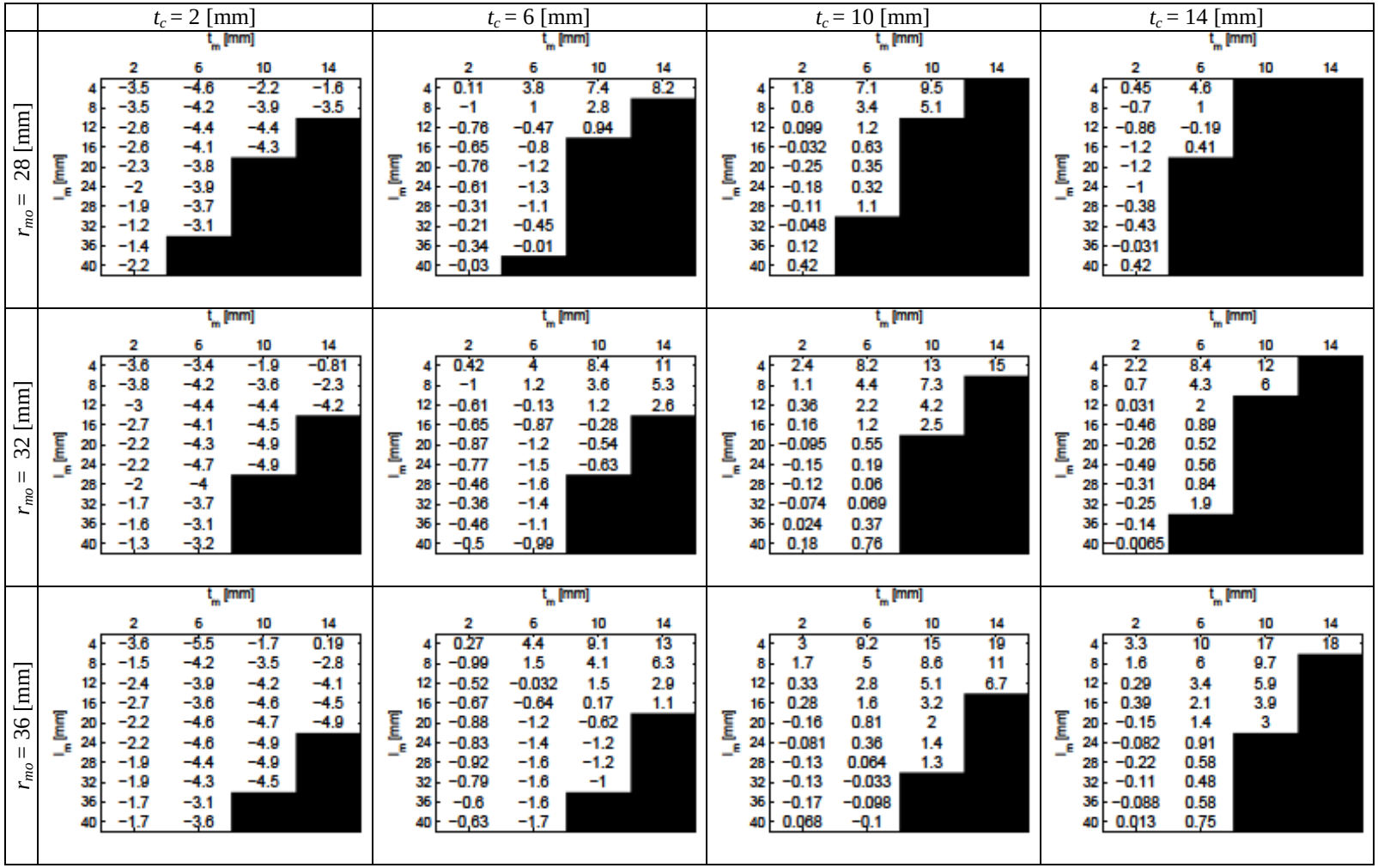

Figure 30: Percent error of the closed form approximation of the dynamic actuator constant that incorporates a correction factor of 0.9 when compared to the dynamic actuator constant values obtained via FEA simulations over the relatively large design space described in Table 6, Table 7, Table 8, and Table 11. The results have the concentric coil, radial magnet MMA designs that lead to saturation blacked out, as well as the geometries that are non-realizable due to the design constraint listed in Table 8.

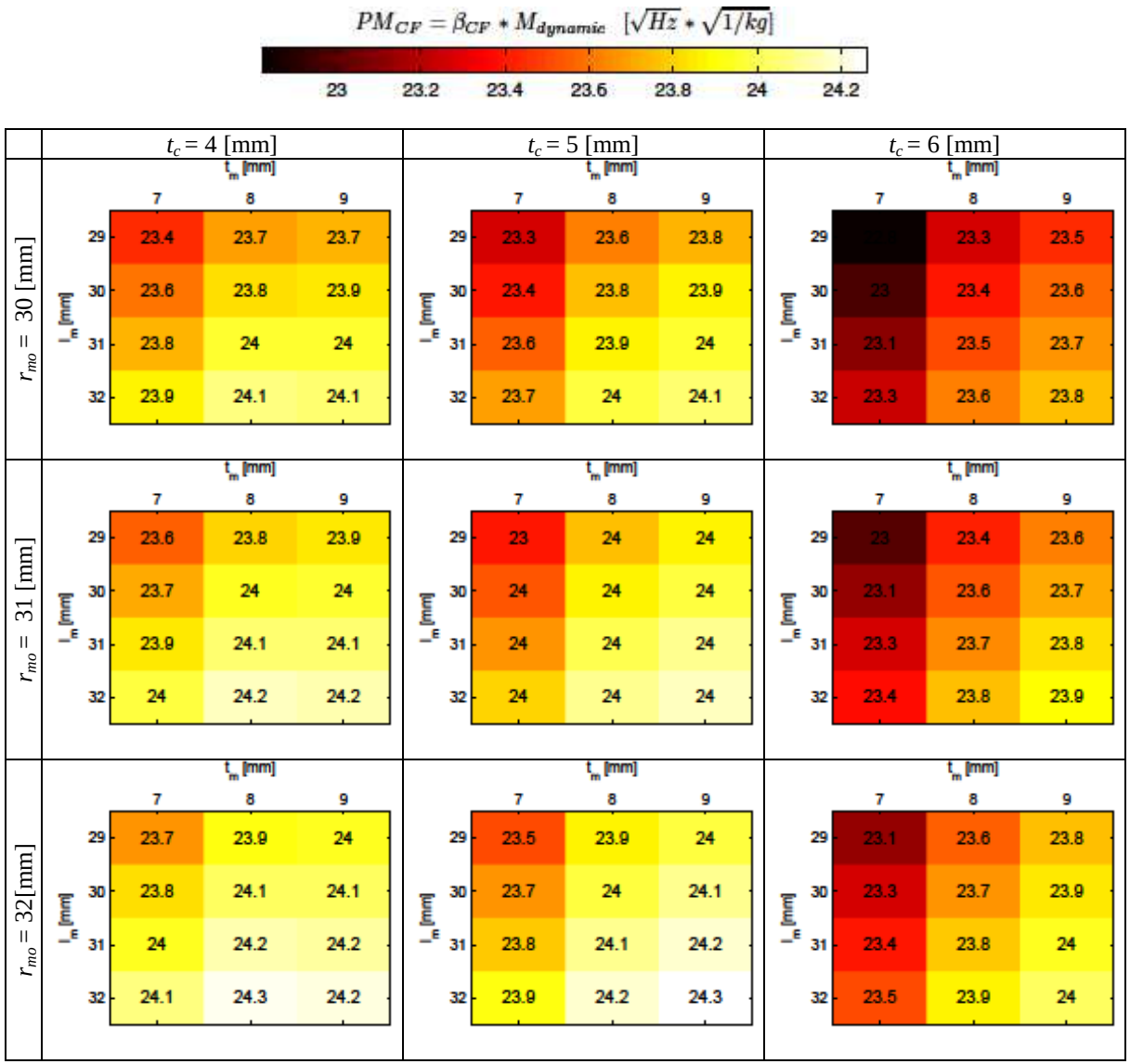

Figure 31: Heat map representation of the closed form approximations of the performance metric over the region of the design space that includes the optimal design. The mass of the payload in these approximations is 0.7 [kg].

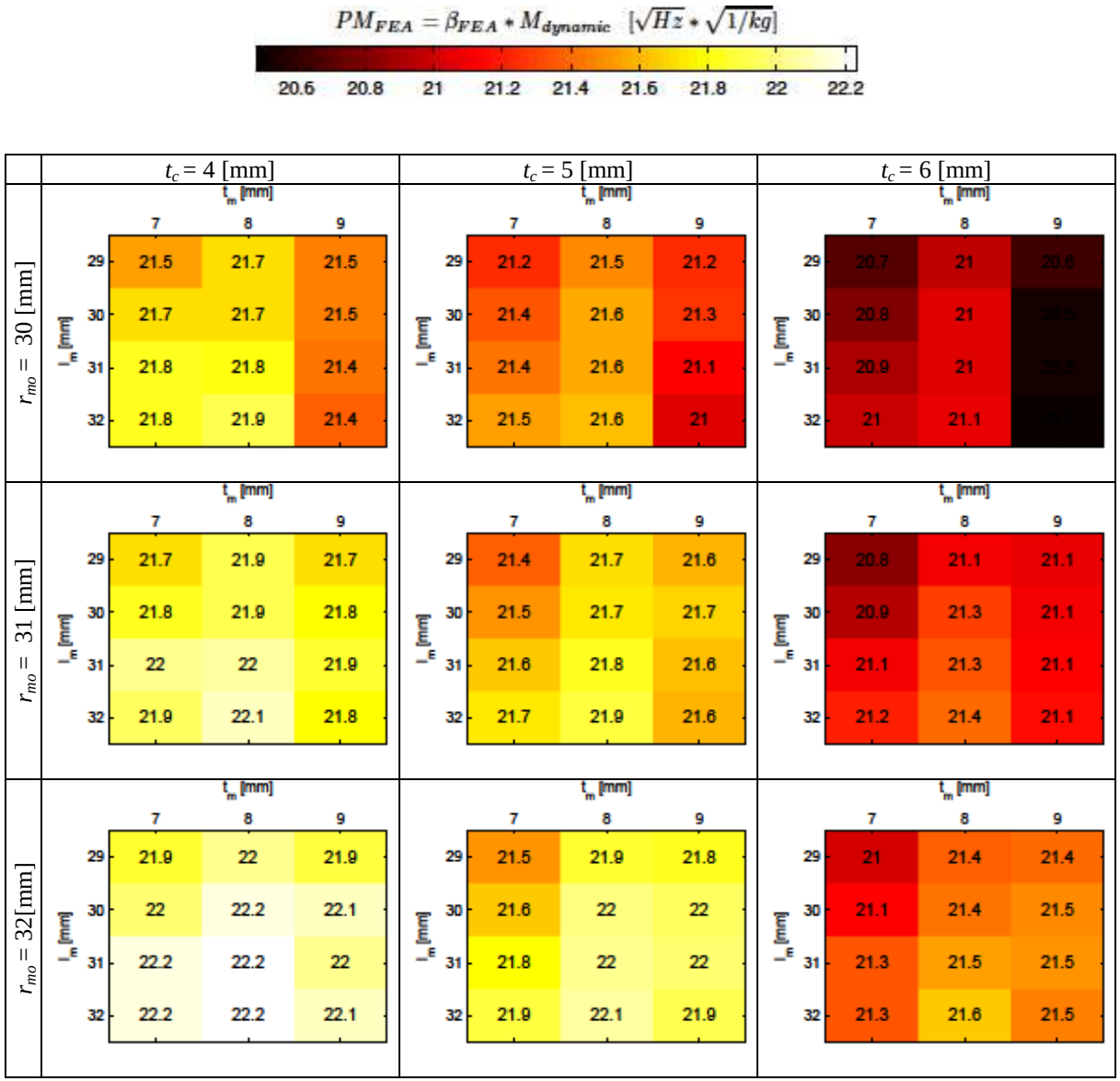

Figure 32: Heat map representation of the FEA approximations of the performance metric over the region of the design space that includes the optimal design. The mass of the payload in these approximations is 0.7 [kg].

CHAPTER 7

7 Experimental setup and results

This section presents the experimental characterization results of the concentric coil, radial magnet MMA that was constructed as a part of this research. The concentric coil, radial magnet MMA that was constructed as a part of this research can be seen in Figure 33, Figure 34, and Figure 35 in the pictures of the experimental setup that was used to characterize the MMA. The experimental setup and the MMA characterization results are described in detail in the following paragraphs. The detailed hardware design of the concentric coil, radial magnet MMA was carried out by David Hiemstra and Daniel Grohnke in collaboration with HIPERNAP LLC [37]. The set of parameter values shown in Table 5 describe the key dimensions of the concentric coil, radial magnet MMA that was constructed. A thorough review of the detailed hardware design, fabrication, and assembly of the concentric coil, radial magnet MMA will be included in a journal paper that is currently under preparation. In what follows below, analysis of the concentric coil, radial magnet MMA's dynamic actuator constant measurement results are first discussed, followed by analysis of the MMA's dynamic mass quantity and performance metric measurement results.

7.1 Experimental setup and measurement results for the dynamic actuator constant

The experimental setup shown in Figure 33, Figure 34, and Figure 35 was used to measure the dynamic actuator constant of the MMA as a function of the MMA's position along its motion range. Figure 33 shows the experimental setup as a whole, comprising the major components that make up an MMA-driven motion system, along with a force sensor testbed that was used to measure the output force of the MMA, and an optical encoder testbed that was used to measure the displacement of the MMA's mover. Figure 34 shows a close-up image of the concentric coil, radial magnet MMA component of the motion system as it was integrated with the experimental setup shown in Figure 33. Figure 35 shows a close-up view of the optical encoder testbed as it was mounted on the constructed concentric coil, radial magnet MMA shown in Figure 33 and Figure 34. The force sensor testbed comprises a miniature strain gauge based load cell (FUTEK LBS200), a manually operated, lead-screw-driven linear slide with fine position control (Velmex A2509P10-S2.5), and a flexure-based decoupler that uses two flexure hinges to absorb any off-axis forces between the MMA and the load cell. The flexure-based decoupler allows for some misalignment between the MMA and the load cell. The linear slide serves as an adjustable ground that fixes the position of MMA, allowing for the MMA's force output to be measured at different positions along its motion range. The optical encoder testbed shown in Figure 35 was used to accurately measure the motion stage's position as the force measurements were carried out. It comprises an optical encoder read-head and scale (Renishaw's Si-HN-4000 read-head, RELM linear scale, and SIGNUM interface electronics).

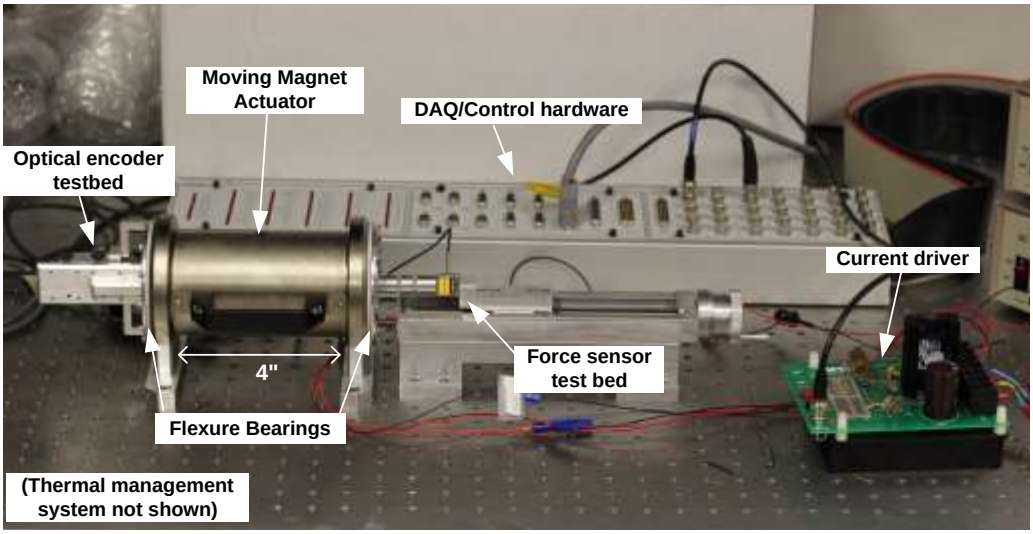

Figure 33: The experimental setup that was used to measure the dynamic actuator constant of the concentric coil, radial magnet MMA that was constructed as a part of this research.

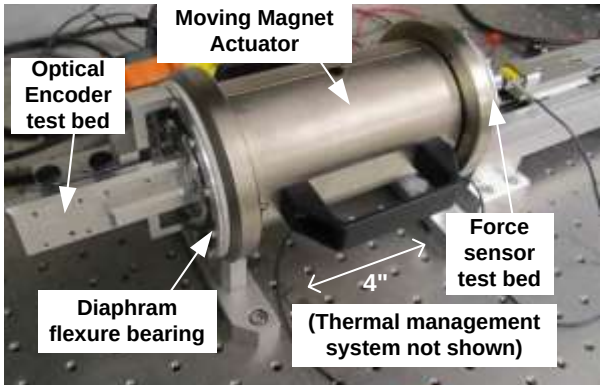

Figure 34: A close-up of the concentric coil, radial magnet MMA component from the experimental testbed shown in Figure 33.

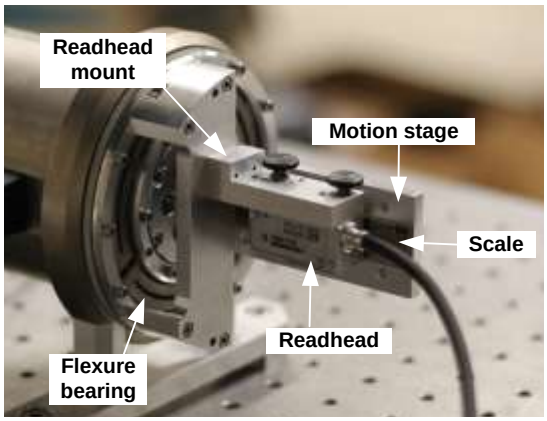

Figure 35: A close-up view of the optical encoder testbed that was used to measure the position of the concentric coil, radial magnet MMA's motion stage.

A measure of the MMA's dynamic actuator constant requires a measure of the MMA's force output, power consumption, and magnet mass. A measure of the magnet mass was obtained by using the known dimensions of the permanent magnets in the MMA's mover assembly to calculate their volume and multiplying their volume with the known density of the permanent magnets. A measure of the MMA's power consumption requires a measure of the coil winding's resistance and a measure of the current in the coil windings. The current driver is used to command a current input into the coil windings, and the coil winding's resistance was measured with a multimeter. A measure of the MMA's force output was obtained via the force sensor testbed. The force output of the MMA was measured at different points along its motion range. The linear slide was used to fix the MMA's position at different points along its motion range, and the optical encoder shown in Figure 35 was used to accurately measure the motion stage's position as the force measurements were carried out. Figure 36 shows the dynamic actuator constant measurements that were obtained at different positions along the motion range of the MMA for a fixed current input of 0.1 [A], along with the corresponding dynamic actuator constant values that were predicted via FEA simulations. A measure of the MMA's dynamic actuator constant as a function of the magnitude of the current input was also obtained while the position of the MMA was held fixed at its center, zero-stroke position. The results are shown in Figure 37, along with the corresponding dynamic actuator constant values that were predicted via FEA simulations.

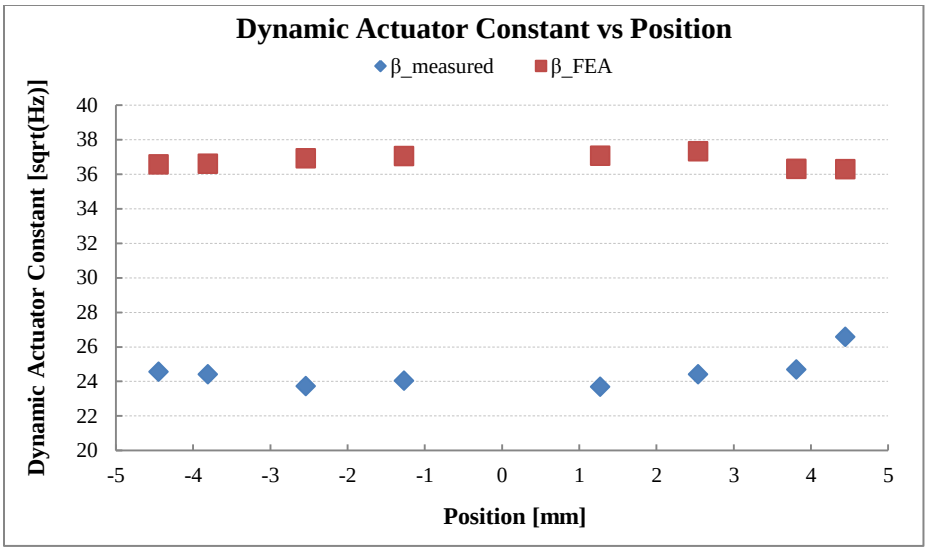

Figure 36: Dynamic actuator constant vs the position of the MMA's motion stage along its motion range. The average dynamic actuator constant measurement is 24.51 [$\sqrt{Hz}$] with a standard deviation of 0.912 [$\sqrt{Hz}$]. When compared to the dynamic actuator constant values obtained via FEA simulations, the average percent error of the measured dynamic actuator constant is -33.31% with a standard deviation of 3.0%.

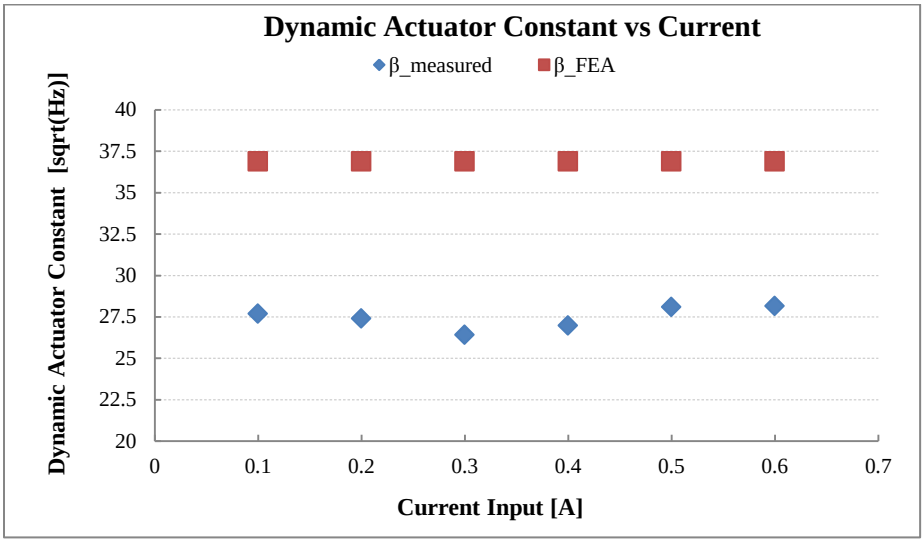

Figure 37: Dynamic actuator constant vs current input. The average dynamic actuator constant measurement is 27.44 [$\sqrt{Hz}$] with a standard deviation of 0.673 [$\sqrt{Hz}$]. When compared to the dynamic actuator constant values obtained via FEA simulations, the average percent error of the measured dynamic actuator constant is -25.57% with a standard deviation of 1.8%.

Figure 36 shows that the concentric coil, radial magnet MMA has a high degree of dynamic actuator constant-stroke uniformity which implies a high degree of force-stroke uniformity. The average measured dynamic actuator constant is 24.51 [$\sqrt{Hz}$] with a standard deviation of 0.912 [$\sqrt{Hz}$]. When compared to the dynamic actuator constant values obtained via FEA simulations, the average percent error of the measured dynamic actuator constant is -33.31% with a standard deviation of 3.0%. Figure 37 shows that the concentric coil, radial magnet MMA has a high degree of dynamic actuator constant-current linearity which implies a high degree of force-current linearity. The average dynamic actuator constant measurement is 27.44 [$\sqrt{Hz}$] with a standard deviation of 0.673 [$\sqrt{Hz}$]. When compared to the dynamic actuator constants obtained via FEA simulations, the average percent error of the measured dynamic actuator constant is -25.57% with a standard deviation of 1.8%.

The experimental results shown in Figure 36 and Figure 37 show that the measured dynamic actuator constant values are well below the dynamic actuator constant values predicted via FEA simulations. In the dynamic actuator constant vs stroke experiment the error is -33.3%, and in the dynamic actuator constant vs current experiment the error is 25.57%. For each of the experimental measurements taken in the respective experiments, the given percent error between the measured and expected value is nearly constant, indicating that the discrepancy between the measured and expected values are due to the same set of factors. More experiments are needed to conclusively identify these set of factors, and more experiments are needed to more accurately quantify this discrepancy. In this context, more experiments means a greater variety of different experiments to obtain the same measurements, and more repetitions of the same experiments to average out any errors or disturbances that might have been present during the experiments. The discrepancy between the measured and expected dynamic actuator constant values can be attributed to a variety of possible factors. Some of these possible factors are listed below:

1. The radially magnetized permanent magnet rings in the mover assembly are an assembly of eight axially magnetized permanent magnet arc segments that, when formed together, approximate the magnetic flux density of a single piece radially magnetized permanent magnet ring. The arc segment permanent magnet assembly would result in a smaller magnetic flux density than the single piece radial permanent magnet. The magnitude of this discrepancy is a currently an open question. At the same time, the arc segment permanent magnet assembly would have a smaller permanent magnet mass than the single piece radial permanent magnet.
2. The larger dynamic actuator constant measurements that were obtained in Figure 37 vs Figure 36 indicate a possible constant, backlash-type force across the stroke that is imposed by the flexure bearings. This backlash-type force, if present, is more prominent in the dynamic actuator constant measurements in Figure 36. This might be due to the relatively small constant current input that was used in that experiment.
3. The dynamic actuator constant values obtained via FEA simulations used a coil overhang of 1 [mm] instead of the 2 [mm] coil overhang of the constructed concentric coil, radial magnet MMA, implying a slightly smaller percent error than reported in Figure 36 and Figure 37.
4. The coil's finite wire coating thickness in the constructed coil, radial magnet MMA was not accounted for in the FEA simulation. Closer inspection of the discrepancy between the coil winding model used in the FEA simulations and the coil windings of the constructed coil, radial magnet MMA would lead to a better assessment of the possible reasons for the discrepancy between the measured and FEA-obtained dynamic actuator constant values.

7.2 Measurement results for the performance metric and other notable parameters

Actuator Level Design Specification	Target Value	Achieved Value
Stroke length, l_s	10 [mm]	10 [mm]
Payload mass, m_p	0.7 [kg]	0.7 [kg]
Permanent magnet mass, m_m	0.685 [kg] (The permanent magnet mass value associated with the maximum *PM* value in the design space that was predicted by FEA simulations)	0.68 [kg]
Size	< (150 [mm] x 150 [mm]) (Desktop Size)	150 [mm] x 100 [mm]
Force-Stroke non-uniformity	<5%	3%
Performance Metric, $PM=\beta*M_{dynamic}$	22.2 $[\sqrt{Hz}\cdot\frac{1}{\sqrt{kg}}]$ (The maximum achievable *PM* value in the design space according to the FEA simulations)	15.4 $[\sqrt{Hz}\cdot\frac{1}{\sqrt{kg}}]$
Dynamic actuator constant, β	36.8 $[\sqrt{Hz}]$ (The dynamic actuator constant value associated with the maximum *PM* value in the design space, as predicted by FEA simulations)	25.5 $[\sqrt{Hz}]$
Dynamic mass quantity, $M_{dynamic}$	0.604 $[\frac{1}{\sqrt{kg}}]$ (The dynamic mass quantity value associated with the maximum *PM* value in the design space that was predicted by FEA simulations)	0.60 $[\frac{1}{\sqrt{kg}}]$
Cont. Force, F	> 40 [N]	51 [N]
Cont. Power, P	Minimize	5 [W]
Coil Resistance, $R_{ic}+R_{oc}$	23.5 [Ω]	21.4 [Ω]

Table 12: The target values and corresponding measured values of the various actuator level design specifications the constructed concentric coil, radial magnet MMA was designed to satisfy.

CHAPTER 8

8 Conclusion

In this thesis, analysis of the dynamics and control of a general single-axis, MMA-driven, flexure-based motion system indicated that there are four critical actuator level design specifications that an MMA must satisfy to maximize the performance of the motion system: one, a large motion range; two, a highly uniform force-stroke profile; three, reasonably small off-axis attraction forces between the permanent magnet and the back iron; and four, a large magnitude of the product of the actuator's dynamic actuator constant and dynamic mass quantity – a product referred to as the *performance metric (PM)* throughout this thesis. As is suggested by the fourth actuator level design specification, the analysis showed that solely maximizing an actuator's dynamic actuator constant (as suggested in the previous literature [1]), is not the best strategy for maximizing overall motion system performance. Instead, the analysis showed that a better strategy for maximizing overall motion system performance is to maximize the performance metric, i.e. the product of the actuator's dynamic actuator constant and dynamic mass quantity. Maximizing an actuator's dynamic actuator constant and dynamic mass quantity independently from one another is also not an appropriate strategy for maximizing overall motion system performance since the two quantities are not completely independent; rather, both are a function of the mass of the permanent magnet. Analysis of the dynamic mass quantity for different combinations of payload and permanent magnet masses showed that the magnitude of the dynamic mass quantity can take on a wide range of values, implying that the magnitudes of the payload and permanent magnet masses have a significant effect on the maximum performance the motion system is capable of. The aforementioned finding, however, does not discredit the utility of the dynamic actuator constant as a figure of merit; it instead sheds light on its true value.

Because the dynamic actuator constant of an MMA is independent of geometric scaling, it is useful for comparing the relative performance merit of different types of MMA architectures. When making this comparison, the MMAs should be scaled up or down in size so that their respective permanent magnet masses are close to equal. The stroke length of the different designs should also be close to equal. After this scaling is done, the dynamic mass quantities of the different MMA designs, assuming the same payload, become comparable to one another; the magnitude of each MMA's dynamic actuator constant can then be used as a relative measure of the inherent performance merit associated with the different MMA designs. Consideration of the dynamic actuator constant played a significant role in the evaluation process used to compare the relative performance merit of several variations of the concentric coil, radial magnet MMA architecture. The variations of the concentric coil, radial magnet MMA architecture were evaluated in order to identify the variation that could best satisfy the four critical actuator level design specifications required of MMAs used in high performance motion systems. The variation of the concentric coil, radial magnet MMA architecture shown in Figure 2 was identified as the variation with the greatest potential performance.

The potential performance of the concentric coil, radial magnet MMA architecture was bolstered by the presented analysis of an idealized model representative of the force producing physics of an MMA that revealed the existence of a fundamental upper limit to the maximum achievable dynamic actuator constant of a Lorentz force actuator. The fundamental upper limit to the maximum achievable dynamic actuator constant was found to be solely a function of the permanent magnet and coil winding material properties. Assuming the use of the best available permanent magnet (N52-grade neodymium) and coil winding (copper) material, the upper limit to the dynamic actuator constant was calculated to be 62.8 [$\sqrt{Hz}$]. The upper limit to the dynamic actuator constant is a useful metric, providing insight on the degree to which practical factors (e.g. flux fringing, magnetic saturation, finite assembly tolerances, material properties, etc.) limit optimal performance, in addition to providing insight into the relative performance merit of different MMA designs. It was reasoned that MMA architectures that share similar characteristics to the idealized model are likely to have larger dynamic actuator constants than MMA architectures that do not share similar characteristics to the idealized model. The recently reported concentric coil, radial magnet MMA architecture is more similar to the idealized model than the traditional MMA architecture; an indicator of the concentric coil, radial magnet MMA architecture's potential for exceeding the performance of the traditional type of MMA architecture.

A brute-force search optimization process was used to optimize the design of the concentric coil, radial magnet MMA architecture. A closed form approximation of the product of the concentric coil, radial magnet MMA's dynamic actuator constant and dynamic mass quantity was derived as a function of the geometric and material property parameters that define a concentric coil, radial magnet MMA design. Analysis of the accuracy of the closed form approximation of the dynamic actuator constant across the design space of interest showed that it

had a consistent percent error of ≈10% across most of the design space when compared to the FEA-based dynamic actuator constant approximations, validating the use of the closed form approximation of the performance metric to identify the approximate location of the optimal concentric coil, radial magnet MMA design in the design space. The closed form approximation of the concentric coil, radial magnet MMA's performance metric was used to calculate the performance metric value of every MMA design in the design space, and the results were mapped onto a heat map representation of the MMA's design space, allowing one to quickly identify the optimal concentric coil, radial magnet MMA design's approximate location in the design space by visual inspection of the heat map.

The optimal concentric coil, radial magnet MMA design's dynamic actuator constant and performance metric values were predicted by FEA simulations to be 36.8 [$\sqrt{Hz}$] and 0.604 [$\frac{1}{\sqrt{kg}}$], respectively. Experimental characterization of the constructed concentric coil, radial magnet MMA yielded an MMA with a dynamic actuator constant value of 25.5 [$\sqrt{Hz}$], which is 27.5% larger than the largest dynamic actuator constant value of ≈20 [$\sqrt{Hz}$] that was reported in the survey of traditional MMA architectures conducted in prior work [5], and 82.1% larger than the dynamic actuator constant value of 14 [$\sqrt{Hz}$] that was reported for the MMA of the traditional type that was designed and constructed in prior work [1][5].

There are several new questions and issues that came up during the course of this thesis research that are not completely answered yet. These questions/issues are listed below and can serve as topics for future investigation.

Open questions/ Future work.

1. More experimental analysis needs to be conducted to identify the source(s) of the discrepancy between the expected dynamic actuator constant of 36.8 [$\sqrt{Hz}$] that was predicted by FEA simulations and the measured dynamic actuator constant of 25.5 [$\sqrt{Hz}$]. This discrepancy can possibly be attributed to a variety of factors such as inefficiencies in the transmission system, mechanical design flaws, mischaracterization of the measured dynamic actuator constant of the constructed concentric coil, radial magnet MMA, etc. Conducting a variety of experiments that measure the MMA's dynamic actuator constant in different ways would be helpful in teasing out the source(s) of the discrepancy between the expected and measured dynamic actuator constant values.
2. A thorough analysis of the implications of the dynamic actuator constant and dynamic mass quantity on the performance of actuators other than MMAs would be a valuable addition to this line of research.
3. A thorough investigation of the factors contributing to the discrepancy between the upper limit to the maximum achievable dynamic actuator constant and the dynamic actuator constant values that are predicted by FEA simulations would be a valuable addition to this line of research. The investigation would help to uncover the phenomena responsible for this discrepancy and possible strategies for overcoming these phenomena.

APPENDIX A

A. Relationship between the dynamic variables of force output and power consumption in the expression for the dynamic actuator constant

The dynamic actuator constant is defined as follows,

$$\beta = \frac{K_t}{\sqrt{R}\sqrt{m_m}} = \frac{F_a(t)}{\sqrt{P(t)}\sqrt{m_m}}, \tag{96}$$

where K_t is the actuator force constant, and R is the coil winding resistance. Although the dynamic actuator constant is an actuator constant in that it is a function of actual physical parameters such as size, construction, materials, and geometry, it can also be stated in terms of the dynamic variables indicated above (i.e., $F_a(t)$ and $P(t)$). In what follows below, analysis of the relationship between the force output and power consumption of an actuator carrying out the raster scanning and point-to-point positioning motion profiles will show that the dynamic actuator constant expression that is a function of the dynamic variables is identical to the corresponding expression that is a function of the actuator's physical parameters independent of time.

A.1 Relationship between the force output and power consumption of an MMA carrying out the sinusoidal, raster scanning motion profile

Recall from Section 2.2.1 that an actuator must output the following force waveform to carry out the raster scanning motion profile,

$$F_r(t) = F_{r0}\sin(\omega t), \tag{97}$$

where, $F_{r0} = \frac{\Delta}{2}\left(m_m + m_p\right)\left(\omega_n^2 - \omega^2\right)$, which implies that, $\left|F_{r0}\right| = \frac{\Delta}{2}\left(m_m + m_p\right)\left|\omega_n^2 - \omega^2\right|$. Given that the following relationship between current and actuator force output is true for all instances of time, t,

$$F_a(t) = K_t I(t), \tag{98}$$

an actuator with actuator constant K_t would have to have the following current input to sustain the raster scanning motion profile:

$$I_r(t) = \frac{F_r(t)}{K_t} = \frac{F_{r0}\sin(\omega t)}{K_t}. \tag{99}$$

Letting $I_{r0} = \frac{F_{r0}}{K_t}$,

$$I_r(t) = I_{r0}\sin(\omega t). \tag{100}$$

It is well known that, for any time t, $P(t) = I^2(t)R$, which implies that,

$$P_r(t) = RI_{r0}^{\ 2}\sin^2(\omega t). \tag{101}$$

Letting $P_{r0} = RI_{r0}^{\ 2}$,

$$P_r(t) = P_{r0}\sin^2(\omega t). \tag{102}$$

Comparing the power input and force output waveforms required for an actuator to sustain the raster scanning motion profile,

$$\begin{aligned} F_r(t) &= F_{r0}\sin(\omega t) \\ \mathrm{P}_r(t) &= P_{r0}\sin^2(\omega t) \end{aligned}, \tag{103}$$

it is evident that the time at which the raster scanning motion profile demands the greatest force output from the actuator corresponds to the time of maximum power consumption. From the above it can be concluded that,

$$\frac{F_r(t)}{\sqrt{P_r(t)}} = \frac{F_{r0}\sin(\omega t)}{\sqrt{P_{r0}\sin^2(\omega t)}} = \frac{F_{r0}}{\sqrt{P_{r0}}} = \frac{K_t}{\sqrt{R}} \tag{104}$$

.

Equation (104) shows how the ratio of the dynamic variables of force output and the square root of power consumption is constant for all time, *t*. Hence, when calculating or deriving the dynamic actuator constant with the dynamic variables of force output and power consumption, it must be ensured that the instantaneous values of the corresponding dynamic variables of force output and power consumption are used, not the average or mean root-squared values of the dynamic variables. Note here that power fluctuates and is not constant. In general, it might be worthwhile to look at the average power which is a practically useful quantity:

$$P_{avg} = \frac{P_{r0}}{2}\,. \tag{105}$$

Sometimes, one may even define the root-mean square (RMS) value of current:

$$\begin{aligned} & P_{avg} = I_{RMS}^2 R \\ \Rightarrow\ & \frac{P_{r0}}{2} = I_{RMS}^2 R\,. \\ \Rightarrow\ & I_{RMS} = \frac{I_{r0}}{\sqrt{2}} \end{aligned} \tag{106}$$

A.2 Relationship between the force output and power consumption of an MMA carrying out the triangular velocity, point-to-point positioning motion profile

To carry out the point-to-point positioning, triangular velocity motion profile discussed in Section 2.2.2, an actuator must output force waveforms,

$$F_{pp1}(t) = \frac{2\Delta\left(m_m + m_p\right)\left(2 + t^2 w_n{}^2\right)}{t_r{}^2} \quad \text{for } \left(0 \le t \le \frac{t_r}{2}\right), \tag{107}$$

and,

$$F_{pp2}(t) = -\frac{\Delta\left(m_m + m_p\right)\left(4 + 2t^2 w_n{}^2 - 4t t_r w_n{}^2 + t_r{}^2 w_n{}^2\right)}{t_r{}^2} \quad \text{for } \left(\frac{t_r}{2} < t \le t_r\right). \tag{108}$$

Letting $F_{a,pp1,0} = 2\Delta\left(m_m + m_p\right)$, and $F_{a,pp2,0} = \Delta\left(m_m + m_p\right)$, Equations (107) and (108) can be expressed as follows,

$$F_{a,pp1}(t) = F_{a,pp1,0}\frac{\left(2 + t^2 w_n{}^2\right)}{t_r{}^2} \quad \text{for } \left(0 \le t \le \frac{t_r}{2}\right), \tag{109}$$

$$F_{a,pp2}(t) = -F_{a,pp2,0}\frac{\left(4+\left(2t^2-4tt_r+{t_r}^2\right){w_n}^2\right)}{{t_r}^2} \quad \text{for } \left(\frac{t_r}{2} < t \le t_r\right). \tag{110}$$

The relationship between an actuator's current input and force output can be expressed as,

$$F_{a,pp1}(t) = K_t I_{pp1}(t) \quad \text{for } \left(0 \le t \le \frac{t_r}{2}\right), \tag{111}$$

$$F_{a,pp2}(t) = K_t I_{pp2}(t) \quad \text{for } \left(\frac{t_r}{2} < t \le t_r\right), \tag{112}$$

which implies that an actuator with actuator constant K_t would have to have the following current input to carry out the triangular velocity motion profile:

$$I_{pp1}(t) = \frac{F_{a,pp1}(t)}{K_t} = \frac{\left(m_m+m_p\right)\Delta{\omega_n}^2\left(2\left(\frac{t}{t_r}\right)^2+\frac{4}{\left(\omega_n t_r\right)^2}\right)}{K_t} \quad \text{for } \left(0 \le t \le \frac{t_r}{2}\right), \tag{113}$$

$$I_{pp2}(t) = \frac{F_{a,pp2}(t)}{K_t} = \frac{\left(m_m+m_p\right)\Delta{\omega_n}^2\left(-2\left(\frac{t}{t_r}\right)^2+4\frac{t}{t_r}-1-\frac{4}{\left(\omega_n t_r\right)^2}\right)}{K_t} \quad \text{for } \left(\frac{t_r}{2} < t \le t_r\right), \tag{114}$$

It is well known that the expression for the power consumption of a Lorentz force actuator is $\mathrm{P}(t) = I^2(t)\,\mathrm{R}$, implying that the power consumption of an actuator carrying out the triangular velocity motion profile can be expressed as follows,

$$P_{pp1}(t) = {I_{pp1}}^2(t)R = \frac{4\Delta^2\left(m_m+m_p\right)^2 R\left(2+t^2{w_n}^2\right)^2}{{K_t}^2{t_r}^4} \quad \text{for } \left(0 \le t \le \frac{t_r}{2}\right), \tag{115}$$

$$P_{pp2}(t) = {I_{pp2}}^2(t)R = \frac{\Delta^2\left(m_m+m_p\right)^2 R\left(4+\left(2t^2-4tt_r+{t_r}^2\right){w_n}^2\right)^2}{{K_t}^2{t_r}^4} \quad \text{for } \left(\frac{t_r}{2} < t \le t_r\right). \tag{116}$$

Letting $P_{pp1,0} = \frac{4\Delta^2\left(m_m+m_p\right)^2 R}{{K_t}^2}$ and $P_{pp2,0} = \frac{\Delta^2\left(m_m+m_p\right)^2 R}{{K_t}^2}$,

$$P_{pp1}(t) = P_{pp1,0}\frac{\left(2+t^2{w_n}^2\right)^2}{{t_r}^4} \quad \text{for } \left(0 \le t \le \frac{t_r}{2}\right), \tag{117}$$

$$P_{pp2}(t) = P_{pp2,0}\frac{\left(4+\left(2t^2-4tt_r+{t_r}^2\right){w_n}^2\right)^2}{{t_r}^4} \quad \text{for } \left(\frac{t_r}{2} < t \le t_r\right). \tag{118}$$

Comparing $F_{app,1}(t)$ and $P_{pp1}(t)$,

$$F_{a,pp1}(t) = F_{a,pp1,0}\frac{\left(2+t^2 w_n{}^2\right)}{t_r{}^2}$$
$$P_{pp1}(t) = P_{pp1,0}\frac{\left(2+t^2 w_n{}^2\right)^2}{t_r{}^4} = P_{pp1,0}\left(\frac{\left(2+t^2 w_n{}^2\right)}{t_r{}^2}\right)^2 \quad \text{for } \left(0 \le t \le \frac{t_r}{2}\right), \tag{119}$$

it can be concluded that the ratio of the dynamic variables of force output and the square root of power consumption is a constant throughout the first half of the triangular velocity motion profile, i.e.,

$$\frac{F_{a,pp1}(t)}{\sqrt{P_{pp1}(t)}} = \frac{F_{a,pp10}}{\sqrt{P_{pp1,0}}} = \frac{2\Delta\left(m_m + m_p\right)}{\sqrt{\frac{4\Delta^2\left(m_m+m_p\right)^2 R}{K_t{}^2}}} = \frac{K_t}{\sqrt{R}} \quad \text{for } \left(0 \le t \le \frac{t_r}{2}\right), \tag{120}$$

Comparing $F_{app,2}(t)$ and $P_{app,2}(t)$,

$$F_{a,pp2}(t) = -F_{a,pp2,0}\frac{\left(4+\left(2t^2-4tt_r+t_r{}^2\right)w_n{}^2\right)}{t_r{}^2}$$
$$P_{pp2}(t) = P_{pp2,0}\frac{\left(4+\left(2t^2-4tt_r+t_r{}^2\right)w_n{}^2\right)^2}{t_r{}^4} = P_{pp2,0}\left(\frac{\left(4+\left(2t^2-4tt_r+t_r{}^2\right)w_n{}^2\right)}{t_r{}^2}\right)^2 \quad \text{for } \left(\frac{t_r}{2} < t \le t_r\right). \tag{121}$$

it can be concluded that the ratio of the magnitude of the dynamic variable of force output and the square root of power consumption is a constant throughout the second half of the triangular velocity motion profile, i.e.,

$$\frac{\left|F_{a,pp2}(t)\right|}{\sqrt{P_{pp2}(t)}} = \frac{K_t}{\sqrt{R}} \quad \text{for } \left(\frac{t_r}{2} < t \le t_r\right), \tag{122}$$

which, together with Equation (120), implies that,

$$\beta = \frac{\left|F_{a,pp}(t)\right|}{\sqrt{P_{pp}(t)}\sqrt{m_m}} = \frac{K_t}{\sqrt{R}\sqrt{m_m}} \quad \text{for } \left(0 < t \le t_r\right). \tag{123}$$

The above analysis implies that, when calculating or deriving the dynamic actuator constant with the dynamic variables of force output and power consumption, it must be ensured that the instantaneous values of the corresponding dynamic variables are used, not the average or mean root-squared values of the dynamic variables.

APPENDIX B

B. Example MATLAB code for generating a heat map

```
%Closed form approximations of the dynamic actuator...
%constant over a large design space

%All dimensions below are in SI units
clear all;

%CommonSystemAndActuatorSpecifications
ls=0.01; %stroke length
mp=0.3; %payload mass

%Material and numerical constants in the dynamic actuator constant
%expression
Br=1.4;
rhoc=1.68*10^(-8);
rhom=7600;
Bsat=1.6;

%Defining the geometric design space to span
rmo=0.024:0.004:0.032;
tc=0.002:0.002:0.008;
tm=0.002:0.002:0.019;
lm=0.005:0.005:0.090;
tgmech=0.0011;

[lmmesh,tmmesh,tcmesh,rmomesh]=ndgrid(lm,tm,tc,rmo);

%BetaMaterialConstant
BetaMaterialConst=sqrt(2*pi)*Br/sqrt(rhoc*rhom);

%Beta
Beta=BetaMaterialConst*sqrt(1/(1+ls./lmmesh)).*...
    (sqrt(tmmesh).*sqrt(tcmesh))./((2*rmomesh-tmmesh).*...
    (log(1+tgmech./rmomesh)+...
    log(1+tcmesh./(rmomesh+tgmech))+...
    log(1+tgmech./(rmomesh-tgmech-tmmesh))+...
    log(1+tcmesh./(rmomesh-tgmech-tcmesh-tmmesh))+...
    log(rmomesh./(rmomesh-tmmesh))));

%DynamicMassQuantity
DynamicMassQuantity=((sqrt(2*pi*rhom*lmmesh.*...
    (2*rmomesh-tmmesh).*tmmesh))./...
    (mp+(2*pi*rhom*lmmesh.*(2*rmomesh-tmmesh).*tmmesh)));

%PerformanceMetric
PerformanceMetric=BetaMaterialConst*sqrt(1/(1+ls./lmmesh)).*...
    (sqrt(tmmesh).*sqrt(tcmesh))./...
    ((2*rmomesh-tmmesh).*(log(1+tgmech./rmomesh)+...
    log(1+tcmesh./(rmomesh+tgmech))+...
    log(1+tgmech./(rmomesh-tgmech-tmmesh))+...
    log(1+tcmesh./(rmomesh-tgmech-tcmesh-tmmesh))+...
    log(rmomesh./(rmomesh-tmmesh)))).*...
    ((sqrt(2*pi*rhom*lmmesh.*(2*rmomesh-tmmesh).*tmmesh))./...
```

```
    (mp+(2*pi*rhom*lmmesh.*(2*rmomesh-tmmesh).*tmmesh)));

%Magnet length that makes inner iron saturate
lmsat=(Bsat./(Br.*tmmesh)).*...
    log(((rmomesh+tgmech)./(rmomesh-tmmesh)).*...
    (1+tcmesh./(rmomesh+tgmech)).*...
    (1+tgmech./(rmomesh-tgmech-tmmesh)).*...
    ((1+tcmesh./(rmomesh-tgmech-tcmesh-tmmesh)))).*...
    (rmomesh.^2-2*rmomesh.*tcmesh+tcmesh.^2-2*rmomesh.*tgmech+...
    2*tcmesh*tgmech+tgmech^2-2*rmomesh.*tmmesh+2*tcmesh.*tmmesh+...
    2*tgmech.*tmmesh+tmmesh.^2);

SaturationConstraint=lmmesh<lmsat;
Beta = Beta.*SaturationConstraint;
PerformanceMetric = PerformanceMetric.*SaturationConstraint;

%Takes the huge set of data in the PerformanceMetric matrix, and turns it
%into a j by i cell array called PMtest, where i, the number of rows in
%PMtest, corresponds to the number of rmo values we wish to span, and j,
%the number of columns in PMtest, corresponds to the the number of tc
%values we wish to span. Let the location of an entry in the PMtest cell
%array be (i*j), e.g. (1x2). This entry in the PMtest cell array is a j*i
%cell array. The values in the PMtest cell array entries are called by
%using PMtest{j,i}. This takes the array PMtest(j,i), and makes it into the
%matrix,PMtest{j,i}.Each PMtest{j,i}corresponds to the performance metric
%values as lm and tm vary for a given combination of rmo and tc values. The
%matrices are named PMtest{j,i}. As shown below, the length of i is equal
%to the number of rows in the PerformanceMetric array. It corresponds to
%the number of rmo values we wish to span. The length of j is equal to the
%number of columns in  the PerformanceMetric array. It corresponds to the
%the number of tc values we wish to span.
for i=1:length(tc)
    for j=1:length(rmo)
        PMtest{j,i}=PerformanceMetric(:,:,i,j);
    end
end

%Takes each cell array PMtest(j,i) in the cell array PMtest and turns it
%into a 1 column cell array with all the values from array PMtest(j,i)
AllPMValues=cellfun(@(x) x(:),PMtest, 'UniformOutput', false);

%Minimum PM of the entire set of data
MinPMFromEachSetOfData=cellfun(@(x) min(x((x>0))),AllPMValues);
minPM=min(MinPMFromEachSetOfData(:));

%Maximum PM of the entire set of data
MaxPMFromEachSetOfData=cellfun(@(x) max(x),AllPMValues);
maxPM=max(MaxPMFromEachSetOfData(:));

%% Making the "hotzones maps" 1
%This heat map is a collection of heatmaps that are representative of the
%entire design space as defined above. The color scale is shown next
%to each heatmap entry via the "colorbar" function.
figure
colormap(hot)
p=0;
for i=1:length(rmo)
```

```
    for j=1:length(tc)
       p=p+1;
       subplot(length(rmo),length(tc),p)
       imagesc(tm*1000,lm*1000,PMtest{i,j})
       caxis([minPM,maxPM])
       colorbar
       title(['rmo=' num2str(rmo(i)) ',' 'tc=' num2str(tc(j))])
       set(gca,'xTick',tm*1000)
       set(gca,'xaxisLocation','top')
       set(gca,'yTick',lm*1000)
       grid off
       xlabel('tm [mm]')
       ylabel('lm [mm]')
    end
end

%% Making the "hotzones maps" 2
%This heat map is a collection of heatmaps that are representative of the
%entire design space as defined above. It is the same as the first
%heatzone map except that the color scale is omitted and the grid is
%removed.
figure
colormap(hot)
p=0;
for i=1:length(rmo)
    for j=1:length(tc)
       p=p+1;
       subplot(length(rmo),length(tc),p)
       imagesc(tm*1000,lm*1000,PMtest{i,j})
       caxis([minPM,maxPM])
%        colorbar
       title(['rmo=' num2str(rmo(i)) ',' 'tc=' num2str(tc(j))])
       set(gca,'xTick',tm*1000)
       set(gca,'xaxisLocation','top')
       set(gca,'yTick',lm*1000)
       grid on
       xlabel('tm [mm]')
       ylabel('lm [mm]')
    end
end

%% Making the "hotzones maps" 3
%This heat map is representative of the performance metric values for the
%matrix, PMtest{3,1}, which corresponds to the set of performance metric
%values as lm and tm vary for a given rmo and tm value. The j=3, i=1
%entries in PMtest{j,i} correspond to the third rmo value and the first
%tc value in the matrices used to define the design space. The performance
%metric values are included in text for each MMA design in the design space
%that PMtest{3,1} is representative of.

figure
colormap(hot)
imagesc(PMtest{3,1})

set(gca,'XTick',tm*1000)
set(gca,'XTickLabel',tm*1000)
set(gca,'XAxisLocation','top')
```

```
xlabel('tm [mm]')

set(gca,'YTick',lm*1000/5)
set(gca,'YTickLabel',lm*1000)
ylabel('lm [mm]')

caxis([minPM,maxPM])
colorbar
data=PMtest{3,1};

[rows,cols] = size(data);
for i = 1:rows
    for j = 1:cols
                 textHandles(j,i) = text(j,i,num2str(data(i,j)),...
                'units','data','horizontalAlignment','center' );
    end
end
```

REFERENCES

[1] D. B. Hiemstra, G. Parmar, and S. Awtar, "Performance tradeoffs posed by moving magnet actuators in flexure-based nanopositioning," *IEEE/ASME Transactions on Mechatronics*, vol. 19, no. 1, pp. 201-212, Feb. 2014

[2] S. Verma, K. Won-jong, and G. Jie, "Six-axis nanopositioning device with precision magnetic levitation technology," *IEEE/ASME Transactions on Mechatronics,* vol. 9, no.2, pp. 384-391, Jun. 2004.

[3] T. Yamada, S. Koganezawa, K. Aruga, and Y. Mizoshita, "A high-performance and low-profile moving-magnet actuator for disk drives," *IEEE Transactions on Magnetics,* vol. 30, no. 6, pp. 4227-4229, Nov. 1994.

[4] S. Braune and S. Liu, "Design of a novel moving magnet linear motor for use as a valve actuator," in *Proc. 31st Annual Conference of the IEEE Industrial Electronics Society*, Piscataway, NJ, USA, 2005, pp. 2041-2046.

[5] D. B. Hiemstra, "The design of moving magnet actuators for large-range flexure-based nanopositioning," M. S. thesis, Dept. of Mech. Eng., Univ. of Michigan, Ann Arbor, MI, 2014.

[6] F. L. Langley and P. H. Mellor, "High-specific output bidirectional moving magnet actuator for use in active vibration control of rotorcraft," *IET Electric Power Applications*, vol. 5, no. 1, pp. 100-110, 2011.

[7] R. Banik and D. G. Gweon, "Design and optimization of voice coil motor for application in active vibration isolation," *Sensors and Actuators, A Physical*, vol. 137, no. 2, pp. 236-243, 2007.

[8] R. E. Clark and D. Smith, "Design optimization of moving-magnet actuators for reciprocating electro-mechanical systems," *IEEE Transactions on Magnetics*, vol. 31, no. 6, pp. 3746-3748, 1995.

[9] S. Awtar and G. Parmar, "Physical and control systems design challenges in large range nanopositioning," in *IFAC Symposium on Mechatronic Systems*, Cambridge, MA, 2010, pp. 153-159.

[10] A. Sinno, P. Ruaux, L. Chassagne, S. Topcu, Y. Alayli, G. Lerondel, S. Blaize, A. Bruyant, and P. Royer, "Enlarged atomic force microscopy scanning scope: novel sample-holder device with millimeter range," *Review of Scientific Instruments,* vol. 78, pp. 1-7, 2007.

[11] Y. K. Yong, B. Bhikkaji, and S. O. Reza Moheimani, "Design, modeling, and FPAA-based control of a high-speed atomic force microscope nanopositioner," *IEEE/ASME Transactions on Mechatronics*, vol. 18, no. 3, pp. 1060-1071, Jun. 2012.

[12] K. Salaita, Y. Wang, and C. A. Mirkin, "Applications of dip-pen nanolithography," *Nat Nano,* vol. 2, pp. 145-155, 2007.

[13] M. van de Moosdijk, E. van den Brink, K. Simon, A. Friz, G. Phillipps, R. Travers, and E. Raaymakers, "Collinearity and stitching performance on an ASML stepper," in *Emerging Lithographic Technologies VI*, 2002, pp. 858-66.

[14] G. Schitter and M. J. Rost, "Scanning probe microscopy at video-rate," *Materials Today,* vol. 11, no. 1, pp. 40-48, 2008.

[15] S. Awtar and G. Parmar, "Design of a large range XY nanopositioning system," in *ASME international design engineering technical conference*, 2010, pp. 387–399.

[16] W. O'Brien, "Long-range motion with nanometer precision," *Photonics Spectra*, vol. 39, pp. 80-81, 2005.

[17] D. Hiemstra, G. Parmar, C. Welch, and S. Awtar, "Electromagnetic actuators and component designs thereof," *US Pat. Application* USA 2014/0235644.

[18] D. P. Looze, J. S. Freudenberg, J. H. Braslavsky, and R. H. Middleton. "Trade-Offs and Limitations in Feedback Systems" in *Control System Advanced Methods*, 2nd ed., W. S. Levine, Ed. Boca Raton, FL: CRC Press, 2011, pp. (10-1) - (10-36).

[19] G. Parmar, D. Hiemstra, Y.Chen, and S. Awtar. "A moving magnet actuator for large range nanopositioning." *Proc. ASME Dynamic Systems and Control Conference*, 2011, pp. 41–48.

[20] G. Parmar, "Dynamics and control of flexure-based large range nanopositioning systems", Ph.D. dissertation, Dept. of Mech. Eng., Univ. of Michigan, Ann Arbor, MI, 2014.

[21] G. Parmar, K. Barton, and S. Awtar, "Large dynamic range nanopositioning using iterative learning control", *Precision Engineering*, vol. 38, no. 1, pp. 48-56, 2014.

[22] G. F. Franklin, J. D. Powell, and A. Emami-Naeini. *Feedback Control of Dynamic Systems, 5th ed.*, Upper Saddle River, NJ: Pearson Education, Inc., 2006, pp. 316-323.

[23] S. Awtar, A. H. Slocum, "Design of flexure stages based on a symmetric diaphragm flexure," *Proc. ASPE 2005 Annual Meeting*, Norfolk, VA, 2005, Paper No. 1803

[24] T. Morcos, "The Straight Attraction: Part One," *Motion Control Magazine*, p.33, Jun. 2000. [Online]. Available: http://www.acm-magnetics.com/acm/pdfs/9-TheStraightAttractionPart1.pdf.

[25] D. K. Cheng, *Field and Wave Electromagnetics*, 2nd ed. Reading, MA: Addison-Wesley Publishing Company, 1989, p. 254.
[26] H.-D. Chai, *Electromechanical Motion Devices*. Upper Saddle River, NJ: Prentice Hall, 1998.
[27] "Temperature and Neodymium Magnets." [Online]. Available: http://www.kjmagnetics.com/blog.asp?p=temperature-and-neodymium-magnets.
[28] "Product Model # NCM01-07-001-2X." H2W Technologies, Inc. [Online]. Available: http://www.h2wtech.com/product/voice-coil-actuators/NCM01-07-001-2X.
[29] Y. Hirabayashi, T. Oyama, S. Saito, and H. Sohno, "Moving magnet-type actuator," *US Pat. 5,434,549*, 1995.
[30] T. Morcos, "The Straight Attraction: Part Two," *Motion Control Magazine*, p.25, July/August 2000. [Online]. Available: http://www.acm-magnetics.com/acm/pdfs/10-TheStraightAttractionPart2.pdf
[31] K. Shirey, S. Banks, R. Boyle, and R. Unger, "Design and qualification of the AMS-02 flight cryocoolers," *Cryogenics (Guildf).*, vol. 46, pp. 143–148, 2006.
[32] M. Watada and K. Yanashima, "Improvement on characteristics of linear oscillatory actuator for artificial hearts," *IEEE Trans. Magn.*, vol. 29, no. 6, pp. 3361–3363, 1993.
[33] D. Howe, "Magnetic actuators," *Sensors Actuators A Phys.*, vol. 81, no. 1–3, pp. 268–274, Apr. 2000.
[34] N. Bianchi, S. Bolognani, and F. Tonel, "Design criteria of a tubular linear IPM motor," in *IEEE International Electric Machines and Drives Conference*, 2001, pp. 1–7.
[35] J. Huber, N. Fleck, and M. Ashby, "The selection of mechanical actuators based on performance indices," *R. Soc. Eng. Sci.*, vol. 453, no. 1965, pp. 2185–2205, 1997.
[36] E. P. Furlani, *Permanent Magnet and Electromechanical Devices*. New York: Academic Press, 2001.
[37] "HIPERNAP Technical Report #110". Jan. 20, 2014.